Development of an Opaque Liquid Scintillator Detector for use in the DarkMESA Experiment

by

Jonas Pätschke

Master's Thesis in Physics
submitted to the Department of Physics, Mathematics and Computer Science
(FB 08)
of the Johannes Gutenberg-University Mainz
on the 11th of February 2026

1st Supervisor: PD Dr. Luca Doria
2nd Supervisor: Dr. Stefan Schoppmann

Abstract

In the ongoing search for light Dark Matter, the DarkMESA and NuDoubt^{++} collaborations have joined forces to explore a new region of parameter space. DarkMESA is an upcoming electron beam dump experiment at the new MESA accelerator facility in Mainz, designed to search for light Dark Matter particles mediated by a hypothetical dark photon, using a crystal calorimeter as detector. The NuDoubt^{++} experiment will employ an opaque liquid scintillator detector to investigate double beta decay ($2\nu\beta\beta$) and the beyond–Standard Model neutrinoless double beta decay ($0\nu\beta\beta$), the second of which is yet to be discovered and would indicate the Majorana nature of the neutrino.

This thesis details the construction and testing of a prototype opaque liquid scintillator detector. This novel detector technology could act as an additional or alternative detector to the DarkMESA crystal calorimeter. Such a detector would be able to reject events based on the topological signature. For this purpose, a prototype detector was designed, simulated, and tested at the MAMI accelerator at energies around 10 MeV. The primary capability of interest was the detector's ability to reconstruct the initial angles of electrons as they entered the active volume. The detector uses a 22-litre cubic volume of linear alkylbenzene (LAB) based opaque scintillator and 255 wavelength-shifting fibres attached to SiPMs arranged in a triangular grid with 10 mm spacing near a beam entrance window.

Hiermit erkläre ich, dass ich die vorliegende Arbeit selbstständig verfasst und keine anderen als die angegebenen Quellen und Hilfsmittel (dazu zählen auch KI-basierte Anwendungen oder Werkzeuge) benutzt habe. Sämtliche wörtlichen oder sinngemäßen Übernahmen und Zitate sind kenntlich gemacht und nachgewiesen. Ich versichere, dass ich keine Hilfsmittel verwendet habe, deren Nutzung die Prüferin oder der Prüfer explizit ausgeschlossen hat. Im Anhang A.5 habe ich die verwendeten KI-Tools dokumentiert. Mit Abgabe der vorliegenden Leistung übernehme ich die Verantwortung für das eingereichte Gesamtprodukt. Ich verantworte damit auch jegliche KI-generierten Inhalte, die ich in meine Arbeit übernommen habe. Die Richtigkeit übernommener (KI-generierter) Aussagen und Inhalte habe ich nach bestem Wissen und Gewissen geprüft. Ich habe die Arbeit nicht zum Erwerb eines anderen Leistungsnachweises in gleicher oder ähnlicher Form eingereicht. Mir ist bekannt, dass ein Verstoß gegen die genannten Punkte prüfungsrechtliche Konsequenzen hat und insbesondere dazu führen kann, dass die Studien- und Prüfungsleistung als mit "nicht bestanden" bewertet wird. Die Einschreibung kann für bis zu zwei Jahre widerrufen werden, wenn Studierende zweimal oder häufiger bei Prüfungsleistungen täuschen (§ 69 Abs. 4 und 5 HochSchG).

Jonas Pätschke

Mainz, den 11.02.2026, Jonas Pätschke

Jonas Pätschke
DarkMESA
Institut für Kernphysik
Johann-Joachim-Becher-Weg 45
Johannes Gutenberg-Universität
D-55099 Mainz
`jpaetsch@students.uni-mainz.de`

Table of contents

1. Introduction

DarkMESA is a planned electron beam dump experiment at the upcoming MESA accelerator aimed at detecting signals caused by possible Dark Matter production via a proposed Dark Photon. DarkMESA has begun cooperating with the NuDoubt^{++} collaboration to investigate the use of opaque liquid scintillators as a possible detector medium.

Opaque liquid scintillators are a novel development in the field of liquid scintillators. By introducing wax into the scintillator, topological information of events can be obtained, which would be lost in a typical scintillator, while still retaining excellent light yields.

NuDoubt^{++} plans to use this technology to detect double beta decays ($2\nu\beta^+\beta^+$) of Kr-78, Cd-106, and Xe-124, which are predicted by the Standard Model of particle physics, as well as to investigate the neutrinoless double beta decay $0\nu\beta^+\beta^+$. The latter would provide evidence of physics beyond the Standard Model and indicate the Majorana nature of neutrinos [1].

The use of opaque liquid scintillators in the DarkMESA experiment would allow the identification of Dark Matter interactions at low energies and provide topological information of such events inside the detector. Using these signals, events could possibly be discriminated by reconstruction of the tracks belonging to electrons scattered in Dark Matter interactions.

The aim of this thesis is to construct a prototype detector for reconstructing tracks of electrons provided by the MAMI accelerator. This marks the first time an opaque liquid scintillator detector is constructed to be used as a dedicated electron tracking detector. The main interest is the angular reconstruction of the initial angle of electrons entering the detector, since this would potentially allow for angular reconstruction of scattered electrons in the final DarkMESA experiment.

This thesis is structured as follows: Chapter 2 explains theoretical backgrounds motivating the DarkMESA and NuDoubt^{++} experiments. The planned experimental methods of both experiments, as well as the used technologies in this thesis and their physical foundations are explained in chapter 3. Chapter 4 describes in detail the design of the prototype detector and the process of constructing it. To better understand the potential capabilities of the detector it was simulated in Geant4 as described in chapter 5. The measurements at MAMI using electrons with kinetic energies in the order of 10 MeV, as well as measurements using cosmic ray muons can be found in chapter 6.

2. Theoretical Background

2.1. Dark Matter

2.1.1. Indications for the existence of Dark Matter

Indications for the existence of Dark Matter (DM) come from a variety of astrophysical and cosmological observations at different scales. One of the first hints for its existence came from the observations of F. Zwicky [2] about the velocities of galaxies in galaxy clusters. He noticed that their velocities were too high and could not be explained by the amount of visible light emitted from the cluster. Therefore, he assumed that something ”dark” (in the sense of not emitting light) should have been present. In his original publication (in German), he specifically mentions the words ”dunkle Materie” (Dark Matter) for referring to the additional invisible mass.
Over the years, more observations pointed to the existence of Dark Matter and in the following we will mention some of them.

2.1.1.1. Effect of Dark Matter on the rotation curves of galaxies

Thanks mainly to the work of V. Rubin and collaborators [3], the presence of Dark Matter can be indirectly observed at galactic scales by measuring the galactic rotation curves. The rotation curve of a galaxy describes the relation between stellar velocities and the distance from the galactic core. Using Newtonian physics and equating centripetal and gravitational force:

$$F_Z = F_G \Rightarrow \frac{mv^2}{r} = \frac{GmM(r)}{r^2} \Rightarrow v = \sqrt{\frac{GM(r)}{r}} \tag{2.1}$$

Which means that the velocity should decrease as $\frac{1}{\sqrt{r}}$. However, when looking at the measured rotation curves of galaxies, the rotation velocity is in fact constant for large radii, as can be seen in figure 2.1. This ”flat rotation curve” behaviour can be explained by the presence of a Dark Matter halo with a density proportional to $1/\mathrm{r}^2$, which extends far beyond the galaxy. This halo would then make up over two thirds of the mass of the galaxy. [4]

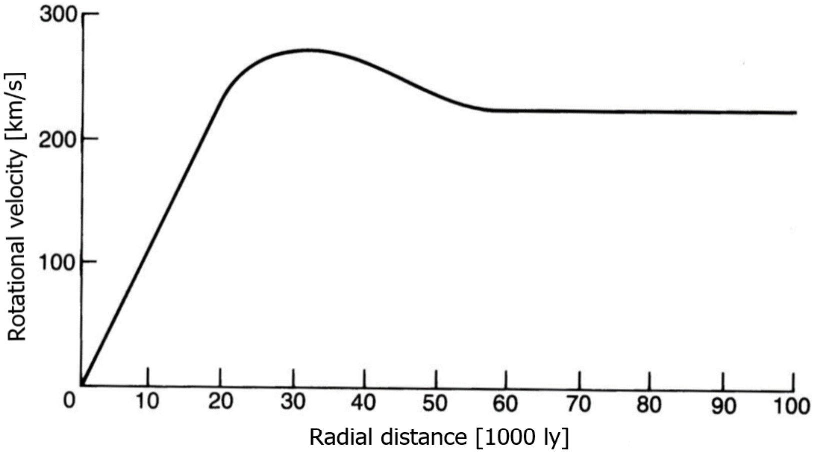

Figure 2.1.: Sketch of the rotation velocity (km/s) with relation to radial distance (ly). The linear behaviour extends up to about 20 ly, the peak and subsequent decline are caused by conventional matter, but due to the effect of the DM halo, the decline is compensated and the velocity remains constant for large distances. [4]

2.1.1.2. Bullet Cluster

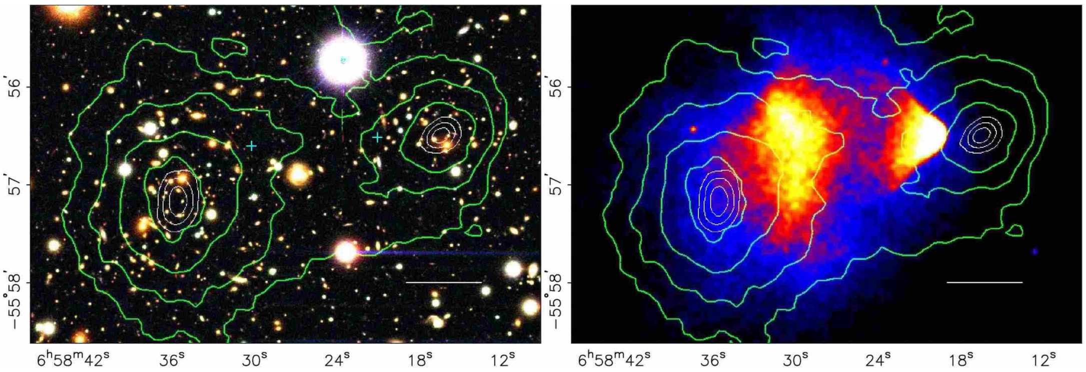

Figure 2.2.: **Left:** Image of the bullet cluster taken by the Magellan Telescopes in the visible light spectrum. The green lines show the weak lensing reconstruction. **Right:** X-ray image of the clusters taken by the Chandra X-ray Observatory. Two large amounts of hot gas can be seen in the middle of the picture.[5]

A direct indication for the existence of Dark Matter on the scale of galaxy clusters can be observed by studying the double galaxy cluster "1E0657-558", commonly known as the "bullet cluster". Two images of this cluster can be seen in figure 2.2. The cluster is divided into two sub-clusters. Both collided in the past. The galaxies of both sub-clusters continued to travel on their original paths. However, between them a large amount of hot gas that previously accompanied both clusters can be observed by looking at the X-ray light produced by the collision (fig. 2.2, right).

By analysing the effect of weak gravitational lensing due to the mass of both subclusters, it can be shown that most of the matter in the galaxies is not comprised of the gas that is now separated, but has passed relatively undisturbed like the galaxies did. The ratio between the mass in the hot gas to the mass of all matter is estimated to be about one sixth. This requires Dark Matter to explain the observed weak lensing and it is a major argument against some classes of modified gravity theories like MOND (Modified Newtonian Dynamics [6]).

2.1.1.3. Cosmic Microwave Background

The cosmic microwave background (CMB) originates from the moment the universe first became transparent. About 380,000 years after the Big Bang, during the so-called Recombination Era, the matter in the universe cooled down enough that the first hydrogen atoms formed from the plasma of electrons and protons present at that time. Photons which previously scattered off free electrons could now travel largely unhindered through the cosmos. Due to the redshift caused by the expansion of the universe, this radiation has been redshifted to microwave wavelengths. Today, the spectrum of the CMB can be well described by a blackbody radiation function with a temperature T = 2.7255 K [7].

Using the Planck satellite, the CMB was mapped with high resolution, as can be seen in figure 2.3. The CMB map shows small fluctuations around the average temperature. These anisotropies were caused by density fluctuations in the plasma before Recombination.

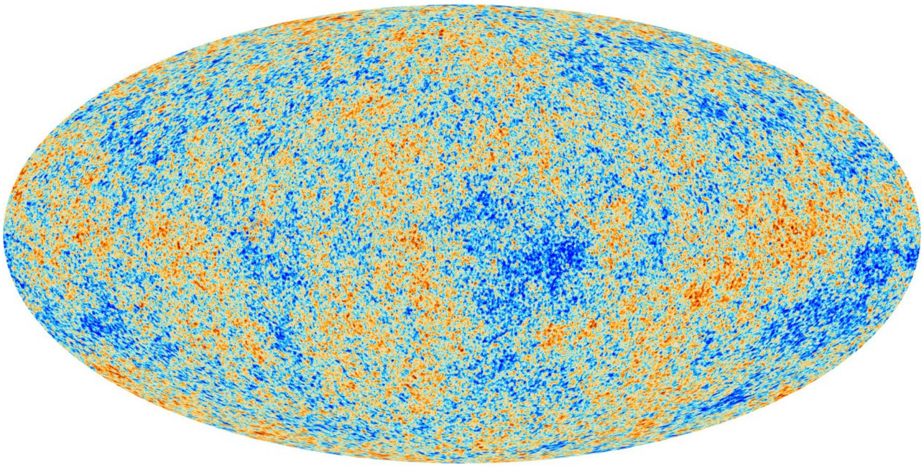

Figure 2.3.: Anisotropies of the Cosmic Microwave Background (CMB) as observed by the Planck satellite. [8]

By fitting the CMB data from the Planck satellite to the Lambda Cold Dark Matter (ΛCDM) cosmological model, a good description of the observed fluctuation spectrum can be obtained. The ΛCDM model is based on the Friedmann-Lemaître-Robertson-Walker (FLRW) metric. With conveniently chosen coordinates, its metric is

$$ds^2 = -dt^2 + R(t)^2 \left(\frac{dr^2}{1-kr^2} + d\theta^2 + sin^2\theta d\phi^2 \right) \ , \tag{2.2}$$

where $R(t)$ is the time-dependent scale parameter, r, θ and Φ spatial coordinates, and k, the space curvature. The curvature k can be rescaled (because of the scale invariance of R, r, and k) to the three possible values -1, 0 or +1, corresponding to an open, flat and closed universe, respectively. Substituting this metric into the Einstein equations yields the Friedmann equations:

$$\frac{\ddot{a}}{a} = -\frac{4\pi G}{3}(\rho + 3P) \tag{2.3}$$

$$\left(\frac{\dot{a}}{a}\right)^2 = \frac{8\pi G}{3}\rho - \frac{k}{a^2} \tag{2.4}$$

where a(t) = R(t)/R$_0$ with R$_0$ being today's value. Eq. 2.4 can be rewritten as

$$\left(\frac{\dot{a}}{a}\right) = H = H_0\sqrt{\frac{1}{a^3}(\Omega_c + \Omega_b) + \frac{\Omega_r}{a^4} + \frac{\Omega_k}{a^2} + \Omega_\Lambda} \ , \tag{2.5}$$

by introducing the appropriate equation of state to obtain $\rho(t) \propto a(t)^{-3(1+\omega)}$. $H = \dot{a}/a$ is the Hubble parameter and H$_0$ today's value. Ω is the density parameter and determines the density of the various kinds of energies making up the universe:
$\sum \Omega_i = 1$.

- $\Omega_c \longrightarrow$ cold DM density
- $\Omega_b \longrightarrow$ baryonic matter density
- $\Omega_r \longrightarrow$ radiation density
- $\Omega_k \longrightarrow$ density due to curvature
- $\Omega_\Lambda \longrightarrow$ dark energy density

By fitting this model to the Planck satellite data, these parameters can be determined:

- $\Omega_c = 0.2589 \pm 0.0057$
- $\Omega_b = 0.0486 \pm 0.0010$
- $\Omega_\Lambda = 0.6911 \pm 0.0062$
- $\Omega_r \sim 10^{-4}$
- $\Omega_k \sim 0$

This means that only about 5% of the matter in the universe is baryonic matter while the majority of it is constituted by Dark Matter and the even more mysterious Dark Energy. [9]

2.1.2. Dark Matter candidates

There are several different types of proposed Dark Matter candidates. Some of the most popular are: (heavy or sterile) neutrinos, WIMPs (**W**eakly **I**nteracting **M**assive **P**articles) and axions. Alternatively it has also been attempted to explain DM using baryonic matter for example using MACHOs (**MA**ssive **C**ompact **H**alo **O**bjects) or by modifying the theory of gravity.

Since neutrinos do have mass, it was thought that the neutrino background radiation could be used to explain DM, but due to their very small mass, neutrinos can only explain a tiny part of DM. Neutrinos are examples of ”hot” DM, since they were relativistic in the early universe. Explaining DM with non-radiant massive objects made of normal baryonic matter (MACHOs), such as brown dwarfs or black holes, also proved to be not possible or unlikely, given our current knowledge. [4]

2.1.2.1. WIMPs

WIMPs are proposed particles outside the SM with masses ranging from the GeV to the multi-TeV scale. After the Big Bang, these particles would have decoupled from the thermodynamic equilibrium of creation and annihilation, when their reaction rate became smaller than the expansion rate of the universe. The lightest supersymmetric particle (LSP) is an example of a WIMP candidate. Supersymmetry (SUSY) is a proposed additional symmetry shared by bosons and fermions which could explain several currently open questions in particle physics. SUSY further has the property of unifying the space-time symmetry with the inner symmetries of particles. It implies a fermion-boson symmetry such that every SM particle has a SUSY partner, which has a spin difference of 1/2 and significantly higher mass (see tab. 2.1). A possible LSP candidate is the neutralino, a linear combination of a Photino, a Zino and two Higgsinos, or the gravitino, the SUSY partner of the graviton. [4]

Spin	SM particle	SUSY partner	Spin
1/2	Leptons Quarks	Sleptons Squarks	0
1	Gluon $W^{\pm}$ Z^0 Photon	Gluino Wino Zino Photino	1/2 0
0	Higgs	Higgsino	1/2
2	Graviton	Gravitino	3/2

Table 2.1.: Elementary particles of the SM and their SUSY partners. (Adapted from [4])

WIMPs became a primary interest in the search for Dark Matter due to the so-called WIMP-miracle. This is based on the hypothesis that in the early universe Dark Matter particles were in thermal equilibrium with SM particles until a "freeze-out" took place:

$$n_\chi \langle \sigma(\chi\chi \to SM) v_\chi \rangle > H(t), \tag{2.6}$$

where n_χ is the number density of DM, $\Gamma = \langle \sigma(\chi\chi \to SM) v_\chi \rangle$ the thermally averaged annihilation rate, v_χ the DM velocity and H the expansion rate of the universe (Hubble constant). When this condition (eq. 2.6) is met, DM particles would no longer be able to efficiently annihilate and therefore decouple. The point of the freeze-out is determined by the coupling strength between DM and SM particles. This therefore also determines the expected number density in the current universe (thermal relic), which can be seen in figure 2.4. By taking into account the required DM density to explain cosmological observations, the expected DM coupling can be extrapolated and therefore also the mass of DM particles. The WIMP-miracle describes the coincidence that, when assuming a DM mass near the electroweak scale and the coupling of weak force, the calculated DM density matches the observed density extremely well.
However, this was discovered in the late 1990s and DM searches based on the WIMP-miracle in the last two decades did not find any indication for the existence of WIMPs. This indicates that other candidates for DM particles have to be considered instead. [9]

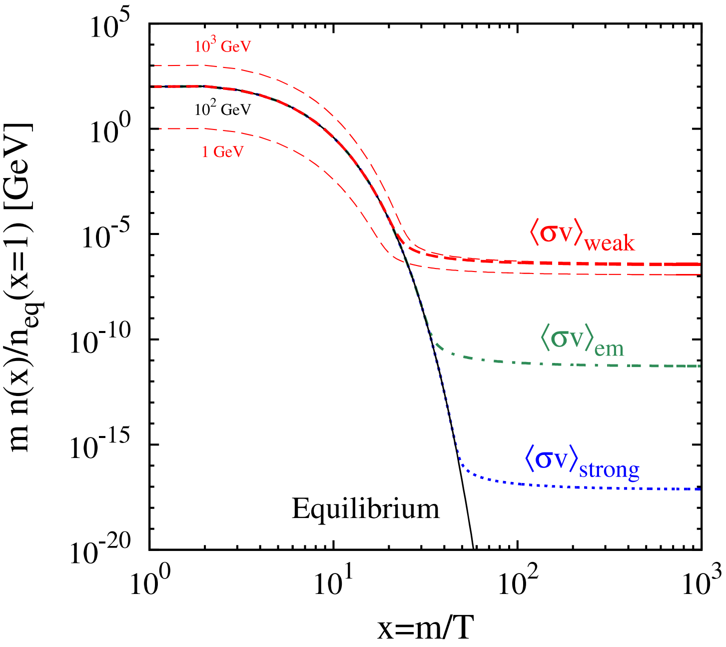

Figure 2.4.: Evolution of DM density before and after freeze-out took place. The number density of DM particles is given as a function of x = m/T, which is a proxy for time. The point in time of freeze-out is determined by the annihilation cross section $\langle \sigma v \rangle$ and therefore the coupling between SM and DM particles. Different couplings lead therefore to different DM relic densities. [10]

2.1.2.2. Axions

Axions were originally postulated to explain the absence of CP-violation [11] in the strong interaction. They are neutral pseudoscalars ($\mathrm{J}^{\mathrm{P}} = 0^-$) similar to neutral pions, but only have a very small mass of 10^{-3} to 10^{-6} eV and decay, like π^0 into two photons:

$$A^0 \longrightarrow \gamma\gamma \tag{2.7}$$

Because their coupling is relatively weak, their lifetime is long. Axions are postulated to be created by reactions with pions which can happen in stars with similar rates to neutrino production. Due to their low mass, Axions are thermal and as such constitute hot Dark Matter like neutrinos. Some models predict a possible condensation of Axions, which would allow them to act as cold Dark Matter, despite their low mass. [4]

2.1.3. The Dark Photon

Many extensions of the SM that try to explain Dark Matter predict an extra U(1) gauge group. The Dark Photon is a hypothetical particle associated with such a gauge group. Its rest mass is thought to be in the MeV to GeV range. The Dark Photon would be the gauge boson of the dark sector and could interact with the photon of the SM:

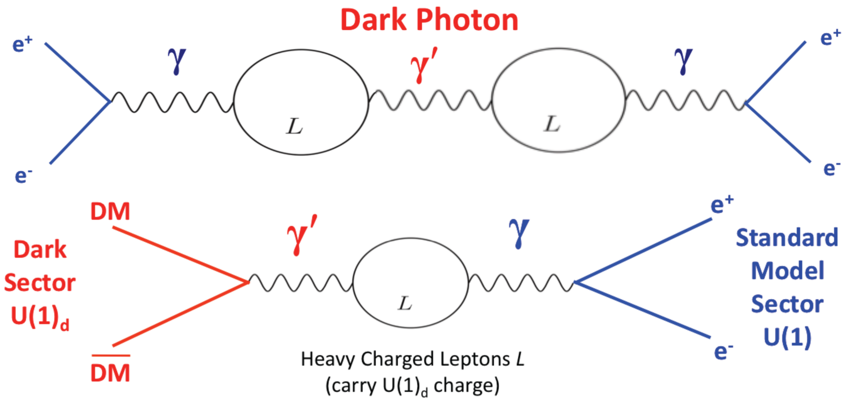

Figure 2.5.: Feynman diagrams showing the interaction of the Dark Photon. **Top**: Kinetic mixing between the Dark Photon and the SM photon. **Bottom**: Interaction between the SM and the Dark Sector via the Dark Photon. The loops in both diagrams represent pairs of charged leptons that could couple to the SM photon and the Dark Photon. [12]

If the mass of the Dark Photon is smaller than that of the Dark Matter particle contained in the dark sector, it would decay into a pair of charged leptons, as can be seen in fig. 2.5. If its mass would be larger than that of the DM particles, it would primarily decay into those. [12]

2.2. Double beta decay

The double beta decay is a rare nuclear process in which the atomic number (Z) changes by two while the number of nucleons (A) remains constant. This can happen if decay via single beta decay (the emission of a single electron or positron) is forbidden or suppressed due to spin or energy configurations.

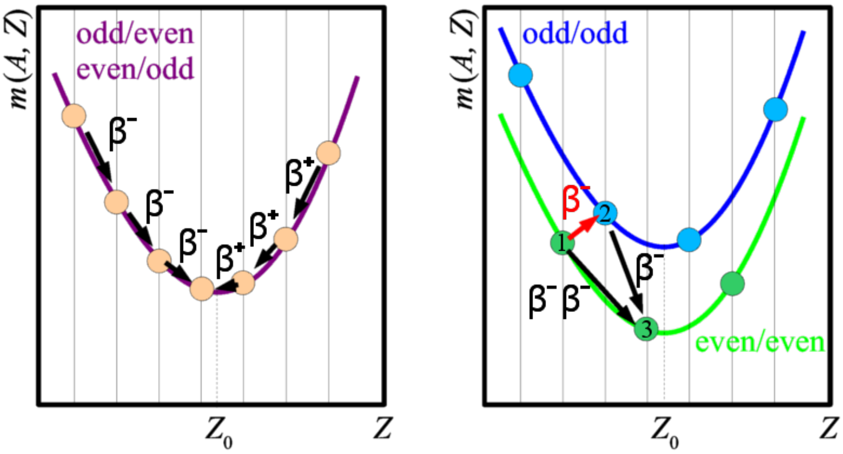

Figure 2.6.: Nuclear mass parabolas for nuclides with even/odd or odd/even atomic to nucleon numbers (**left**) and odd/odd pairings (**right**). β^- decay for nuclide 1 to nuclide 2 is forbidden and only a double β decay to nuclide 3 is possible. [13]

Nuclear pairing interactions cause nuclei with both, an even number of protons and neutrons, to be more strongly bound than those with even-odd or odd-odd pairings. Therefore a decay of an even-even nucleus via beta decay can be suppressed if the odd-odd nucleon following the decay would be more tightly bound. Instead these nucleons can decay via double beta decay into the next even-even nuclei:

$$2\nu\beta^-\beta^- : (A, Z) \rightarrow (A, Z+2) + 2e^- + 2\bar{\nu} \tag{2.8}$$

$$2\nu\beta^+\beta^+ : (A, Z) \rightarrow (A, Z-2) + 2e^+ + 2\nu \tag{2.9}$$

There are also two additional modes of double beta decay involving the capture of electrons:

$$2\nu\text{EC}\beta^+ : (A, Z) + e^- \rightarrow (A, Z-2) + e^+ + 2\nu \tag{2.10}$$

$$2\nu 2\text{EC} : (A, Z) + 2e^- \rightarrow (A, Z-2) + 2\nu \tag{2.11}$$

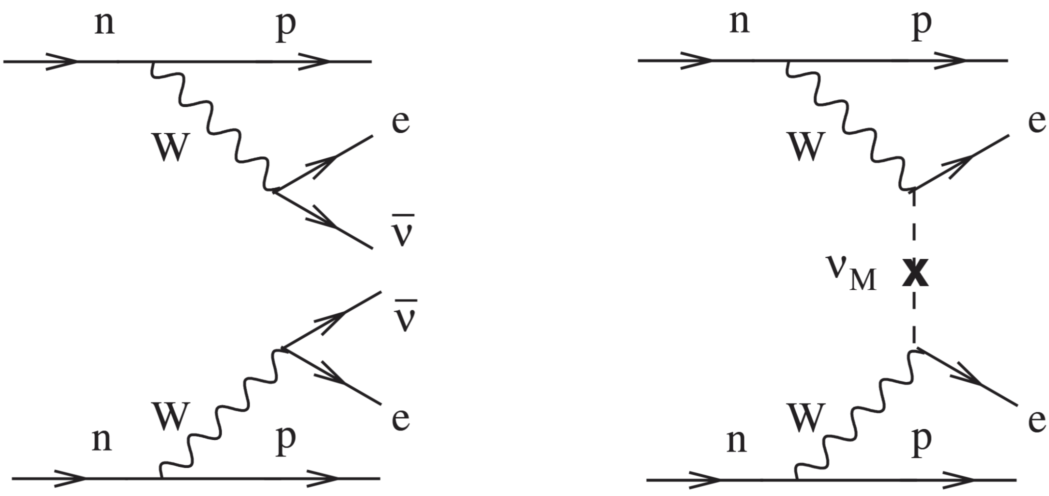

Figure 2.7.: Feynman diagrams of $2\nu\beta^-\beta^-$ (**left**) and $0\nu\beta^-\beta^-$ (**right**) decays. The second shows an interaction via a Majorana neutrino. [14]

Figure 2.7 shows the Feynman diagrams of $2\nu\beta^-\beta^-$ (left) as well as an additional decay mode, the postulated neutrinoless (0ν) double beta decay:

$$0\nu\beta^-\beta^- : (A, Z) \rightarrow (A, Z+2) + 2e^- \tag{2.12}$$

or

$$0\nu\beta^+\beta^+ : (A, Z) \rightarrow (A, Z+2) + 2e^+ \tag{2.13}$$

This is only possible if the neutrino is its own antiparticle, as postulated by E. Majorana, which would violate lepton number conservation and indicate physics beyond the Standard Model [15]. Since the electron (positron) mass is several orders of magnitude smaller than that of the nucleus, the recoil on the nucleus is negligible. For the $2\nu\beta\beta$ decay its energy (Q-value) is split up between the electrons (positrons) and (anti-)neutrinos, which causes the measurable energy spectrum of electrons (positrons) to be continuous (see fig. 2.8).

Neutrinos interact only weakly and thus measuring their energy is challenging. In the case of $0\nu\beta\beta$ decay the entire energy of the decay goes into the electrons (positrons) and the sum of both energies is equivalent to the Q-value. This could be seen as a sharp peak in the measurable energy spectrum of the decay (see fig. 2.8, right, peak).

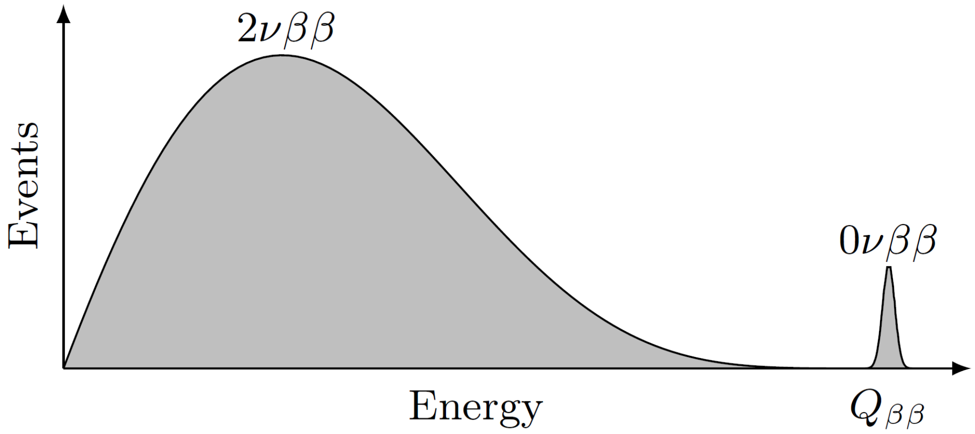

Figure 2.8.: Normalized theoretical energy spectra of $2\nu\beta\beta$ and $0\nu\beta\beta$ decays measurable inside the detector. The emission of neutrinos caused a broad continuous spectrum for $2\nu\beta\beta$. In contrast a sharp peak at the Q-value of the decay can be seen for the neutrinoless decay. [16]

While the $2\nu\beta\beta$ decay is a known nuclear process that has been observed experimentally in several isotopes, the half-lives measured are in the order of 10^{19} to 10^{21} years. This is due to the weak second order nature of the interaction. For neutrinoless decay modes the half-lives are expected to be even longer.
Detecting $0\nu\beta\beta$ brings experimental challenges. A good energy resolution and reliable background discrimination are needed, as well as a high concentration of double beta isotopes with a high Q-value.
The NuDoubt^{++} aims to detect the $0\nu\beta^+\beta^+$ decay, utilizing its high energy resolution and particle identification ability of its hybrid opaque scintillator detector (see sec. 3.3).

3. Experimental Background

3.1. The MESA accelerator

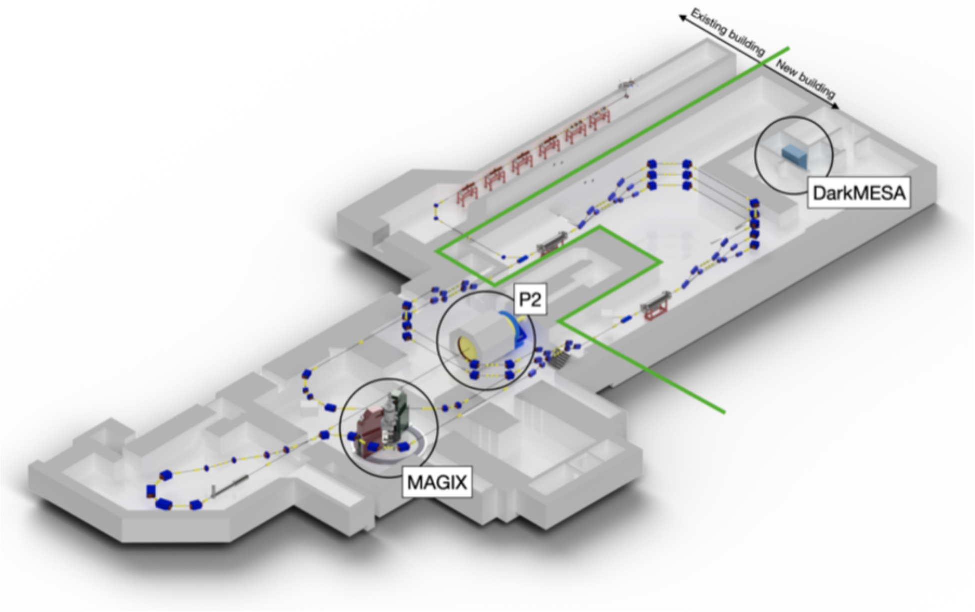

Figure 3.1.: Floor plan of the MESA facility. The DarkMESA experiment is situated directly in the axis of the P2 beam line. [17]

The **M**ainz **E**nergy-Recovering **s**uperconducting **A**ccelerator (MESA) is currently under construction at the Institute of Nuclear Physics of the Johannes Gutenberg University of Mainz. In figure 3.1 an overview of the facility is shown. Three experiments are planned and will be served by the accelerator in two operating modes. The fixed target experiment P2 will use the external beam (EB) mode to determine the weak mixing angle at high accuracy by measuring parity violation asymmetry. The beam dump experiment DarkMESA will be operating simultaneously to P2, searching for Dark Matter that could be produced in the beam dump. In the second operating mode, MESA will be run as an energy recovery linac (ERL). The ERL operation will be exploited by the MAGIX experiment, this is possible as MAGIX will use a windowless gas jet target. MAGIX has a broad physics program ranging from Dark Photon searches to hadron and nuclear physics. The different operational parameters of MESA can be found in tab. 3.1. In EB mode the beam can be polarized, with a polarization flip frequency of 1 kHz, while in the ERL mode the beam will be unpolarized but delivered at high intensity in the mA range. By recirculating the non scattered electron bunches and injecting them at a 180° phase shift into the accelerator cavities, their energy will be recovered in this mode. [18]

Operating Mode	Maximum energy	Current	Experiments	Current goals
External Beam Mode (EB)	155 MeV	150 µA	P2, DarkMESA	Determining the Weinberg angle, Dark Matter search
Energy recovery linac (ERL)	105 MeV	1 mA	MAGIX	Measurement of the proton radius, Dark Matter search and more

Table 3.1.: Overview of the two operation modes of the MESA facility.

3.1.1. DarkMESA

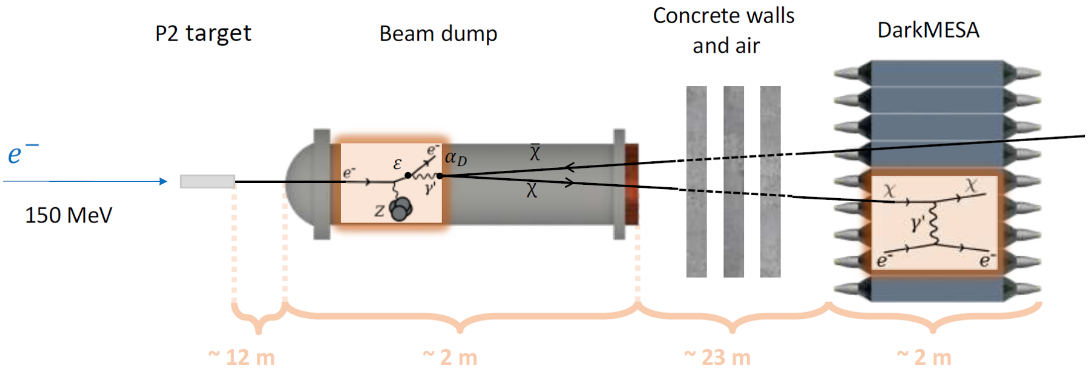

Figure 3.2.: Working principle of the DarkMESA Phase A experiment. The Feynman diagrams show the relevant physical processes for the detection. [19]

The DarkMESA experiment at MESA will search for dark sector particles such as the Dark Photon. By placing the experiment downstream of the fixed target experiment P2 outside of the accelerator hall (see fig. 3.1), the electron beam of MESA will hit the beam dump behind P2, where the Dark Photon can be produced in a bremsstrahlung-like process or with electron-positron annihilation. Dark Photons will then decay into pairs of DM particles. Whether they decay into particle/antiparticle pairs or into two different particles depends on the model considered. These DM particles will travel through several layers of concrete walls towards the DarkMESA detector. Inside the detector, the DM particles can interact with electrons via Dark Photon exchange causing Cherenkov radiation which can be detected (see fig. 3.2). The use of a Cherenkov detector has the advantage of a relatively low sensitivity to background neutrons and their fast response. Potential media are PbF_2 and lead glass, both have a high density, which is ideal for calorimetry.

By using the relatively low energy MESA beam, the experiment can be conducted below the muon and pion production thresholds and an additional beam-related neutrino background can be avoided. Additionally by placing the experiment behind a large amount of concrete, radiation produced by the accelerator can be shielded. To exclude further background radiation, such as cosmic rays or natural radioactivity, a veto system consisting of two layers of plastic scintillator detectors and a lead layer in between, surrounding the Cherenkov detectors will be installed (see fig. 3.3).

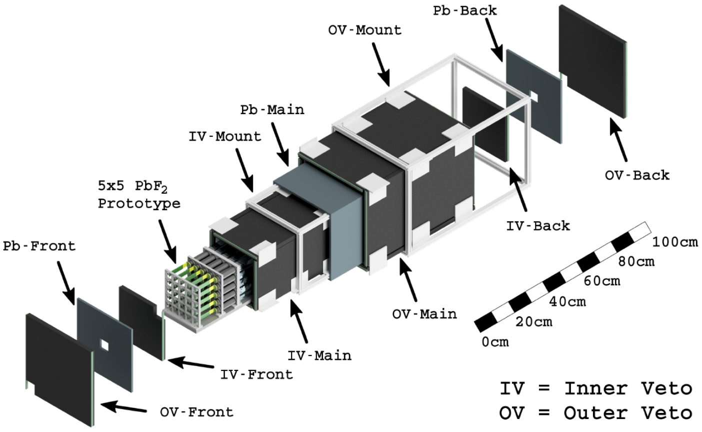

Figure 3.3.: Construction of the DarkMESA Phase A prototype detector. PbF_2 crystals are planned to be used as the Cherenkov medium. [20]

This Cherenkov detector however is not the only detector technology being investigated for the use in the DarkMESA experiment. This thesis focuses on the development of an opaque liquid scintillator (see sec. 3.3) detector prototype to investigate the feasibility of using this technology as either an alternative detector concept or a complementary detector used for the second stage of the experiment.

A detector of this design could offer several advantages compared to a Cherenkov detector. Of utmost importance for this thesis is the potential ability to discriminate detector signals based on their topological signature by reconstruction of the path and angle of electrons due to potential electron–Dark Photon interactions. This could be used to reject signals if they show a scattering angle not possible for those events.

Another advantage is the ability for particle identification based on the event topology and as explained in section 3.3.2 a hybrid scintillator could reject events based on the Cherenkov-Scintillation light ratio.

3.2. The NuDoubt^{++} Experiment

NuDoubt^{++} is a novel experiment being devised at the Institute of Physics in Mainz to investigate the Majorana nature of the neutrino. It will use a combination of several novel experimental techniques for the measurements of two-neutrino double weak decays ($2\nu2\beta+$ and $2\nu\mathrm{EC}\beta+$) and to establish new limits of neutrinoless double beta decay ($0\nu\mathrm{EC}\beta+$ and $0\nu2\beta+$).

3.2.1. Detector

The NuDoubt^{++} detector will combine the use of opaque (sec. 3.3.1) and hybrid (sec. 3.3.2) liquid scintillators, as well as the usage of novel optimized wavelength shifting fibres (OWLs, sec. 3.5.1). The primary isotopes for investigating the mentioned decay are Kr-78, Cd-106, and Xe-124.

A render of the planned detector can be seen in figure 3.4. A cylindrical volume with a diameter of 110 cm is filled with the hybrid-opaque scintillator and OWL fibres in a triangular grid with 1 cm spacing. The radioactive isotopes will be loaded into the scintillator directly. The readout of each fibre will be done by using SiPMs at both fibre ends.

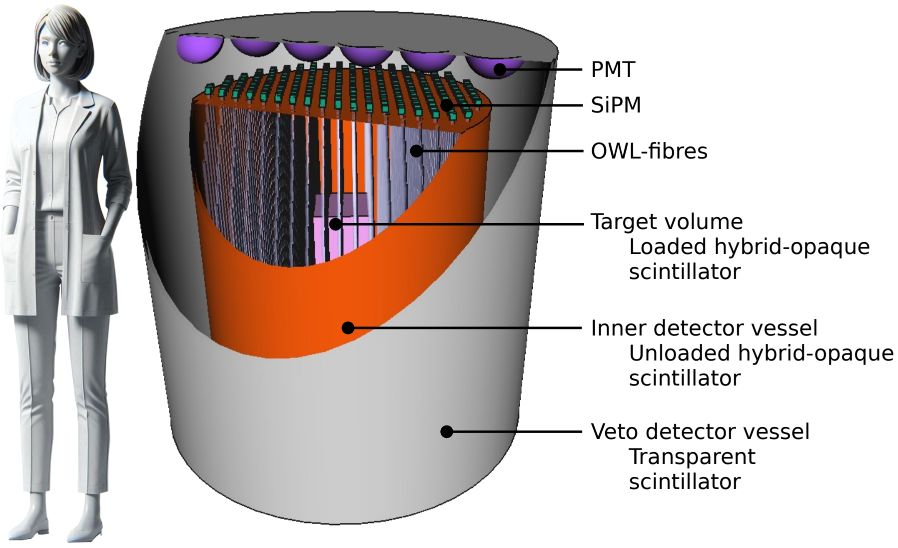

Figure 3.4.: Render of the planned NuDoubt^{++} detector. [1]

This combination of hybrid and opaque scintillator technologies allows for sophisticated particle identification and energy resolution, as described in sections 3.3.2 and 3.3.1.

3.3. Scintillation

Scintillators are materials that are used to convert the kinetic energy of a particle into visible light. This is done by direct ionisation due to charged particles, or indirect ionisation for uncharged particles, e.g. a photon Compton-scattering off an electron, which then ionises the medium.
Scintillators are divided into two types: Organic scintillators, which mainly rely on the electronic structure of the carbon atom and inorganic scintillators, where the electronic band structure found in crystals causes light emission. The processes in organic scintillators will be explained in more detail, since only organic scintillators were used within the scope of this thesis.

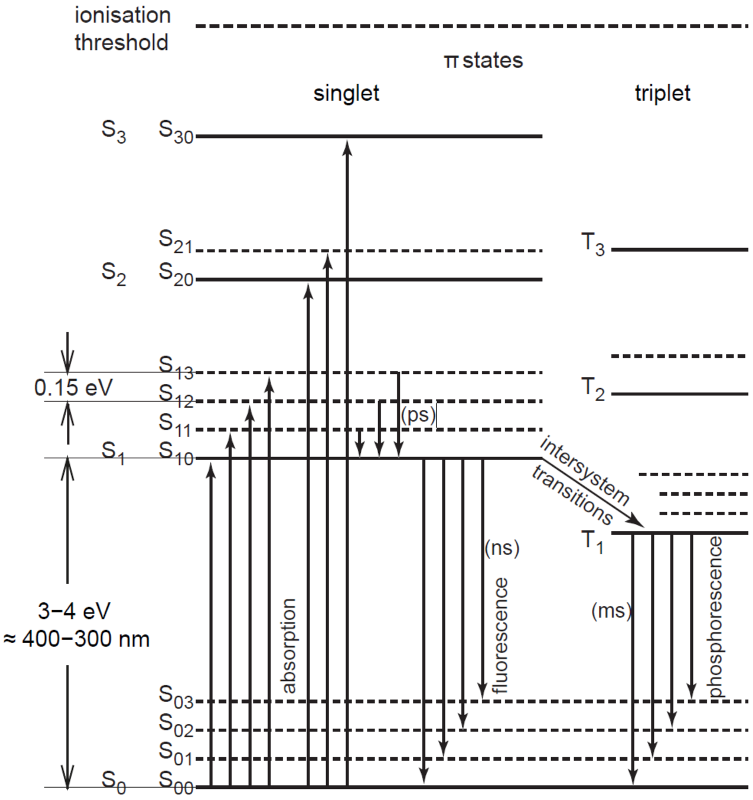

Figure 3.5.: Typical energy levels for scintillator electrons in organic molecules. [21]

A typical energy level scheme for organic molecules can be seen in figure 3.5. Absorption of energy causes the excitation of electrons from the ground state S_{00} to higher levels (S_{1i}, S_{2i}, S_{3i}, ...). They then de-excite from the S_{ni} states to the S_{0n} states radiationless in picoseconds (Stokes shift). The de-excitation from S_{n0} to the ground states emits light (eV range) and takes place in the nanosecond range (prompt fluorescence).

For a fraction of molecules the T_{1i} triplet states can be populated by radiationless inter-system transitions. Since T_{1i} states are metastable, the decay from them to S_{0i} takes place in the millisecond range (phosphorescence). If energy is absorbed while the T-levels are occupied, the electrons can undergo transitions back to the S-levels, followed by immediate de-excitation. This can lead to delayed fluorescence (µs to ms).
Due to the delayed signal, phosphorescence and delayed fluorescence should be avoided if possible. This can both be suppressed by using very pure organic materials.

In order to make a scintillator transparent to its own light, the Stokes shift has to be significant. This can be achieved by adding additional agents into the scintillators, called fluors. This is also used to shift the emitted light towards wavelengths better suited for detection by photosensors. For example, the primary scintillator used by the NuDoubt^{++} collaboration and in the detector built in this thesis is LAB (linear alkylbenzene). The emission spectrum of LAB can be seen primarily in the UV range. Using PPO (2,5-Diphenyloxazole), the emission spectrum is shifted to the visible light range (see fig. 3.6).

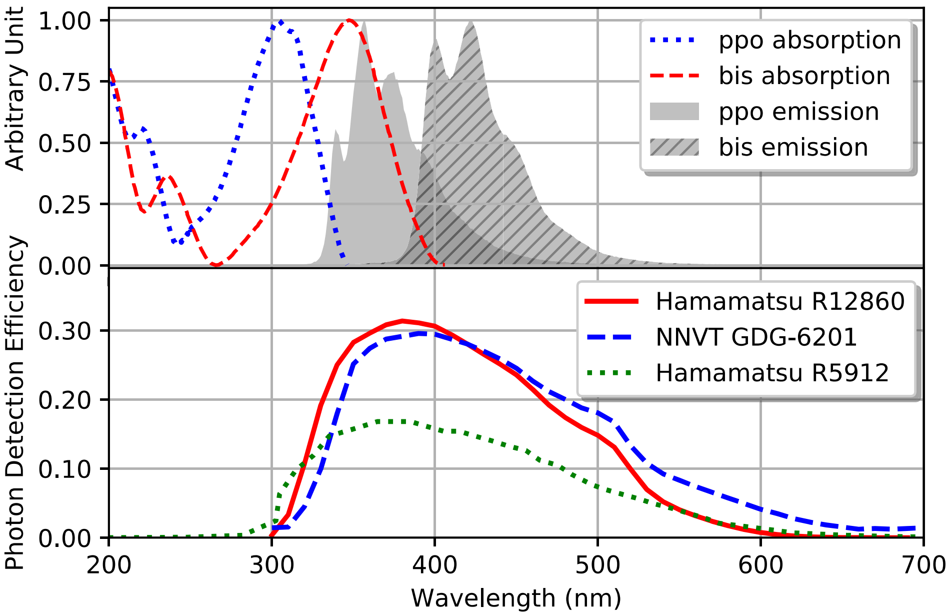

Figure 3.6.: Absorption and emission spectra of PPO and BIS, two commonly used fluors, as well as quantum efficiency curves for three different photomultiplier tubes. [22]

3.3.1. Opaque liquid scintillators

Opaque liquid scintillators offer a novel alternative approach in the use of liquid scintillators. While normally a scintillator would be made as clear (i.e. reducing scattering and self-absorption) as possible to the light produced, they are made opaque by the addition of additives, most commonly a type of wax. Due to this, the light produced by the scintillation is Mie-scattered. In combination with high wax concentration and therefore short scattering lengths, the produced light is confined to its point of origin by a random-walk.

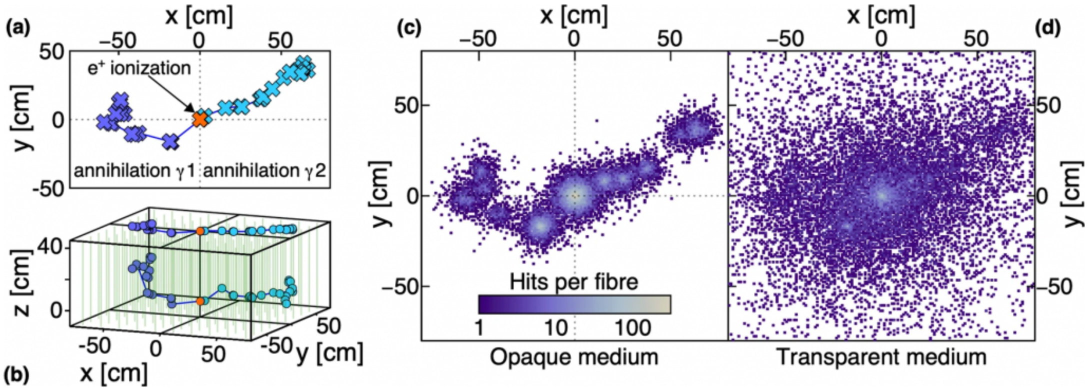

Figure 3.7.: (a) shows the x-y projection of the energy deposition due to a positron and (b) the three-dimensional extent. (c) shows a comparison between the event in a transparent and opaque medium. [23]

When a particle, for example an electron, interacts with the scintillator and creates light, this light is then confined to a broad track for high energies or just a short path appearing as a ”blob” (bulky light object). These are usually confined to the size of a few centimetres.

In contrast a photon could produce multiple Compton-scattering events and create several separated blobs. Therefore, for example a positron decaying into two gammas can also be identified based on its event topology (see fig. 3.7).

The readout of an opaque detector can of course not be performed with photo sensors on the exterior surfaces of the volume like with a traditional scintillation detector. Wavelength shifting fibres (WLS, see sec. 3.5) have to be placed throughout the volume to extract light.

The scattering length of opaque scintillators is typically in the order of millimetres and the attenuation in the order of several metres. With this, every photon has many chances to be scattered and eventually hit a WLS fibre, and a high light yield can be achieved.

3.3.2. Hybrid scintillators

Hybrid scintillation detectors take advantage of the particle-dependent ratio between Cherenkov and scintillation light. Heavier particles are closer to the Cherenkov threshold and therefore produce less Cherenkov light, compared to lighter ones. Gamma photons produce no Cherenkov light on their own and the Compton scattered electrons they produce are often close to the Cherenkov threshold or below it. Figure 3.8 shows how this ratio can be used in combination with opaque liquid scintillators (sec. 3.3.1) for particle identification.
Currently, there are two practical approaches to hybrid scintillators, water-based and hybrid-slow. In water-based hybrid scintillators, small quantities of organic liquid scintillator are suspended in water by the use of small micelles via surfactant interactions. 1-10% of the mixture is scintillator. This is done to reduce the amount of scintillation light in order to be able to separate the Cherenkov light peak from the scintillation light using fast electronics. The advantage of this approach is a cost reduction and a safe detector medium with respect to flammability. This, however, decreases the light yield of the medium.

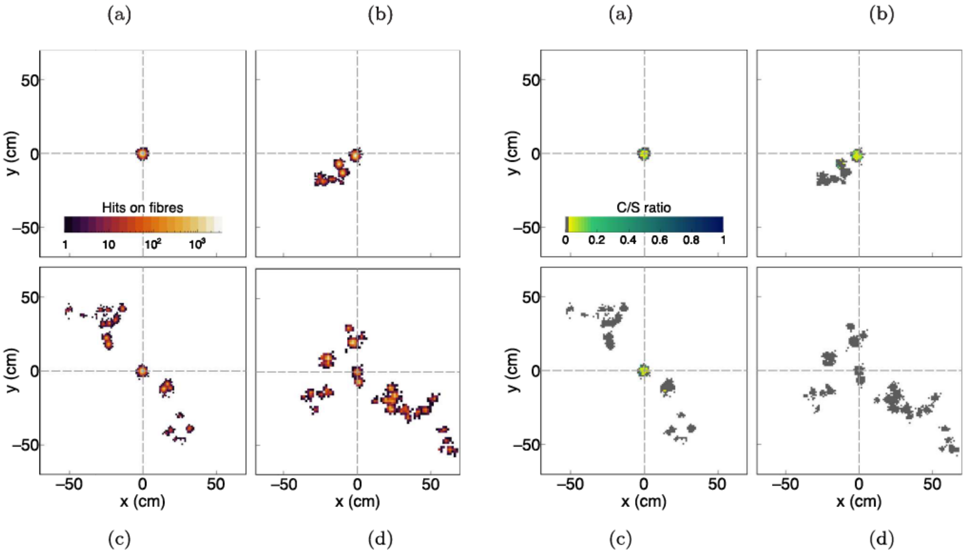

Figure 3.8.: Particle identification strategy in NuDoubt^{++}. The **left** panels show the fibre hits for four different events and the **right** panels visualises the Cherenkov-scintillation ratio. Geant4 simulation of a 2.8 MeV electron (a), a gamma photon with 2.8 MeV (b), single positron of 1.78 MeV kinetic energy, and (d) two positrons of 0.38 MeV kinetic energy each. All events deposit the same amount of energy. [1]

Hybrid-slow scintillators aim to exploit intrinsically slow fluors and solvents in the scintillator. Using this, the scintillation light is delayed and a Cherenkov light peak becomes distinguishable at the beginning of light emission. By not reducing the amount of scintillator in the media, like water-based hybrid scintillators do, the light yield is higher, which leads to a better energy resolution and low detection thresholds can be achieved. Normally this approach would decrease the spatial resolution of the detector, but this can be negated by the introduction of opacity into the detector as explained in section 3.3.1. [1]

3.4. Silicon photomultipliers

Silicon Photomultipliers (SiPM) are solid-state photodetectors used to detect low levels of light with single photon sensitivity. When a photon is absorbed in the depletion zone of the detector, it creates an electron-hole pair (see fig. 3.9). A charge avalanche is created due to the applied voltage. This creates an amplification gain of about 10^6. The SiPM is made up of multiple pixel cells in typical size a range of 15-70 µm. Because of the small size of the pixels, only single cells are usually hit and the number of hit pixels is proportional to the number of photons or the light intensity.

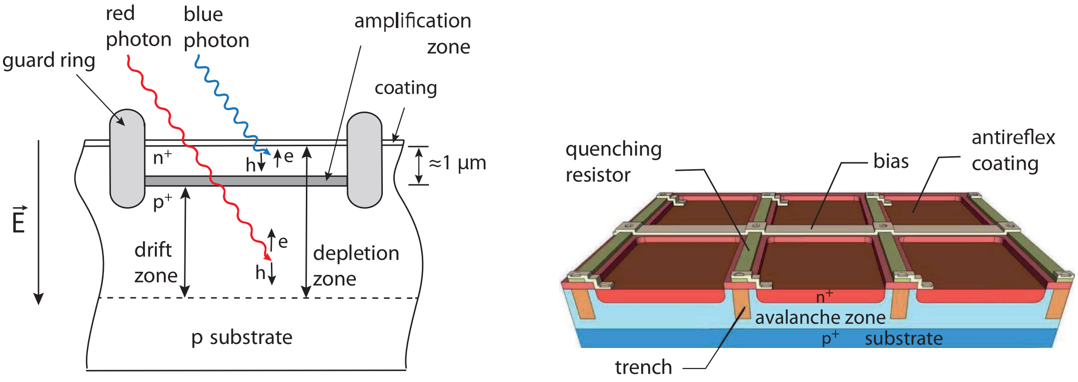

Figure 3.9.: **Left:** Schematic of a single SiPM cell. An incoming photon is absorbed at different depths depending on its wavelength. The charge carriers are amplified in the amplification zone. **Right:** Render of a SiPM array showing multiple pixel cells separated by trenches to reduce crosstalk between cells. [21]

To operate SiPMs a voltage is applied, which is typically about 10-15% higher than the breakdown voltage. After an avalanche is created, it is quenched by a resistor. This resistor also decouples the individual cells and determines the decay time of the pulse. The rise time is given by the avalanche process and has a fast peaking time (≈ 0.5 ns). [21]

3.5. Wavelength-shifting fibres

To extract light from scintillator detectors, wavelength shifting (WLS) fibres can be used. They are a combination of optical fibres and wavelength shifters. When a photon of the scintillator medium hits a WLS fibre, it is absorbed by it and re-emitted at a different wavelength. The photon is then emitted at a new angle. By taking advantage of total internal reflection, the photon can then be trapped in the fibre and travel along it until it hits a photodetector on one of the fibre ends. But the photon can also hit the fibre surface at an angle smaller than the critical angle for total internal reflection. This creates relatively large loss cones, as seen in figure 3.10. [21]

3.5.1. Optimized wavelength-shifting fibres

Optimized wavelength shifting (OWL) fibres are a novel development in the use of wavelength shifting fibres that aim to increase the amount of captured shifted light in the fibre by moving the wavelength shifter to the surface. This technology is based on the development of wavelength-shifting modules (WOMs) for the IceCube-Upgrade [24].
For ordinary WLS fibres, if the point of emission is at the centre of the fibre, only the axial angle of θ_z contributes to the incident angle α, limiting the capture efficiency. By shifting the point of emission to the surface of the fibre, the azimuthal angle θ_ϕ also contributes and the chance for total internal reflection increases. Because of this, only the smaller "loss cones" seen in figure 3.10(right) are relevant in contrast to the capture cone for ordinary fibres. Using this, the capture efficiency of these fibres could be increased to almost 40% instead of the usual efficiency of about 5% for commercially available ordinary fibres. [25]

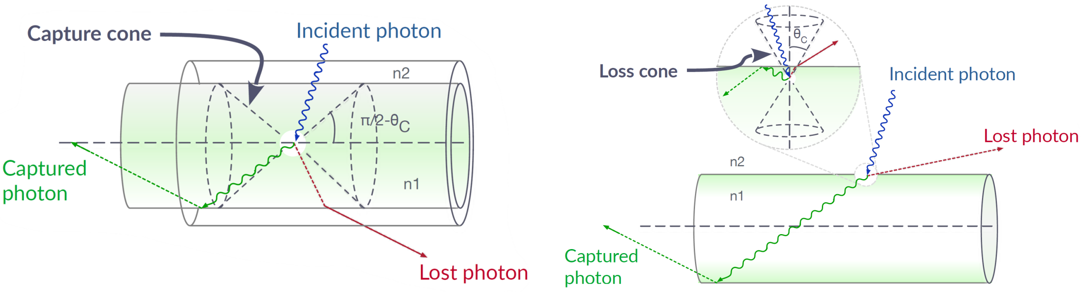

Figure 3.10.: Comparison between ordinary WLS fibre (**left**) emission and capture and the improved capture mechanism of OWL fibres (**right**). The point of emission has been moved near the surface of the fibre, by doing this only photons emitted inside the small loss cone are not captured by total internal reflection. [26]

3.5.2. Bubo fibres

As mentioned in section 3.3, the scintillator used for NuDoubt^{++} and potentially DarkMESA, is LAB based. LAB can act as a mild solvent and dissolve the wavelength shifting paint of the OWL fibres or even a plastic fibre core. In order to prevent this, the fibre is placed into a plastic or glass tube.
These new fibres are called Bubo fibres (see fig. 3.11). The name derives from the biological genus "Bubo", which includes the biggest species of owls, like the Eurasian eagle-owl ("Bubo bubo").

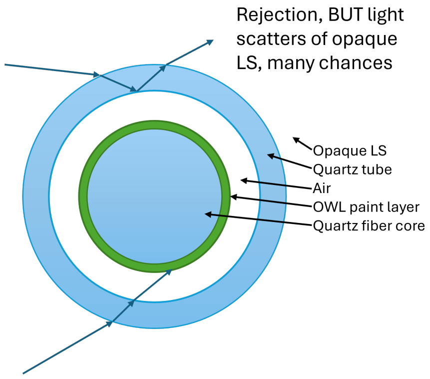

Figure 3.11.: Sketch of the Bubo fibres used in the DarkMESA prototype detector developed in this thesis. Both the tube and the fibre core are made of fused quartz glass (see sec. 4.1.1).

The addition of the tubes to the fibre has an effect on the final trapping efficiency of the fibres. Due to the addition of an air gap between the OWL fibre and the tube, the total internal trapping efficiency inside the OWL fibre is improved, as the difference between the reflective index of air and the fibre is greater than that between the fibre and the scintillator. The tube can also cause additional total internal reflection and Fresnel losses at the tube-air interface. However, due to the properties of the opaque scintillator, light rejected at this interface is not necessarily lost: after scattering within the scintillator, it may return to the fibre and has multiple opportunities to pass through the interface.
The larger radius of the Bubo fibres reduces the total amount of active scintillator volume in the detector and therefore its light yield and potentially its energy resolution. A smaller tube would alleviate this to some extent, but most commercially available fibres have wall thicknesses of 1 mm or greater and thinner tubes could prove to be mechanically challenging, especially for the final planned fibres with lengths of over one metre. [27]

4. Prototype detector

The purpose of the prototype detector being developed in the scope of this thesis is to investigate the possible advantages of liquid opaque scintillators for the DarkMESA experiment, acting as a proof-of-concept for the proposed capabilities such a detector can offer.
The opaque liquid scintillator allows for reconstruction of event topologies, which can be used to discriminate events based on their signature and enables particle identification. By analysing the event topology it could be possible to determine the scattering angle of electrons after a potential Dark Matter interaction and discriminate events based on it. The energy resolution of the detector was also being investigated.
To test these capabilities the detector was designed for an electron beam experiment with the MAMI accelerator using a low current 14 MeV e^- beam.

4.1. Detector design

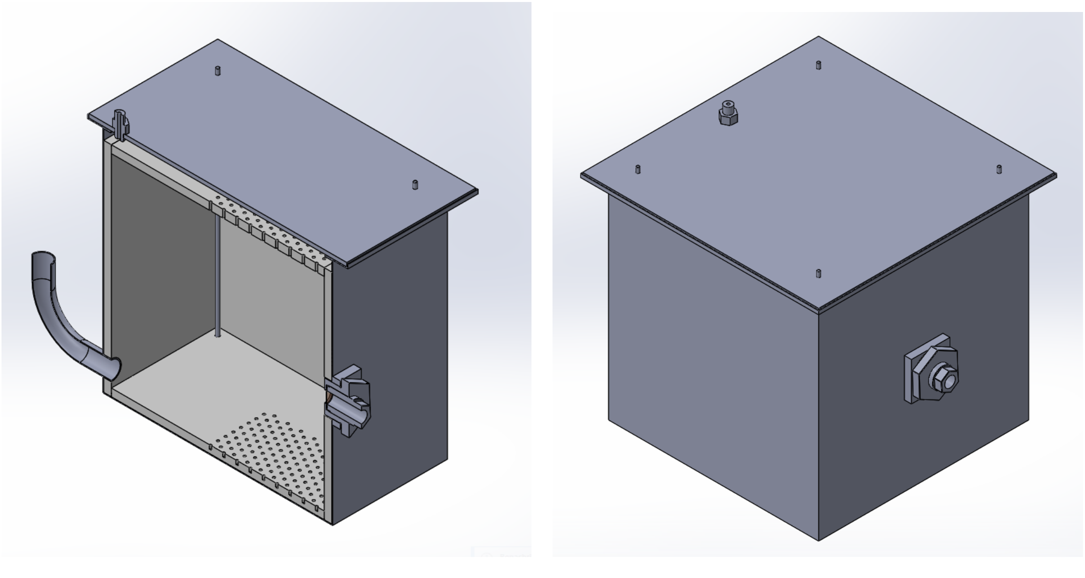

Figure 4.1.: Render of the detector vessel. **Left:** Cut of the vessel with the interior PTFE plates used for reflection visible (light grey). The beam window can be seen in the centre of the right wall. **Right:** Closed detector.

A render of the detector design is shown in figure 4.1. The stainless steel vessel holds a 22 litre volume, to be filled with opaque liquid scintillator. The area facing the centre of the beam side is filled with a triangular grid of 255 Bubo-WLS fibres (see sec. 3.5.2) with 10 mm spacing. This extra volume provides the possibility to change the fibre spacing to 15 mm and still have enough space for all fibres.

At the inner sides of the detector vessel 10 mm thick PTFE plates are placed to act as reflectors for the light produced by the scintillator (see fig. 4.2). In theory this allows for a better energy resolution of events near the walls since less photons would be lost due to absorption. The top and bottom plates are connected by four threaded rods. This allows the middle assembly consisting of those plates, and all 255 Bubo-fibres to be constructed outside of the vessel (see ch. 4.2) and to be inserted into the detector.

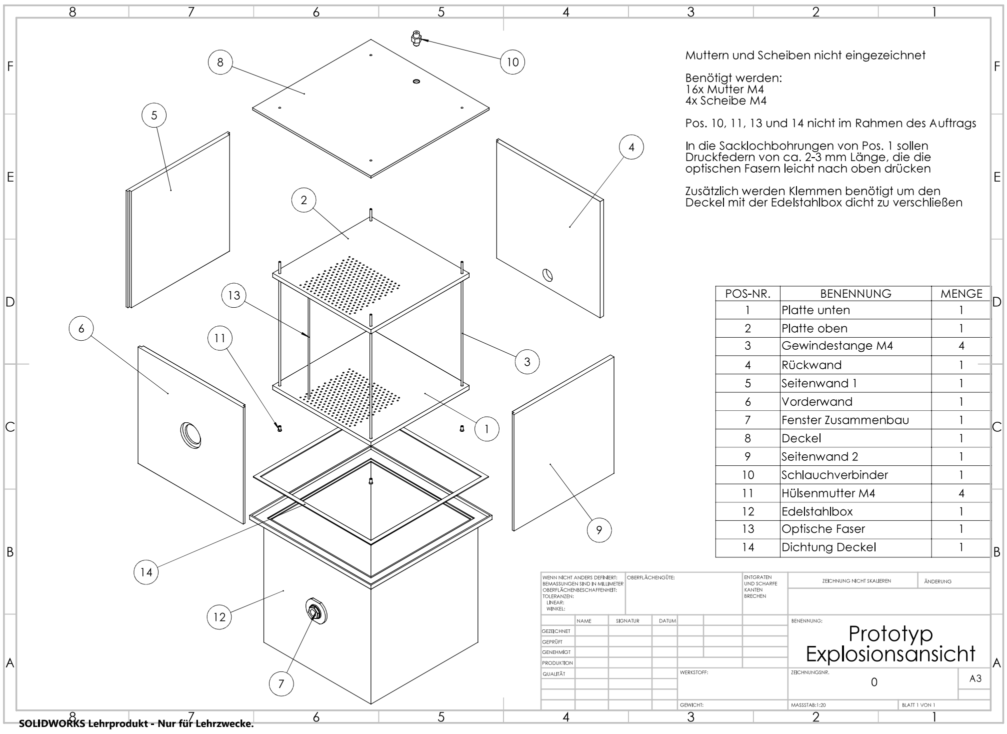

Muttern und Scheiben nicht eingezeichnet

Benötigt werden:
16x Mutter M4
4x Scheibe M4

Pos. 10, 11, 13 und 14 nicht im Rahmen des Auftrags

In die Sacklochbohrungen von Pos. 1 sollen Druckfedern von ca. 2-3 mm Länge, die die optischen Fasern leicht nach oben drücken

Zusätzlich werden Klemmen benötigt um den Deckel mit der Edelstahlbox dicht zu verschließen

POS-NR.	BENENNUNG	MENGE
1	Platte unten	1
2	Platte oben	1
3	Gewindestange M4	4
4	Rückwand	1
5	Seitenwand 1	1
6	Vorderwand	1
7	Fenster Zusammenbau	1
8	Deckel	1
9	Seitenwand 2	1
10	Schlauchverbinder	1
11	Hülsenmutter M4	4
12	Edelstahlbox	1
13	Optische Faser	1
14	Dichtung Deckel	1

BENENNUNG: Prototyp Explosionsansicht
ZEICHNUNGSNR. 0
A3
MASSSTAB:1:20
BLATT 1 VON 1

Figure 4.2.: Exploded-view of the construction drawing for the prototype detector. The complete construction drawing can be found in the appendix A.1.1.

The lid of the detector (fig. 4.2, part 8) was not used for the tests at MAMI. Originally this lid was supposed to seal the detector volume and nitrogen would be constantly flushed into the detector as a protective atmosphere to hinder possible degradation of the scintillator due to atmospheric oxygen. However, contrary to the initial concept an alternative scintillator mixture was used, which does not significantly degrade when exposed to oxygen over the timespan of the experiments. Figure 4.3 shows a detailed drawing of the beam window. It is situated in the centre of the front wall of the vessel and a thin Kapton foil is used to minimally impact electrons passing into the detector. The foil is held in place by a screw-in inner part. The complete beam window flange possesses a significant thickness of steel, the impact of this on electron tracks will be discussed in sec. 6.3.2.

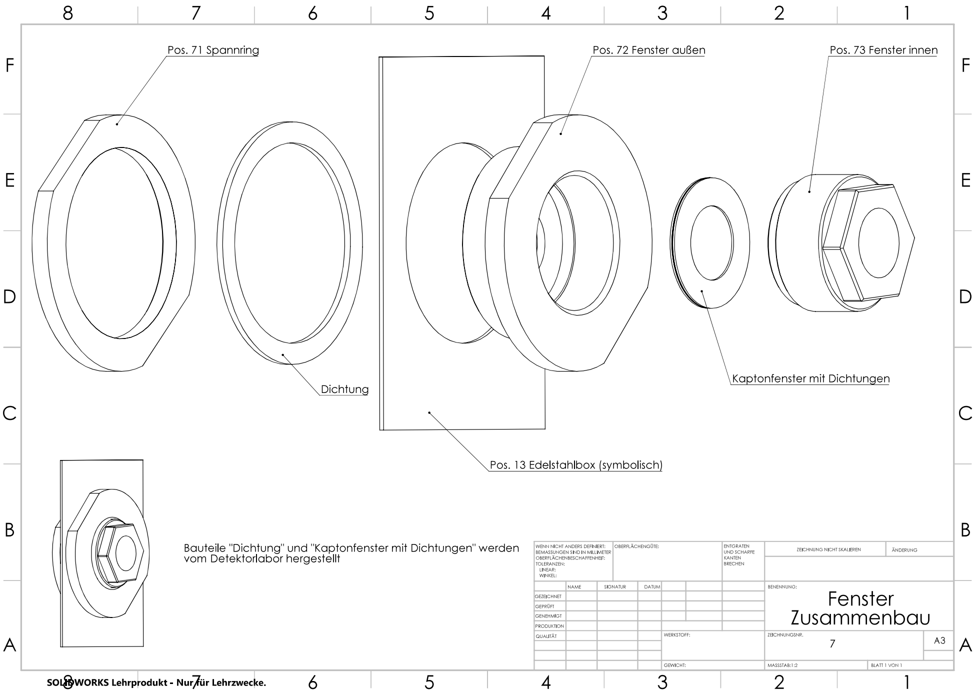

Figure 4.3.: Construction plan for the beam window flange.

4.1.1. Bubo-Fibres

The Bubo fibres used in the prototype detector consist of 3 mm diameter OWL fibres and 6 mm diameter quartz tubes with a wall thickness of 1 mm. The design of the top and bottom parts of the fibre assembly is shown in figure 4.4. The parts are 3D printed using a resin resistant to the scintillator (see appendix A.1.2).

The inner fibre is spring loaded in order to be pressed against the SiPMs on the PCB (see sec. 4.1.2). This, in combination with a small amount of optical grease, ensures a good optical coupling of the upper fibre end to the SiPM, while also allowing for some tolerances in the length of the fibre core, as well as the quartz tubes.

Between the lower end of the fibre and the spring, a "thorn" containing a small piece of reflective foil is situated. No optical grease is used to couple the lower end with

the reflector, as this would pose a risk of contaminating the inside of the quartz tube if the lower fibre end separates from the thorn during assembly.
The thorn is inserted into the spring to ensure its correct orientation during assembly and the spring fits into a blind hole of the main piece used to seal the lower end of the Bubo fibre.
The main piece holds the quartz tube in place and possesses a peg on the lower end, which is used in conjunction with blind holes in the lower PTFE plate in order to arrange all 255 Bubo fibres in the triangular grid.

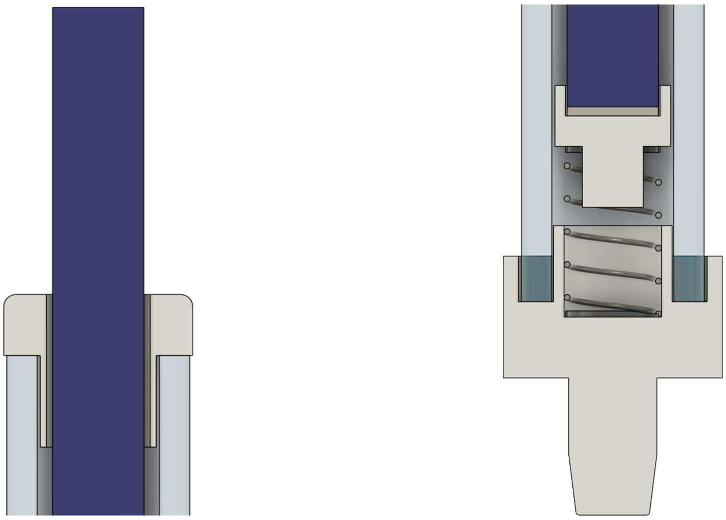

Figure 4.4.: **Left:** Side cut of the upper part of the Bubo assembly. The OWL fibre is not connected to the 3D printed part. **Right:** Side cut of the lower part of the Bubo assembly.

To attach the main parts of the upper and lower Bubo ends, the same 3D printing resin is used as a UV activated glue. First, the lower part is glued to the quartz tubes by placing a few drops of resin inside the outer rim (see fig. 4.4, right), then pressing the tube into it. This spreads the resin inside the rim, creating a seal and forcing some of the resin to rise about 1 mm inside the tube. This creates a stronger bond between both parts (see fig. 4.5, right). To cure the resin an ordinary 3D printing resin curing station is used.
After fixing the lower piece, the spring and thorn containing the reflector have to be placed inside the tube. The top part is fixed in a similar manner to the bottom by using resin. Since its opening is smaller than both the thorn and the spring, it has to be fixed last.

The OWL fibres are not yet placed into the tubes. This is one of the last steps when assembling the complete prototype. After placing the middle assembly, consisting of the upper and lower PTFE plates with all fibres placed and connected via the threaded rods on all four sides, in the detector vessel (fig. 4.2), and filling the detector with the scintillator, the OWLs can just be inserted through the holes in the top PTFE plate and the upper part of the Bubo tubes (see sec. 4.2 and sec. 4.3).

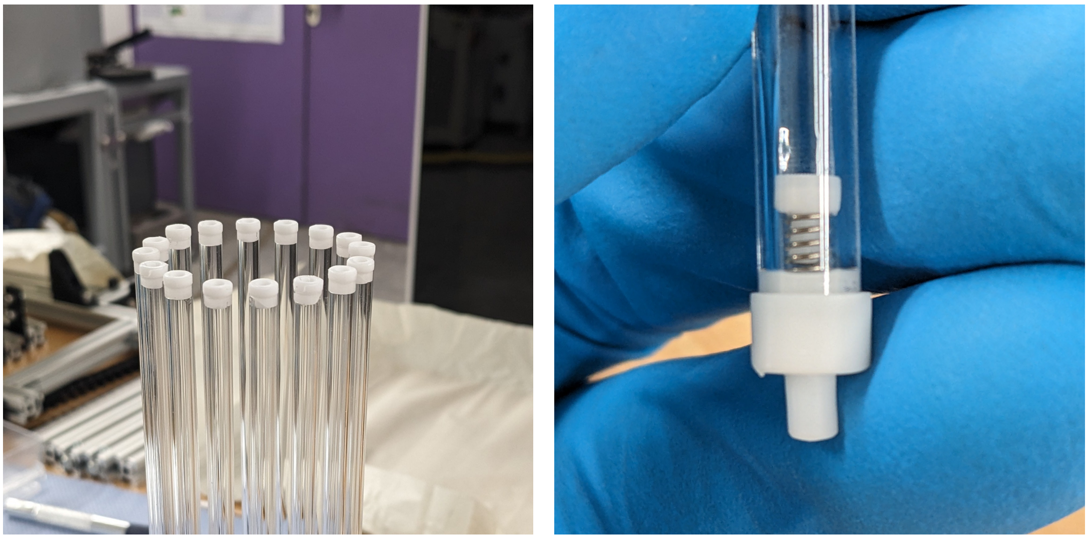

Figure 4.5.: **Left:** Bubo fibres after attaching to top parts. 3D printed stands are used to hold 16 fibres at once while assembly and curing of the resin. **Right:** Lower part of a finished Bubo fibre.

4.1.2. Electronics

The readout of the fibres is performed by SiPMs arranged in the same triangular grid as the fibres and placed directly on a PCB (see fig. 4.6). A CAEN FERS 5200 system is used to control and read out the SiPMs. Since 255 SiPMs are used in the detector, four separate DT5202 units connected to a DT5215 concentrator board are required (see A.2.2).

As the size of the PCB is limited to the dimensions of the inner assembly of the detector, it is not possible to connect the DT5202 directly and route the signals as intended to the PCB. In order to achieve this, a secondary PCB has to be used. This PCB is placed directly on top of the main PCB and is connected via several rows of 2.54 mm pin connectors.

The SiPM grid is divided into four sectors, one for each board. For reliability purposes in the potential use of the self-triggering mode of the detector, the first rows near facing the beam side were chosen to be routed to one common board (Board 0). The division of the grid for other boards is done in the most efficient manner when designing the routing. The division of the board and the SiPM to channel mapping can be seen in figure 4.6 (right).

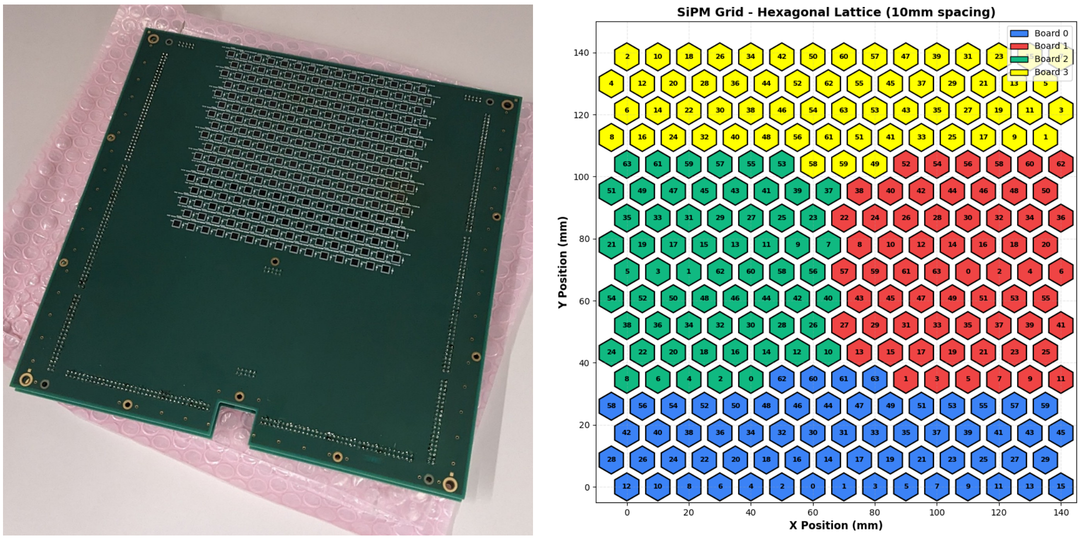

Figure 4.6.: **Left:** Finished main PCB with the SiPMs placed in the grid. **Right:** Division of the SiPM grid between all four FERS boards.

4.2. Detector construction

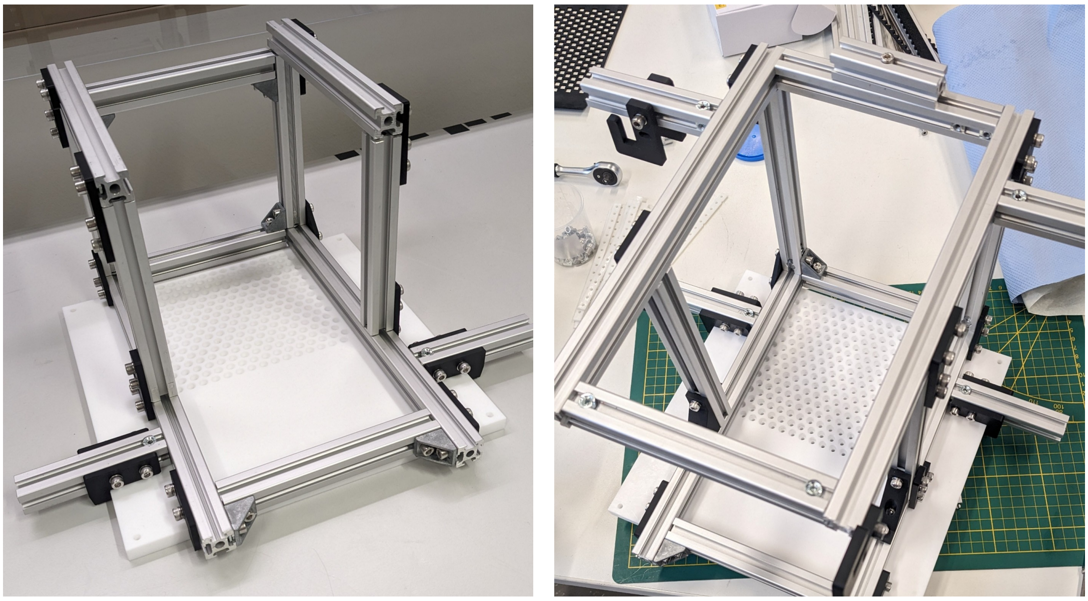

Figure 4.7.: Assembly frame for placement of the Bubo tubes. The **left** shows an early version, the **right** is an improved iteration with brackets to secure the top and bottom PTFE plates.

To arrange all 255 Bubo fibres in the triangular grid, a construction frame has to be used. This frame can be seen in figure 4.7 and 4.8. The frame is constructed using 20 mm aluminium extrusions and clamped to the upper PTFE plate using 3D printed brackets.

The Bubo tubes are then placed upside down into the plate. The placement has to be done row by row. An auxiliary clamp is used to hold and align the current row, before placing a bracket on top of the free standing tubes, securing the row once all 15 tubes of it have been placed. Then a small piece of tape is used to secure the current row to the frame. The top brackets have interlocking features to allow them to more securely hold the row in place in relation to the neighbouring rows. Once all 17 rows are in place, the bottom PTFE plate has to be placed on top of the frame and the pegs of the bottom Bubo parts (fig. 4.4, right) have to be placed inside the corresponding blind holes in it.

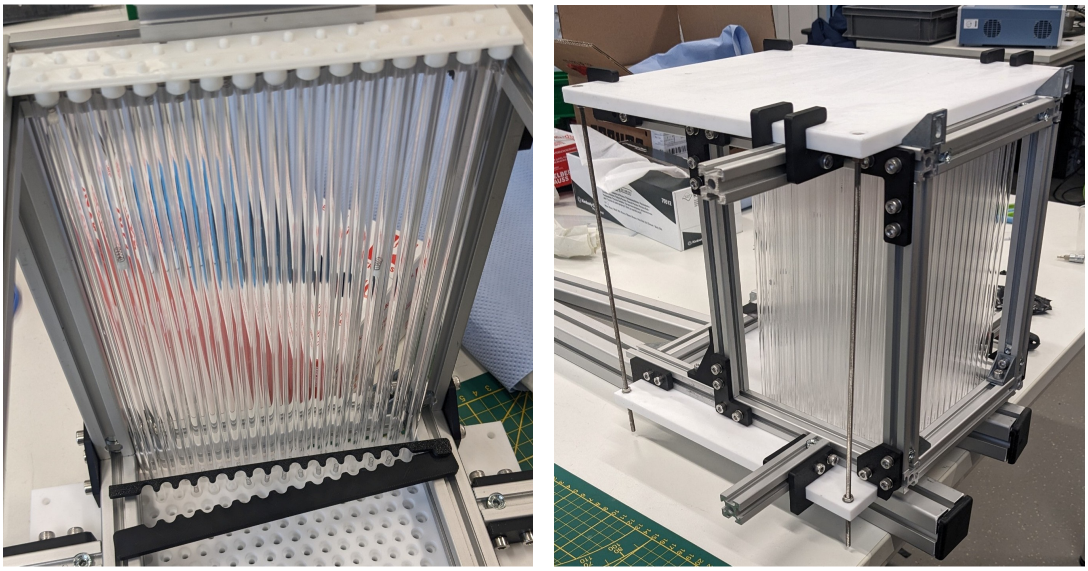

Figure 4.8.: **Left:** Assembly process of placing the Bubo tubes row by row with the auxiliary clamp visible. **Right:** Completed inner assembly that has yet to be rotated and is then transport-ready.

Originally, the tape should have been removed before placing the PTFE plate, but because the brackets are slightly warped, which is a common occurrence with thin 3D printed resin parts, this was not possible without the Bubo tubes disconnecting. The decision was made to trim excess tape before placing the PTFE plate. Due to the scintillator acting as a mild solvent this will have a negative effect on its purity, but the high viscosity of the scintillator mixture should limit the diffusion of the dissolved adhesive into the larger volume. Further considering the planned short operating life of the detector, the impact should be negligible.

After placing the bottom PTFE plate onto the frame, it is secured using brackets like for the top plate and four threaded rods are used to directly connect both plates. Finally, the whole inner assembly has to be flipped by 180 degrees around the horizontal axis. The frame remains attached to the assembly until just before the middle assembly is placed into the detector vessel at the test site at MAMI. This is done for a secure transport of the assembly. At the test site the frame is then carefully removed and exposed threaded rods at its top can be used to attach handles to slowly lower the assembly into the vessel.

The detector can then be filled with the scintillator through a gap in the back of the vessel (sec. 4.3). The scintillator acts as a dampener due to its high viscosity, and protects the Bubo tubes from shock while placing the detector into the test stand (fig. 4.9, left).
After placing the detector into the test stand, the OWL fibres can be placed. The fibres can be inserted through the holes in the top PTFE plate and are supposed to just drop into the Bubo tube.

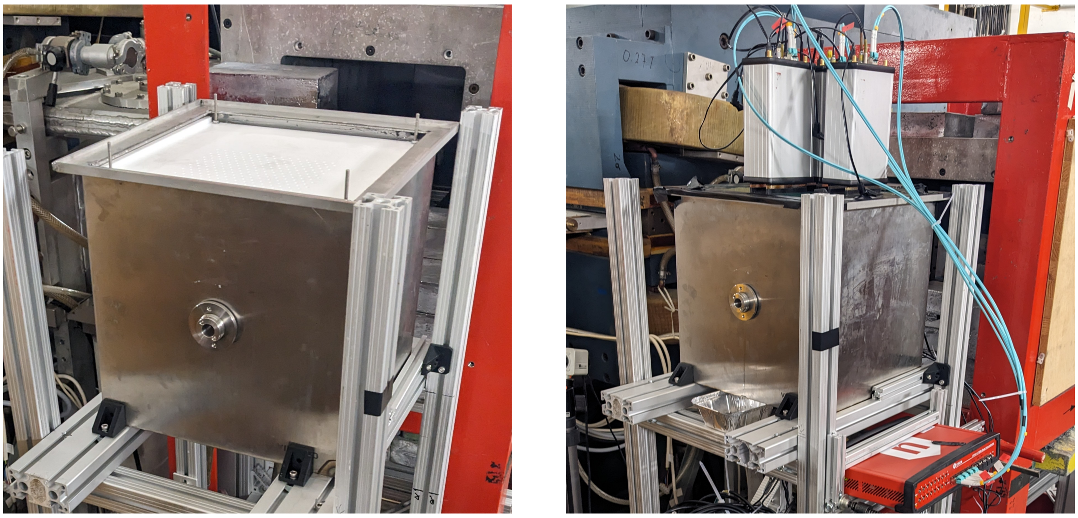

Figure 4.9.: **Left:** Detector vessel with inserted inner assembly placed onto the test-stand at the MAMI test site. **Right:** Finished prototype detector with the FERS installed.

Most fibres could easily be inserted and the springs worked as intended to provide a small upwards force. However, some of the fibres showed significant variation in the thickness of their quartz rod cores, which caused them to get stuck in the upper ends of the Bubo rods and either broke off inside the tubes or could just not be inserted (see sec. 4.3).

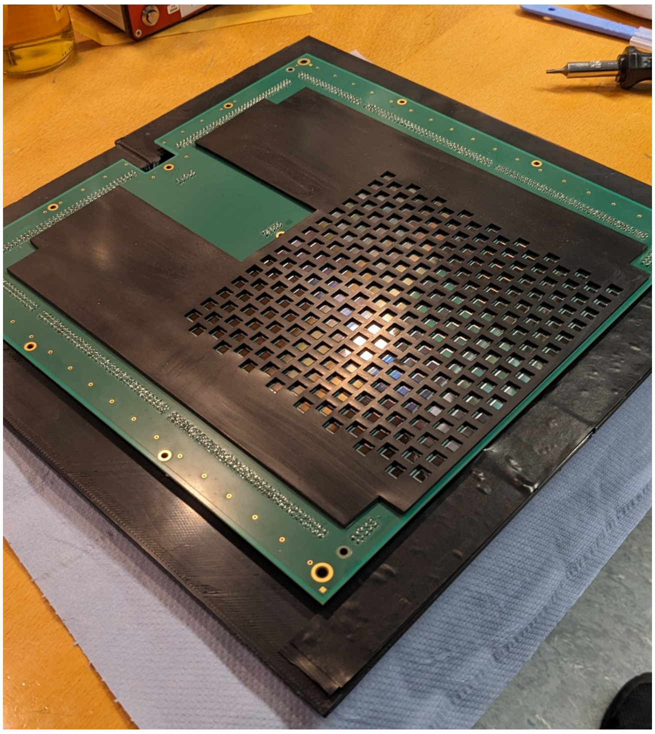

Figure 4.10.: Readout PCB with the rubber spacing mask attached.

In order to place the PCBs and the SiPMs, a 2 mm thick rubber mask was laser cut with cutouts corresponding to the SiPM grid. This mask is then attached to the PCB, using a double sided adhesive tape and ensures that the PCB does not rest on the SiPMs directly, which would damage them. Additionally, the mask physically isolates the SiPMs, preventing light transmission between fibres and other SiPMs. Guidance pins are then inserted into four blind holes in the top PTFE plate. When placing the PCBs, these ensure the correct orientation of the SiPM and fibre grid.
When the PCBs are in place, light proof tape is used to seal the detector, and the readout electronics are connected. To further ensure that no environmental light gets into the detector, a large light-thight blanket is placed around the electronics.

4.3. Problems and future improvements

When constructing the detector, several problems arose. Most importantly it became clear that the design of the Bubo top part has to be revised. In the current design, a thin straw-like part is present at the lower half of the part (see fig. 4.4, left). This is intended to give the resin that is used in bonding the part to the quartz tube more surface area and to centre the part. However, because of physical limitations of the 3D-printing, a certain thickness of this feature has to be used and the diameter of the hole for the OWL core is getting restricted. In most cases this does not matter, since the diameter of the quartz OWL cores should be 3 mm and the hole has a diameter of 3.3-3.4 mm. But the manufacturing tolerances of the rods were lower then expected, causing several rods to be significantly larger. Due to this, many rods scraped against this inner hole of the Bubo top, damaging the paint layer on the outside, and several fibres could not be inserted. This can be seen in figure 4.11. In future Bubo production, this can be avoided by not using the straw-like part of the top cap and instead using a design shown in figure 4.12. There, a thicker cap is used with counterbore hole, where one diameter matches the inner diameter of the quartz tube, the other a slightly larger diameter as the outer diameter of the tube. The bond would then be achieved by placing a small amount of resin at the inner rim and spreading it by inserting and rotating the tube.

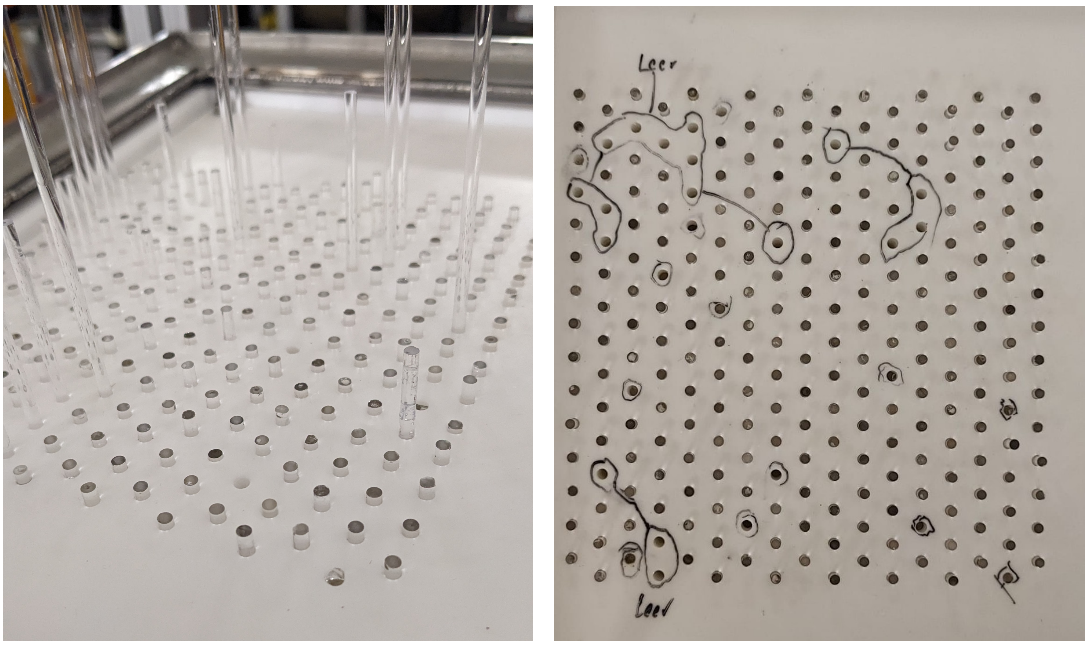

Figure 4.11.: **Left:** Stuck OWL fibres in the Bubo tubes. Some of the seen extruding fibres could be forcefully inserted, but others broke. **Right:** Fibre grid with the broken or missing ("leer") fibres marked.

As described in sec. 4.2, difficulties arose when arranging the Bubo tubes in the assembly frame. The brackets used had a problem staying in place before the PTFE plate could be placed. For this reason, extra adhesive tape was needed to secure them, which could not be fully removed after assembly. Therefore, for a potential second prototype, the construction method has to be revised. This could be done by making the pegs at the bottom of the Bubo tubes longer, allowing the use of thicker brackets that connect the rows together. Additionally, the blind holes in the bottom plate should be changed to through holes. This would make it easier to align the plate and check whether all tubes are seated in the plate.

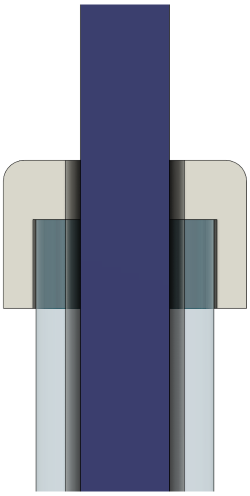

Figure 4.12.: Revised design of the Bubo top cap. This does not restrict the size of the through-hole.

4.4. Design and construction conclusions

As mentioned, this is the first ever opaque liquid scintillator detector built for electron tracking within the context of Dark Matter searches. During the construction of this prototype various insights have been gained on the production procedure of this kind of detector. As described in the previous section several problems arose in the production of the prototype and the Bubo fibres, which have already been identified, and the first potential improvements have been devised. This will allow for more efficient and precise manufacturing in the future.

5. Simulation studies

5.1. Simulation framework

In order to determine the desired dimensions and spacing of the prototype, a Geant4 simulation framework of the planned NuDoubt^{++} detector was modified to simulate the expected performance of the prototype. Geant4 is a Monte Carlo simulation toolkit for the propagation of particles through matter developed by CERN [28].

5.1.1. Initial NuDoubt^{++} simulation

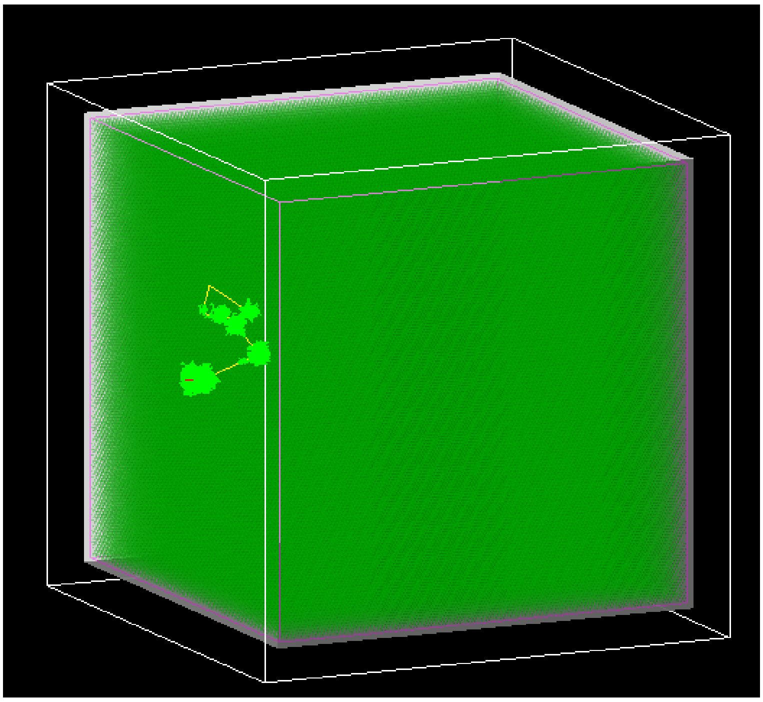

Figure 5.1.: Event example of a 14 MeV electron interacting with the detector, which created multiple clusters caused by γ-emission and subsequent Compton scattering.

The initial NuDoubt^{++} simulation contains the detector seen in figure 3.4. This is a cylindrical volume of opaque scintillator of 1.4 m diameter, filled with a triangular fibre grid of 10 mm spacing. To get a better idea of the event signature and possible event topology caused by 14 MeV electrons within the detector, the geometry of the

NuDoubt^{++} simulation was changed from cylindrical to cubic and an electron gun was placed in the middle of one detector side. In this configuration, electrons with 14 MeV kinetic energy were generated and directed towards the detector centre (see fig. 5.1).

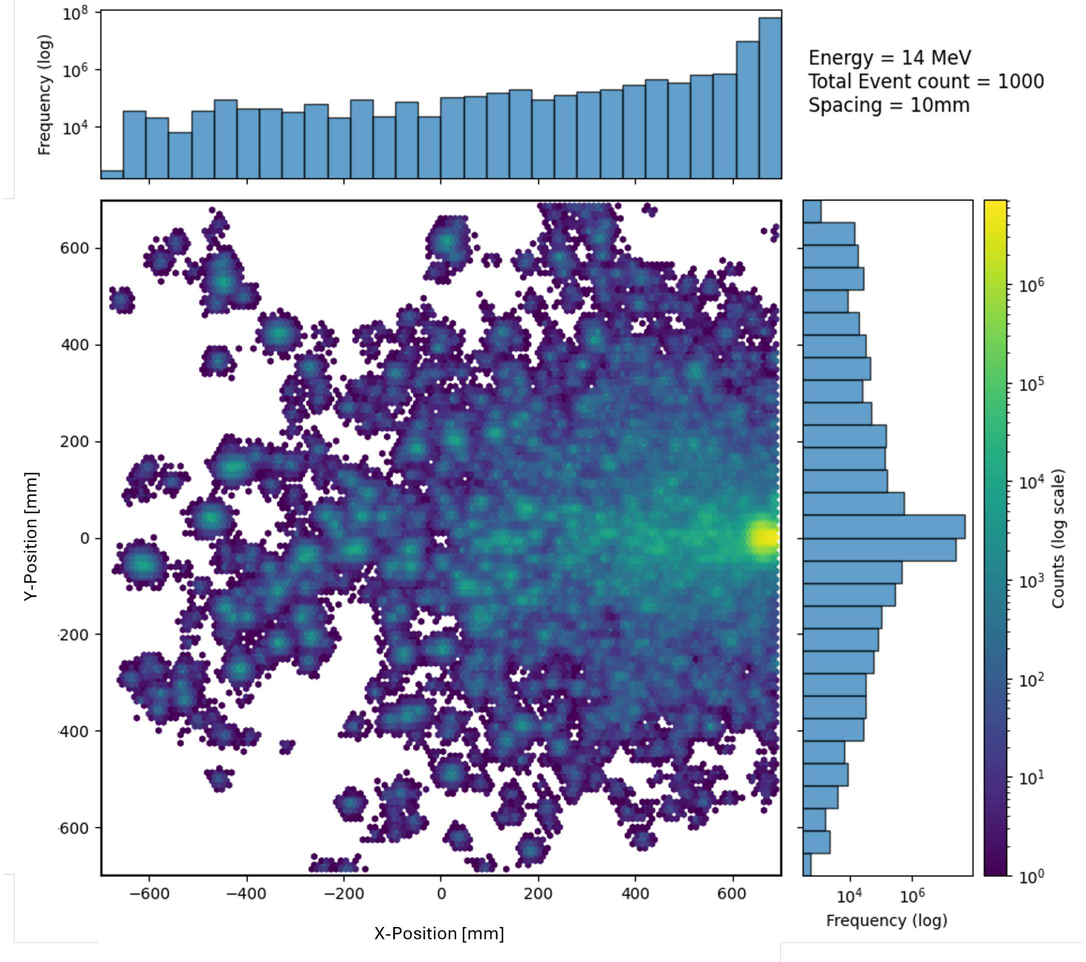

Figure 5.2.: 1000 electron events superimposed to visualize their potential sizes.

Figure 5.2 shows the signals of 1000 events displayed at once. When an electron is generated, it can produce light directly or, due to bremsstrahlung, a photon can be created. These photons can travel relatively large distances inside the detector before Compton scattering on electrons in the detector, which then again produce scintillation light. This creates the clusters that can be seen in figures 5.1 and 5.2.

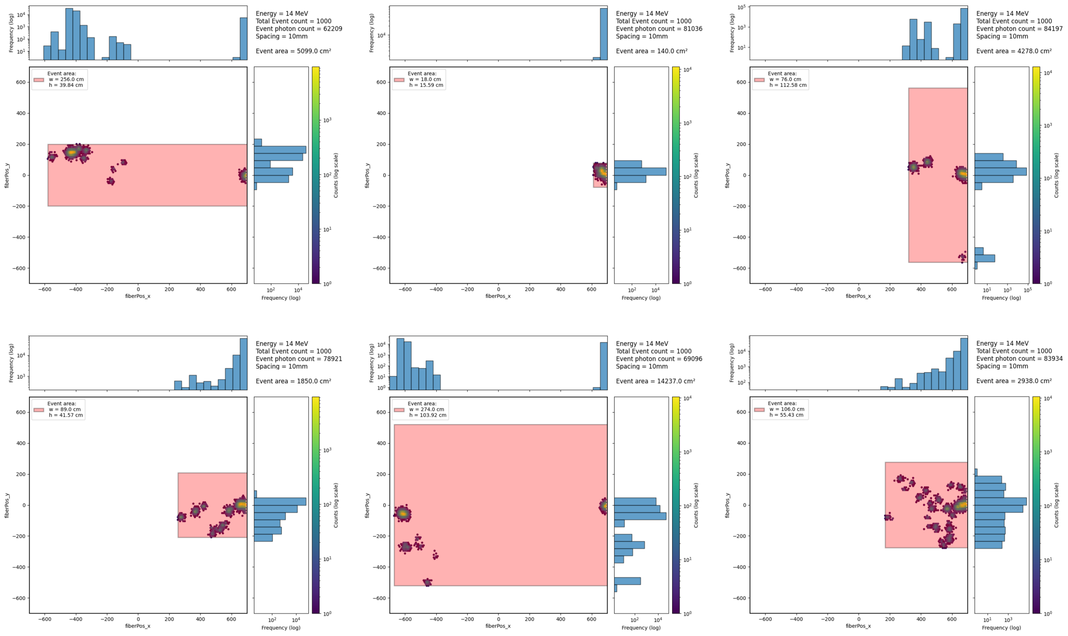

Figure 5.3.: Size envelopes of multiple 14 MeV electron events. The envelopes are symmetric.

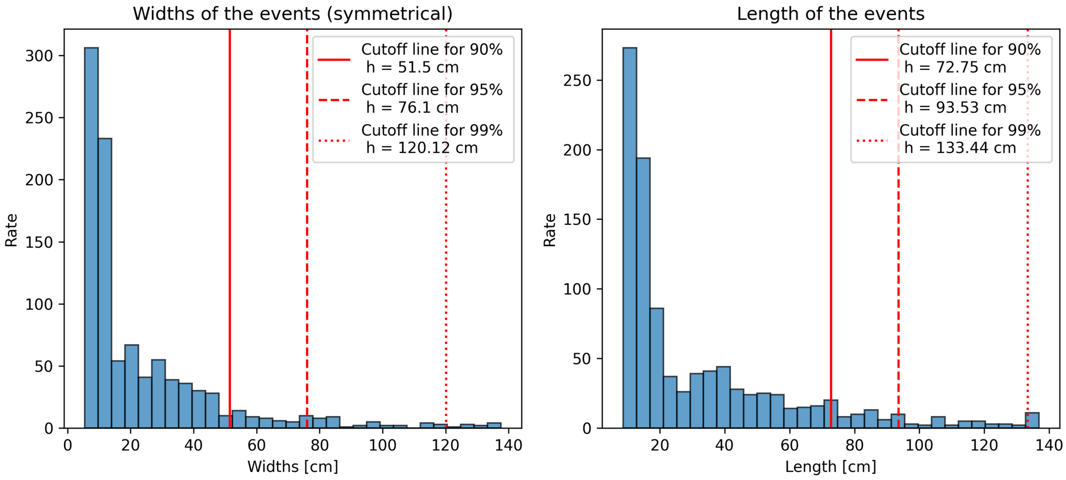

Figure 5.4.: Distribution of the dimensions for electron events

Figure 5.4 shows the distribution of event sizes that were determined by drawing envelopes around the events, as seen in figure 5.3. A detector capable of containing 90% of the simulated 1000 events would need to be just over 100 cm wide and over 70 cm long and be already half the size of the planned final NuDoubt^{++} detector.

Since this would exceed the scope of this master's thesis, it was decided to primarily focus on the initial electron track. As seen from the peaks in the distribution, a volume of about 20 cm to 30 cm width and about 20 cm length will be sufficient to contain the events reliably.

5.1.2. Prototype simulation

5.1.2.1. Fibre spacing

The fibres are arranged in a triangular lattice (see fig. 5.5), as this allows for the most dense packing of fibres. A denser fibre spacing would of course increase the detectors spatial resolution, but comes at the cost of less active scintillator material and an increase in the number of required readout channels, and therefore production cost. For this prototype 256 readout channels are available (sec. 4.1.2).

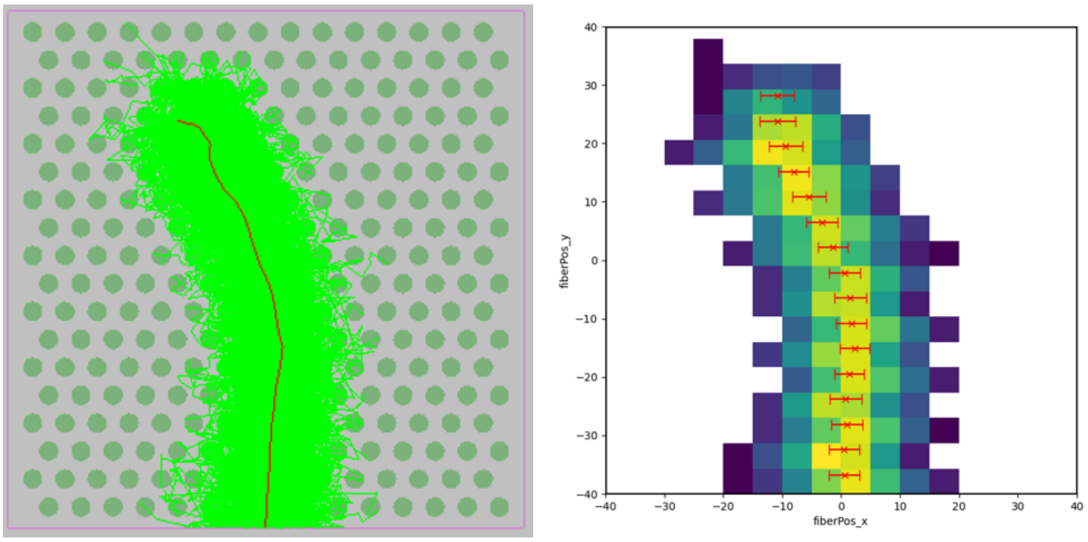

Figure 5.5.: A 14 MeV electron track with a 5 mm fibre spacing as seen in the simulation (**left**) and the visualisation heat map (**right**, axis in mm)

If a fibre spacing of 5 mm would be chosen as seen in figure 5.5, the detector could only cover a area of about 80 mm by 80 mm. The simulation however shows that the electrons can exceed this length, as shown in figure 5.6. Therefore, the 5 mm spacing was discarded.

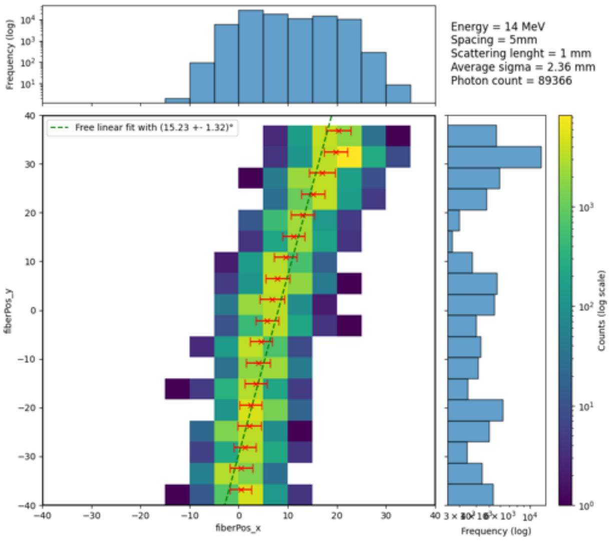

Figure 5.6.: 14 MeV electron passing through the available detector volume at 5 mm spacing and 255 fibres (heat map axis in mm).

A spacing of 10 mm or 15 mm can reliably cover the entire primary electron track with 10 mm having a better resolution. Therefore, the 10 mm spacing was chosen for the prototype, but the detector volume was designed to be sufficiently large to also fit a fibre grid of 15 mm for future testing.

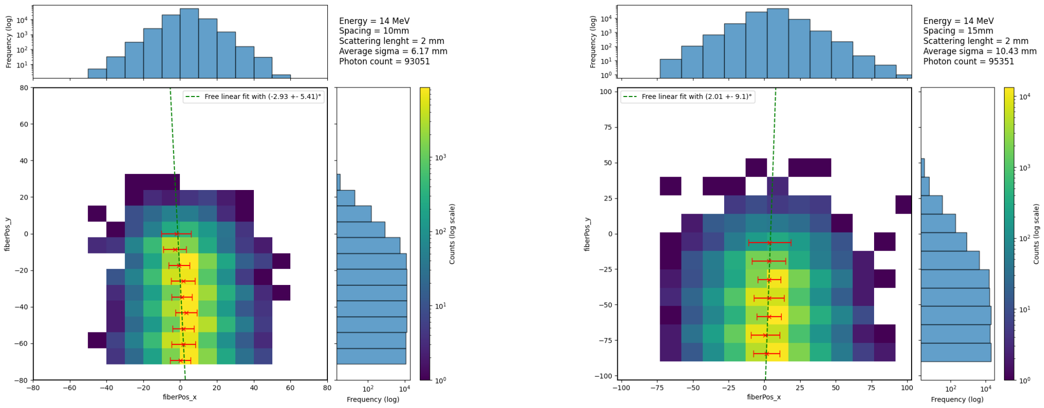

Figure 5.7.: 14 MeV electron tracks with 10 mm (**left**) and 15 mm (**right**) spacing (heat map axis in mm).

5.1.2.2. Prototype simulation setup

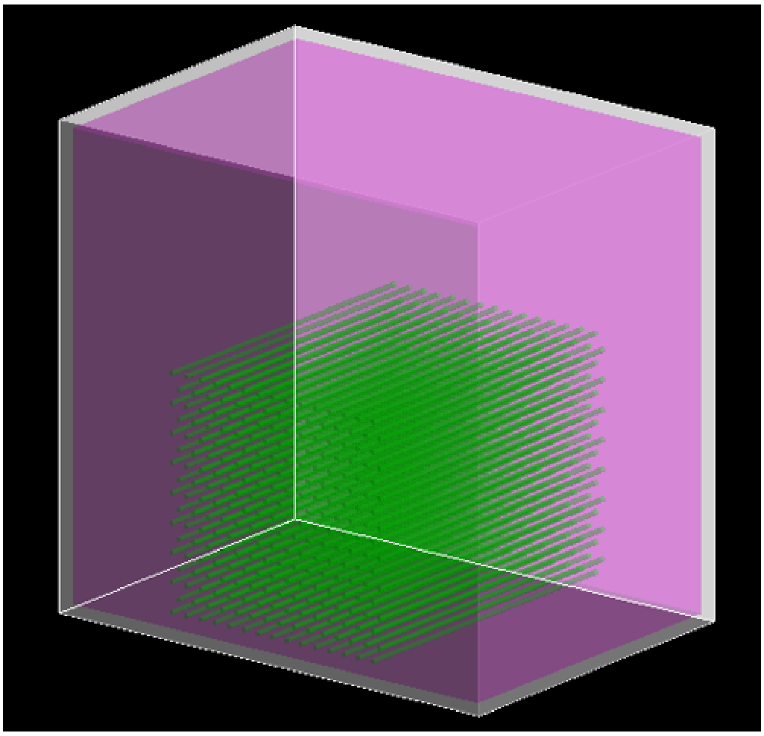

Figure 5.8.: Prototype detector simulation geometry

To investigate the main capabilities of the prototype, two final simulation setups were devised. Figure 5.8 shows the simulation matching the final dimensions of the constructed prototype detector (see sec. 4). A 15 by 17 triangular fibre grid at 10 mm spacing is placed on the lower side of the detector volume. This is surrounded on the sides and the back by the liquid scintillator. The total volume would allow the future testing of an alternative grid with 15 mm spacing with about the same number of fibres. Electrons were generated in the centre of the lower detector wall inside the volume travelling upwards into the fibre grid (see fig. 5.9).

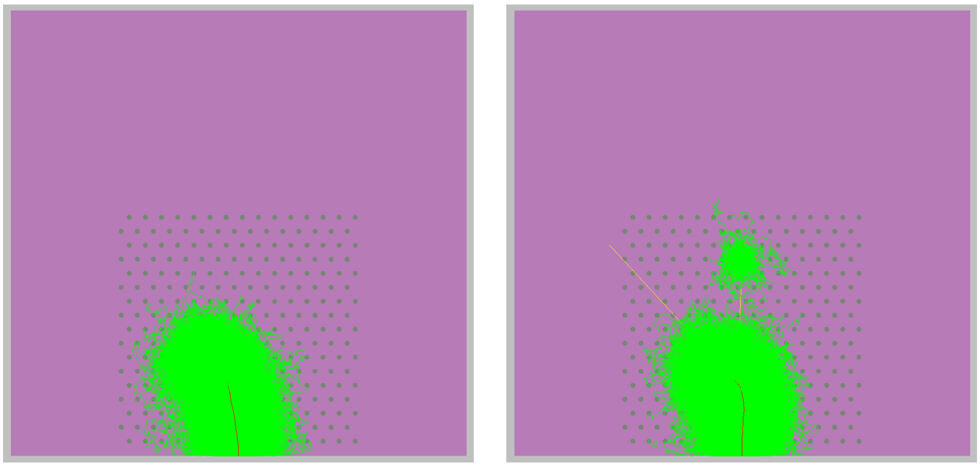

Figure 5.9.: Example events for the prototype simulation with 14 MeV electrons.

A secondary simulation setup was also developed to better match the expected events for Dark Matter interactions at DarkMESA (see fig. 5.10). Dark matter scattering events could take place anywhere in the detector volume and the detector would only see a sudden electron track starting inside it, in contrast to the beam electron tracks, which start at the beam window on the side of the detector. For this, the entire volume was filled with fibres and the electrons were generated in the centre of the volume with a random angle in the detector plane. The angle into or out of the detector plane was kept at 0°. This was done as no vertical position information can be reconstructed with the detector prototype, due to of the one-sided fibres readout.
The electron energies used in the simulations range from 7 MeV to 14 MeV in steps of 1 MeV.

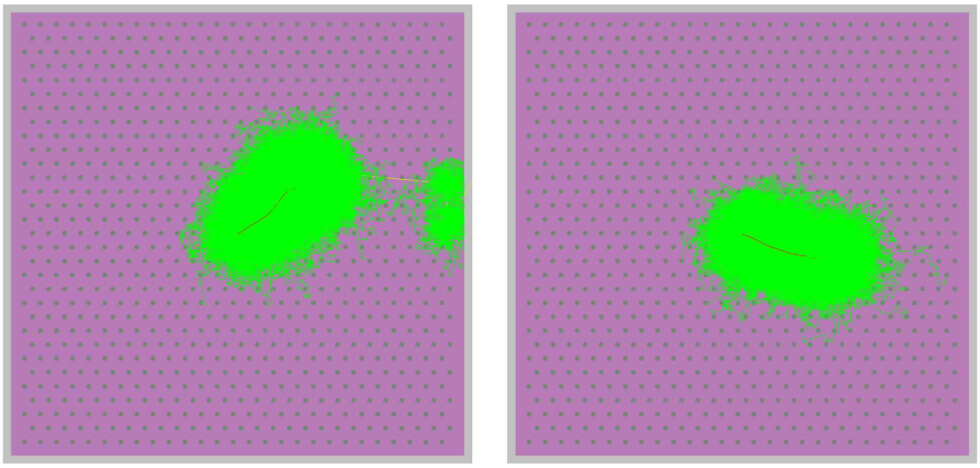

Figure 5.10.: DarkMESA-like simulation setup. Electrons are generated in the middle of the volume with 14 MeV.

5.1.3. Fibre efficiency and time spread

The Geant4 simulation does not model the OWL fibres, instead it only provides the hit times of photons on the fibre surfaces and positions. The processes in the fibres are not simulated, but calculated using a C^{++} program initially developed in another NuDoubt^{++} master's thesis [29], and adopted for the DarkMESA prototype simulation. The following equation is used to calculate the efficiency of the OWL fibres:

$$\epsilon = \epsilon_{\text{capture}} \cdot \epsilon_{\text{QE}} \cdot \epsilon_{\text{Coupling}} \cdot e^{-\frac{\text{Distance}}{\text{Att.length}}} \cdot (\epsilon_{\text{mirror}}) \tag{5.1}$$

For every shifted photon there is an equal chance to either be emitted travelling upwards towards the SiPM, or to be reflected downwards. The lower face of the fibres have a reflector coupled to the fibre. A 90% reflection efficiency is assumed for this reflector (ϵ_{mirror}), and also for the coupling of the upper fibre faces to the SiPM ($\epsilon_{\text{Coupling}}$). A capture efficiency of 40% [1] is assumed for the OWL fibres, which would be the projected best case scenario, as well as an attenuation length of 2 m. The quantum efficiency of the SiPMs is assumed to be 40%.

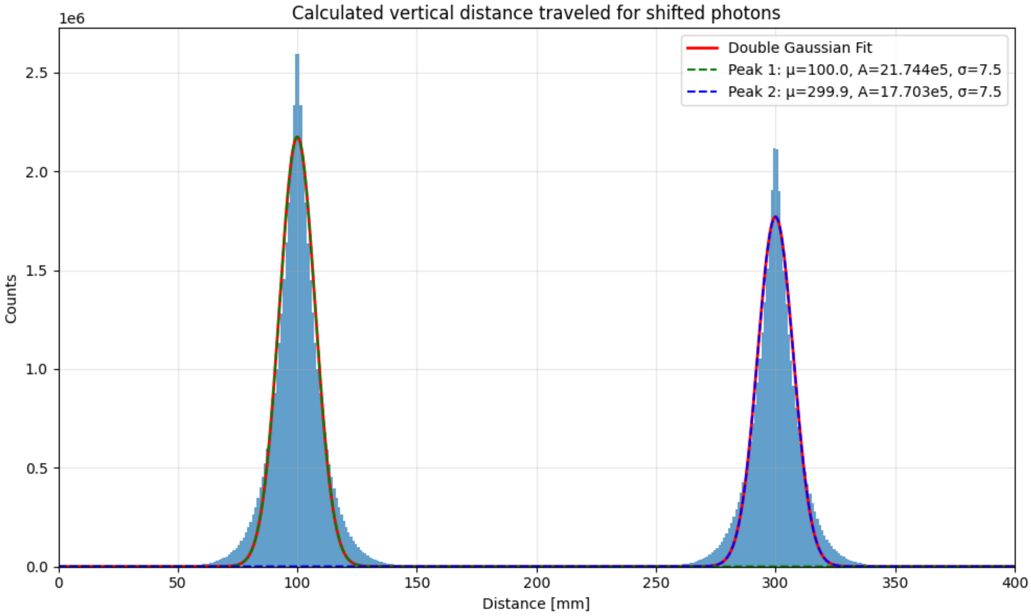

Figure 5.11.: Calculated distances travelled by photons inside the OWL fibres. Two peaks can be seen, since the fibre hits happen mostly in the middle of the detector and each shifted photon has a 50% chance of travelling up or down. Downward travelling photons have a 10% chance of being lost at the reflector and have to travel about 20 cm further. This caused the second peak to be about 18% smaller. The peaks are approximated with Gaussian fits.

As mentioned before, the simulation only provides the hit time of the fibre. Therefore the hit time on the SiPM has to be calculated by the same program. For this, equation 5.2 is used:

$$t_{\text{hit}} = t_{\text{capture}} + t_{\text{WLS-decay}} + t_{\text{timespread}} + t_{\text{transit}}. \tag{5.2}$$

After the scintillation photons hit the fibre and are captured (t_{capture}), the excited wavelength shifter has to decay first ($t_{\text{WLS-Decay}}$). Then the shifted photons have to travel to the SiPM. If they would travel on a direct path, this would only depend on the distance (t_{transit}), however in the OWLs the paths can be more complicated, e.g. spiralling up the fibre. This induces a variation in the travel time ($t_{\text{timespread}}$).
The distribution of the travelled distances is shown in figure 5.11 and the hit times on the SiPMs are shown in figure 5.12. Most photons arrive between a few nanoseconds and about 50 ns. Some can however take significantly longer. To avoid overlap photons from different events, a maximum event rate for a beam experiment would be in the order of a few MHz.

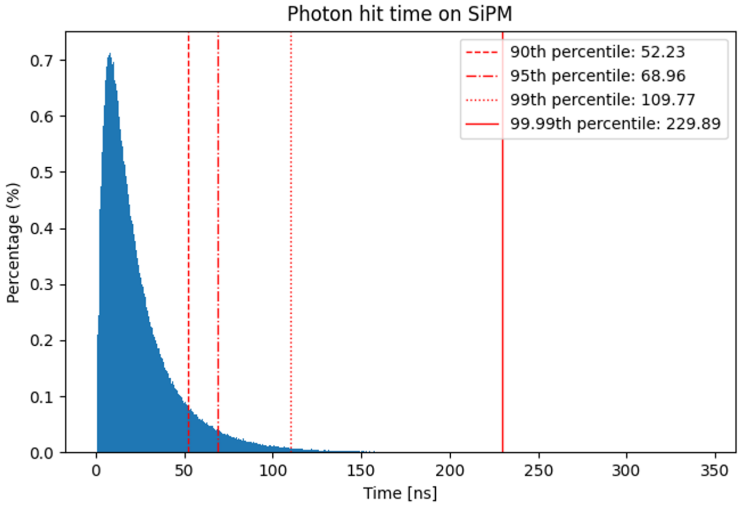

Figure 5.12.: Calculated photon hit times distribution of electron using the hit times provided by the simulation and equation 5.2.

5.2. Detector capabilities

5.2.1. Angular reconstruction

As mentioned in chapter 4, one of the main objectives of the prototype detector is to investigate the feasibility of angular reconstruction using an opaque liquid scintillator detector for electrons. This was done by a simple weighted linear fit to the tracks generated in the Geant4 simulation. A more sophisticated track reconstruction would certainly be possible and will be addressed in a future work.

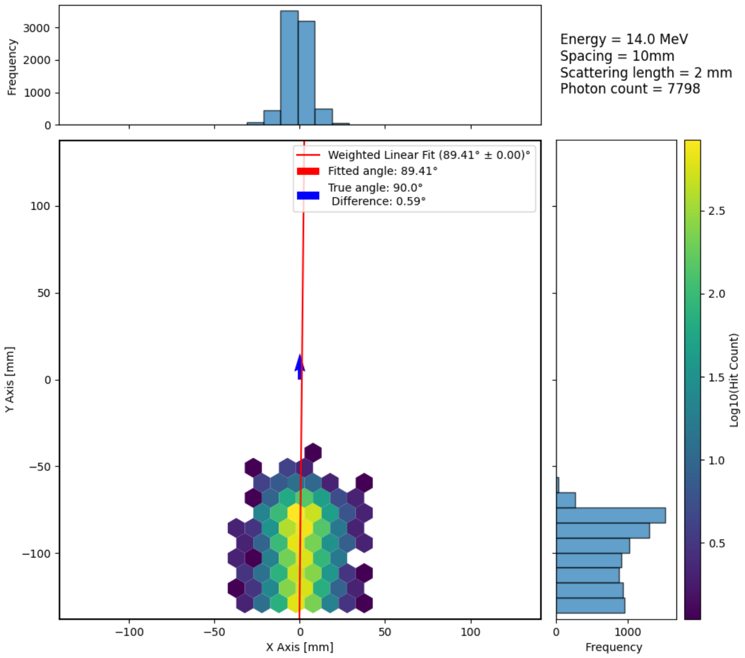

Figure 5.13.: Optimal fit case.

A optimal fit case can be seen in figure 5.13, where minimal scattering is present. The tracks in figure 5.14 show more scattering. The angular reconstruction still works reasonably, well but the need for a complex, non-linear fit is highlighted in the right track.

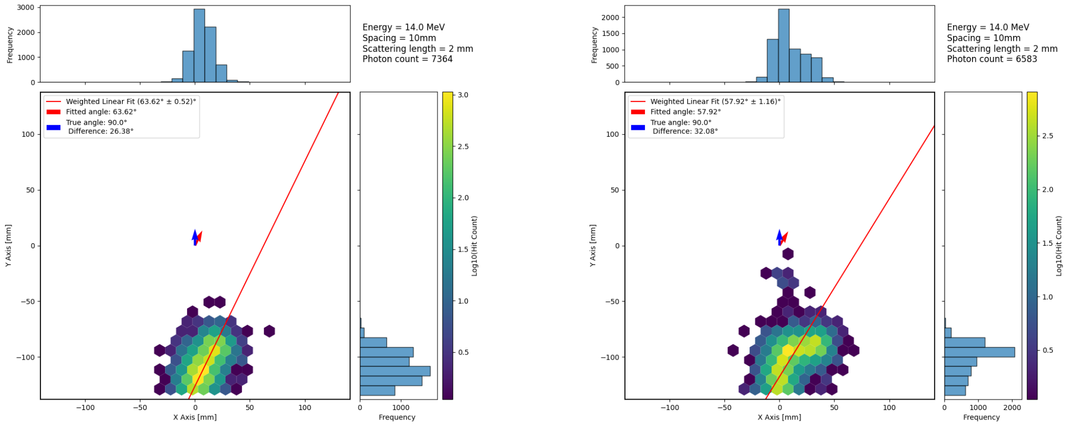

Figure 5.14.: Example fits. **Left:** A straight electron track at an angle due to scattering of the electron at the start of the track. **Right:** Track of an electron that initially travels straight into the detector, but then scatters abruptly. A more sophisticated fit method would allow for a better reconstruction of the initial electron angle.

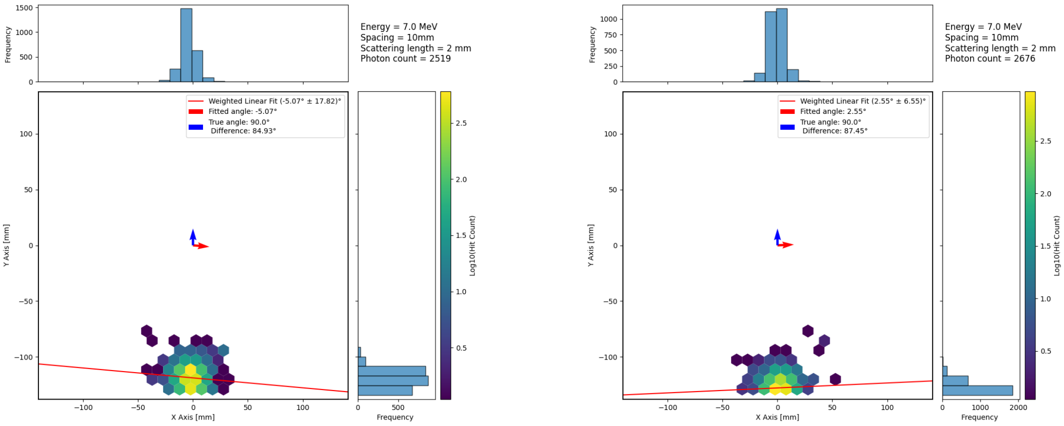

Figure 5.15.: Tracks of electrons that either lost a significant amount of energy due to bremsstrahlung or scattered into or out of the detector plane. Both shorten the track length and lead to a failure of the linear fit.

A problem of the prototype can be seen in figure 5.15. Low electron energies or large energy losses shortly after generation due to bremsstrahlung can cause the tracks to be too short for the linear fit to yield good results. The track can also appear to be shortened, caused by the electron being scattered into or out of the detector plane. For the DarkMESA-like simulation setup this is less of a problem, as the electron tracks are not cut at the beginning by the detector wall (see fig. 5.16).

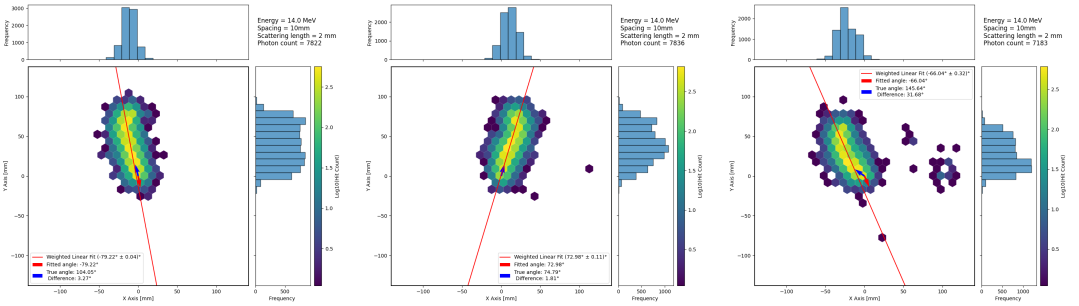

Figure 5.16.: Track fits for DarkMESA-like simulation setup

Figure 5.17 shows a difficult case for the angular reconstruction in the DarkMESA-like simulation and the intended future DarkMESA case. The electron scatters almost immediately after being generated, this causes the reconstructed fit to be off by about 90°.

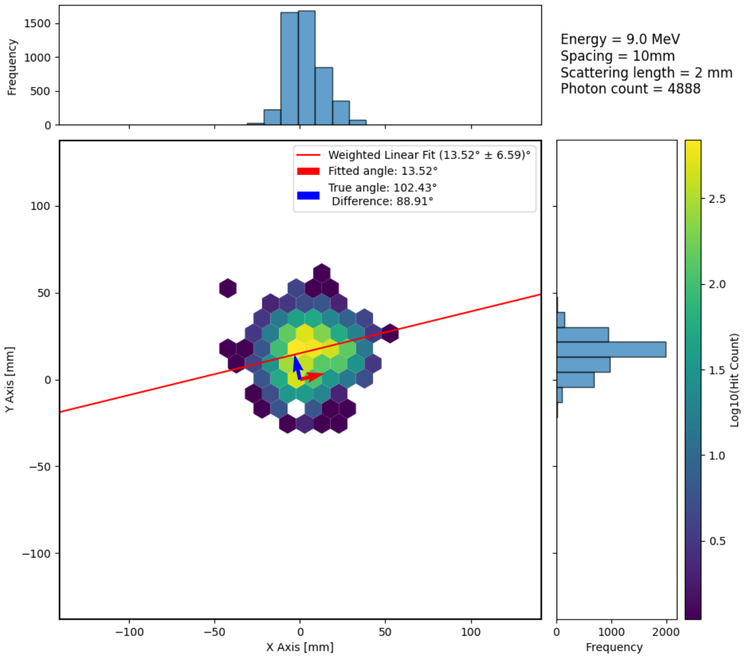

Figure 5.17.: In this event an electron is hard scattered almost immediately. This makes an accurate reconstruction using the linear fit unlikely.

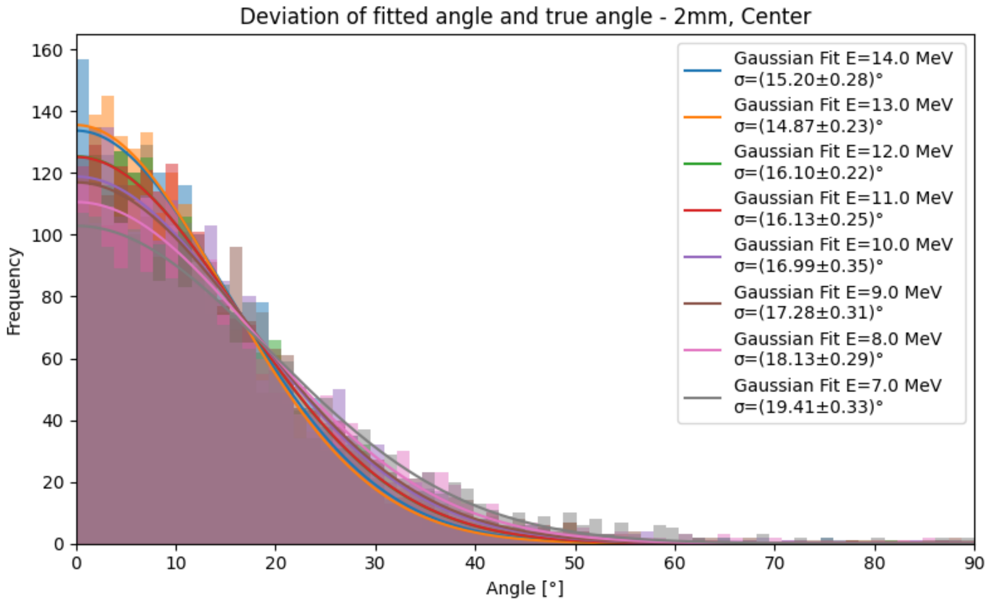

Figure 5.18.: Reconstructed angles for DarkMESA-like simulation.

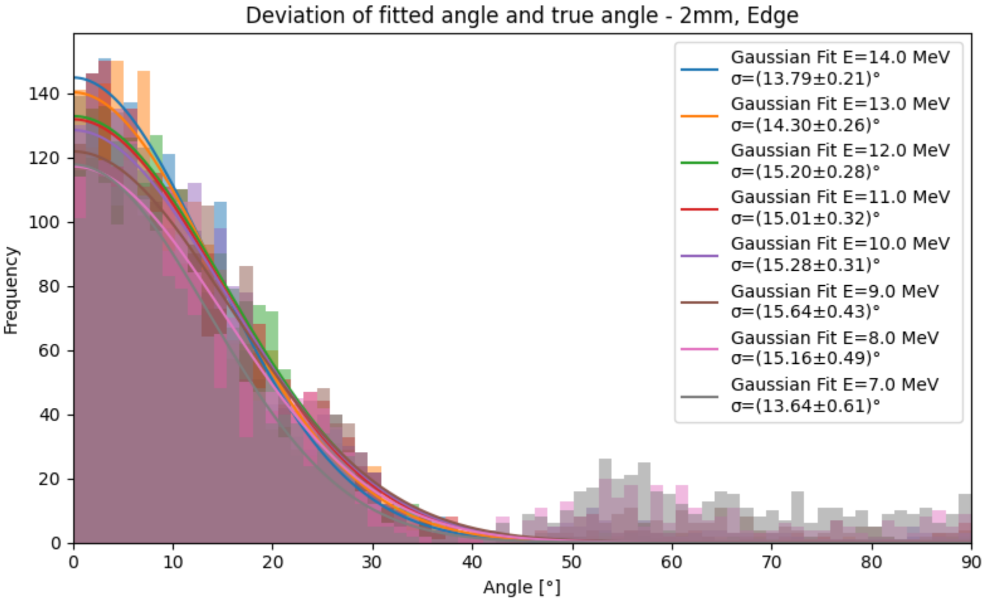

Figure 5.19.: Reconstructed angles for DarkMESA-like prototype simulation.

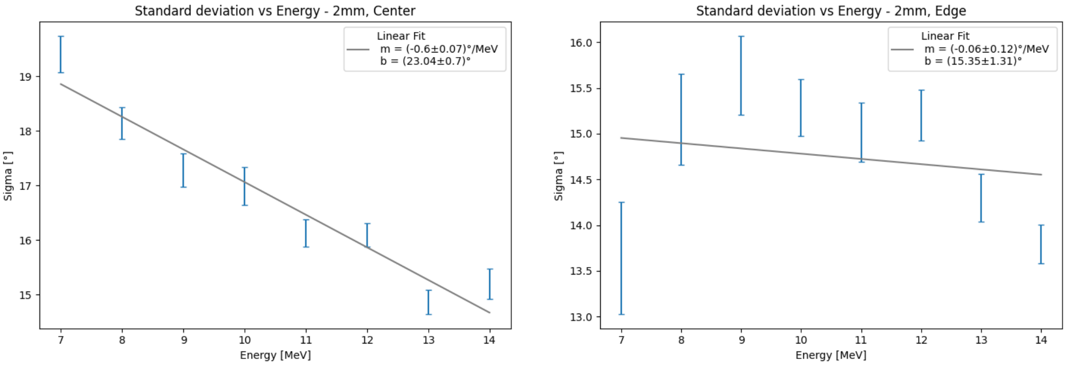

Figure 5.20.: Relation between electron energy for DarkMESA-like (**left**) and prototype (**right**) simulation.

When looking at the distribution of the fitted angles, a clear difference can be seen between the DarkMESA-like (fig. 5.18) and the prototype simulation (fig.5.19). Gaussian fits were performed for different energies and the relation between electron energy and reconstructed angle is shown in figure **??**. For the DarkMESA-like simulations, a linear relation between standard deviation and energy is shown. This is not the case for the prototype setup, and, when looking at the distribution, a bump is present at around 55°. Most likely this is caused by tracks that are too short for a reliable linear fit (see fig. 5.15).

5.2.2. Energy reconstruction

To investigate the energy resolution of the detector, a photon count to energy calibration has to be performed. For this, a Crystal Ball function [30] is fitted to the photon count distributions for different energies (7-14 MeV). The Crystal Ball function consists of a Gaussian core portion and a power-law tail. The power-law tail is used to take into account energy losses in a detector due to processes such as bremsstrahlung or escaping radiation (leakage).
This is also exactly what happens in the detector causing the tail seen in fig. 5.21 and fig. 5.22/5.23. The bremsstrahlung photons already mentioned in sec. 5.1.1 can cause energy leakage. For larger detectors this would be less of a problem.

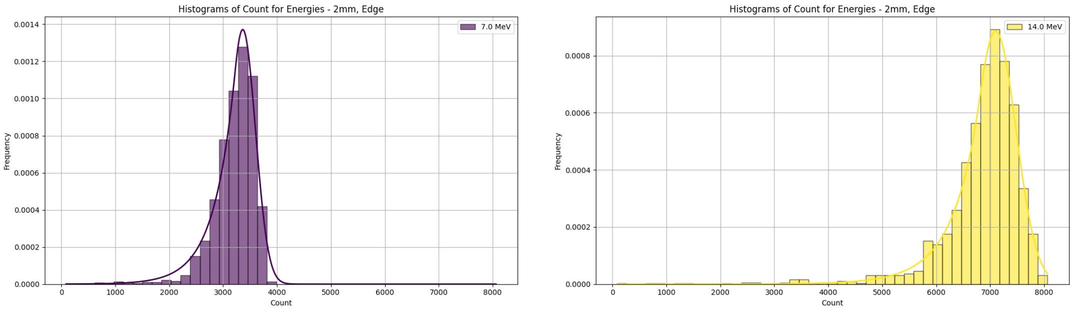

Figure 5.21.: Photon count distribution of 7 MeV and 14 MeV electrons with the superimposed Crystal Ball fit.

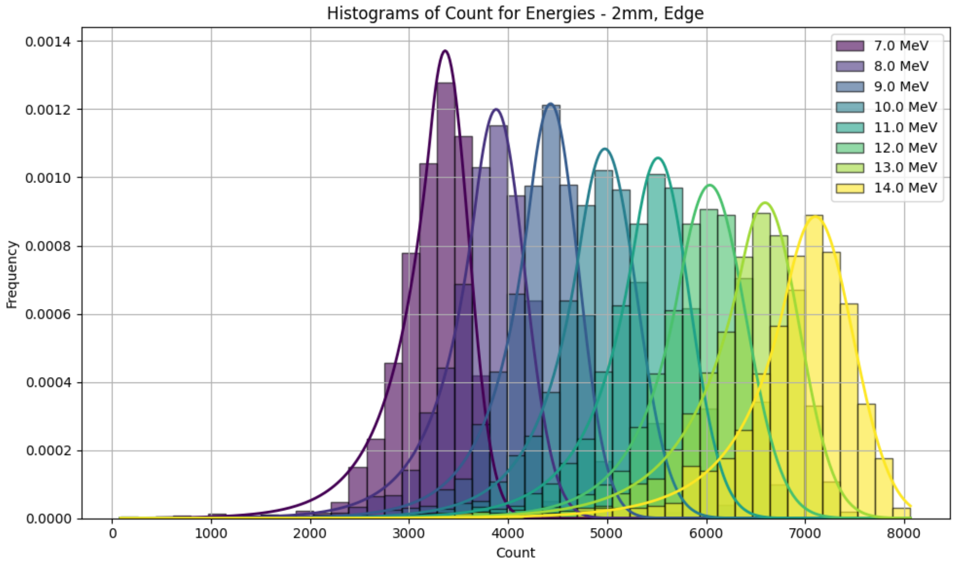

Figure 5.22.: Fitted photon count distributions of the prototype simulation.

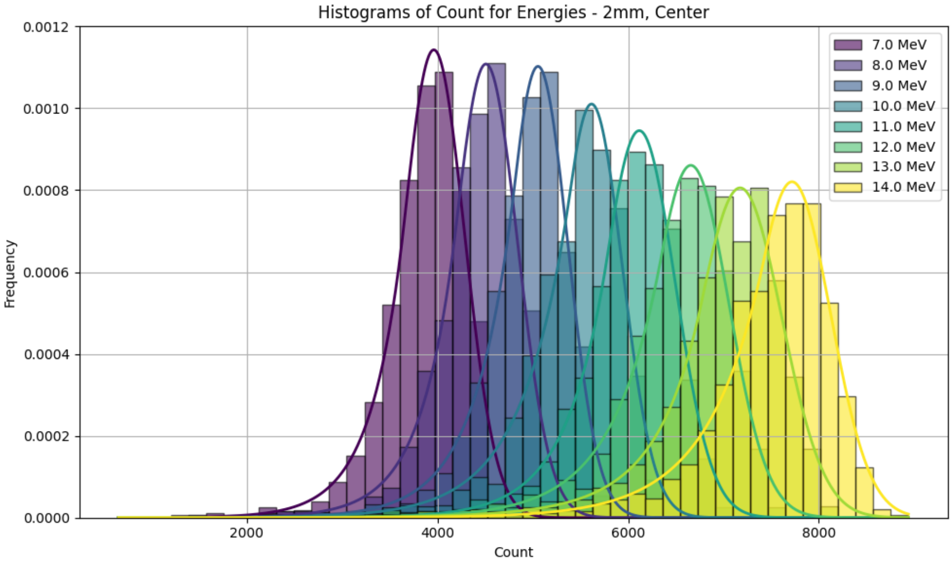

Figure 5.23.: Fitted photon count distributions of the DarkMESA-like simulation.

Using the fits of the distributions at different energies, a calibration is performed. Figure 5.24 shows that the relation between the peak or median of the fits to the initial electron energy is linear. By fitting this, a conversion function between hit count and energy was determined.

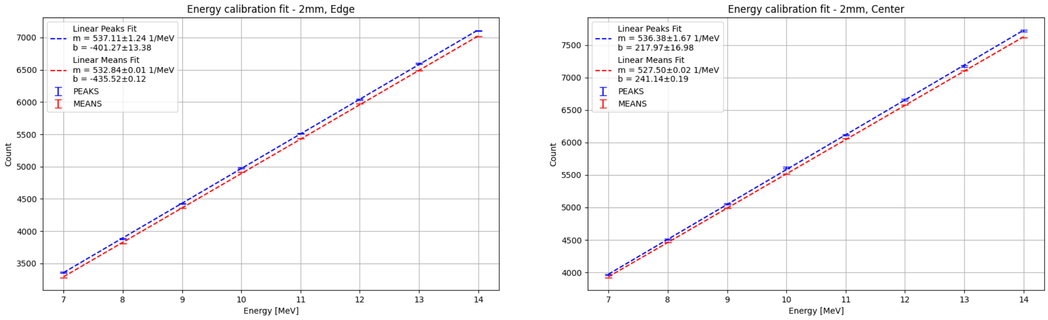

Figure 5.24.: Photon-count-energy calibration relation for both setups. For both setups two functions were determined, one using the peaks of the fitted functions and one using the medians.

To evaluate the quality of the calibration, the difference between reconstructed and true energy is calculated and shown for both setups in figure 5.25. The distribution again shows a Gaussian peak and a power-law tail caused by energy leakage.

The energy leakage due to photon escape is shown in figure 5.26. A clear correlation between the missing energies and the energies of photon leaving the detector volume of the simulation is seen. In the most extreme case about 12 MeV were missing in the reconstruction. This event shows a photon closely matching this energy leaving the detector.

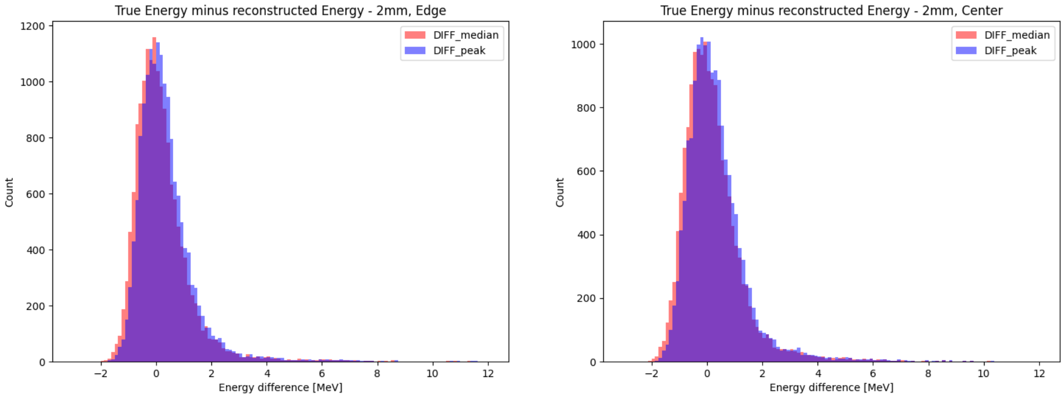

Figure 5.25.: Energy reconstruction test for prototype (**left**) and DarkMESA-like (**right**) setups. The differences between the calibration using the peaks and the medians of the fitted Crystal ball functions were not significant.

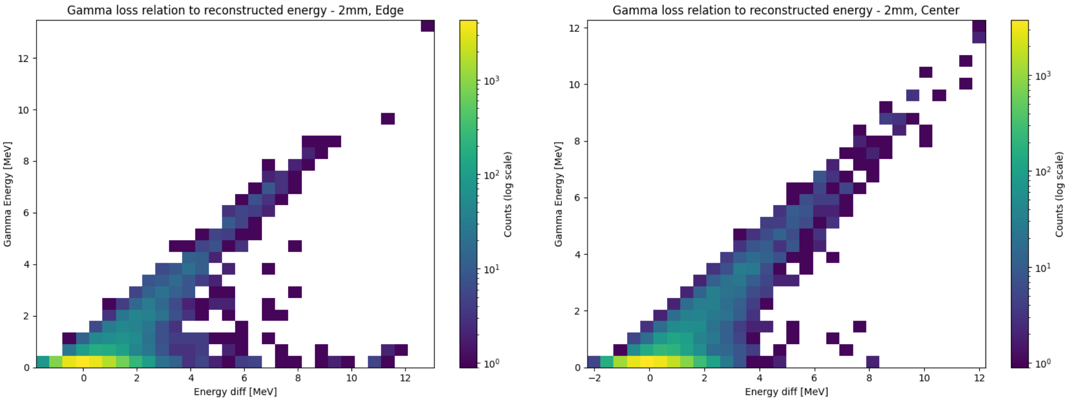

Figure 5.26.: Relation between mismatch of reconstructed energies and energy loss due to bremsstrahlung photons leaving the detector volume for prototype (**left**) and DarkMESA-like (**right**) setups.

Further a difference between DarkMESA-like and prototype simulation can be found near the x-axis. For the prototype simulation, there were several events with a large mismatch in reconstructed to true energy, but no photons were emitted. This is most likely due to scattering of the electrons causing short tracks and many photons being absorbed by the detector walls, as reflective qualities of the walls were not implemented in the simulation.

5.2.3. Electron direction determination

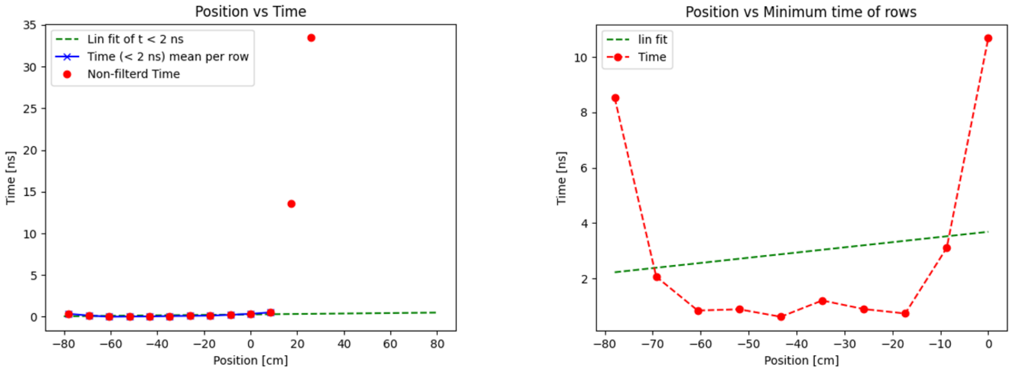

Figure 5.27.: **Left:** Relation between fibre hit time and fibre y-position obtained directly from the Geant4 simulation. **Right:** Relation between SiPM hit time and y-position of the fibre calculated by C^{++} code explained in section 5.1.3. Both show a positive slope.

In order to see if the electron direction could be determined, the simulated arrival time of photons along the y-axis of the prototype was analysed. To this end the first photon hit per row is compared to the y-position. For an electron travelling along the y-axis, the arrival time should increase with y-position. This can be seen when looking at the raw fibre hit time information obtained directly from Geant4 (fig. 5.27 (left) and fig. 5.28(left)). However, taking into account the effect of the wavelength shifting fibres, the timing resolution is worsened. This has several causes. A large portion of photons are lost, as they are not captured by total internal reflection inside the fibres. Photons can also travel up or downwards in the fibre after being shifted, which delays about half of the captured photons. And finally, the mechanisms inside the fibre adds a time spread to the re-emission of the wavelength shifted photons.
This change in the timing information can be seen in figures 5.27 and figures 5.28.

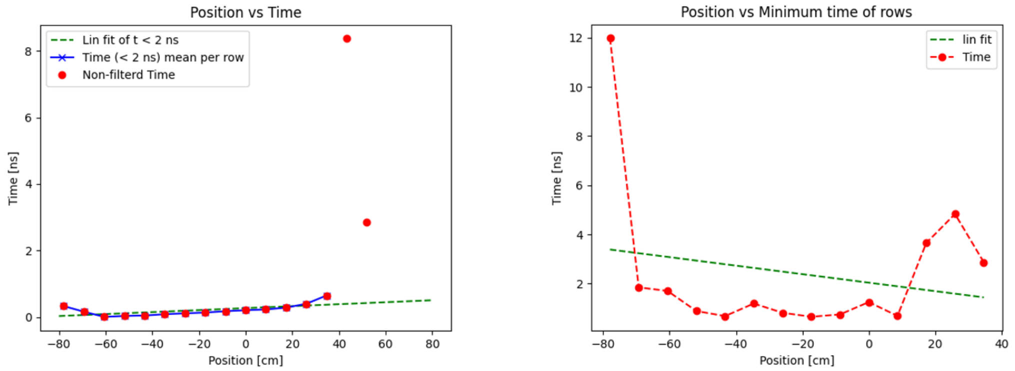

Figure 5.28.: **Left:** Relation between fibre hit time and y-position. This is similar to the event shown in fig. 5.27. **Right:** Relation between SiPM hit time and fibre y-position. The sign of the slope has changed after calculation the SiPM hit times.

Therefore, it is not possible to reliably determine the direction of travel using this prototype. Whereas in figure 5.27 the linear fit to the calculated SiPM hit times would still return a positive slope and therefore the correct direction of travel, this is not the case for the event shown in figure 5.28.

5.3. Cosmic ray background

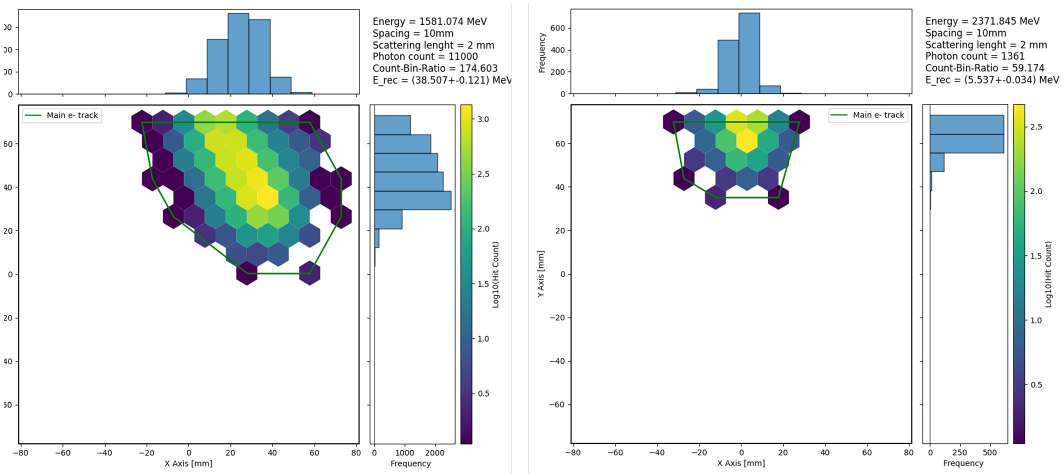

Figure 5.29.: Event signatures of muons hitting the prototype detector. **Left:** The muon hit the detector at about (30, 30) mm and travelled to the detector wall. The reconstructed energy of about 38 MeV does not match beam electron energies. **Right:** An edge-clipper event. Track signature and reconstructed energy would match expected electron beam events closely.

The response for the detector to cosmic ray muons was also simulated. For this the particle generation of the simulation was changed. Muons were generated with the appropriate energy and angular distributions by using the Geant4 ”Cosmic-ray Shower Library” (CRY) [31]. For most cases, these events can be easily distinguished from electron interaction due to the significantly higher hit counts or higher deposited energies. Muons do not get stopped even in large amounts of scintillator, which can be seen in figure 5.31. Therefore, the energy deposited in the detector depends mostly just on the detector size and entry point.

For the prototype detector, cosmic events like the ones in figure 5.29 are expected. The event shown in the left panel could be easily rejected due to the large energy deposition or photon count. However, the event shown in the right panel can not be distinguished from a beam electron event, since the size and photon count match the expectation for a low energy electron. These events are called ”edge-clippers”. As the name implies, they are caused by muons hitting the upper or lower edges of the scintillator volume and leaving it after only travelling small distances inside of it. Both event signatures were seen in the constructed detector prototype (see sec. 6.2).

The signals of edge-clippers are only a potential concern for the detector prototype. In a potential DarkMESA use case, the signals are expected to appear inside the detector volume as described in sec. 5.1.2. The signals due these edge-clippers can be disregarded by defining a fiducial volume inside the larger total detector volume and excluding events that take place near the sides of the detector. By excluding these regions, noise caused by potential radioactivity of the detector vessel materials can also be discriminated.

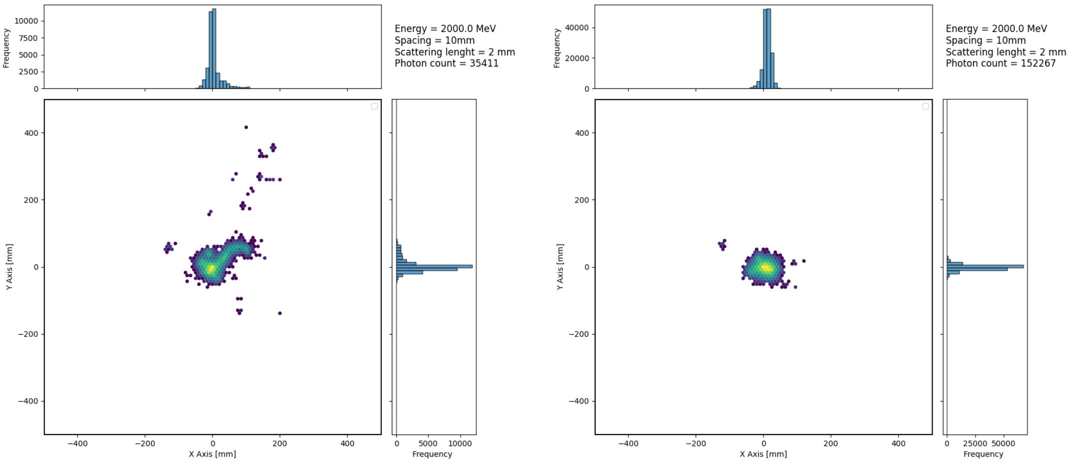

Figure 5.30.: Events caused by cosmic ray muons travelling into the detector plane in a 1 m^3 detector.

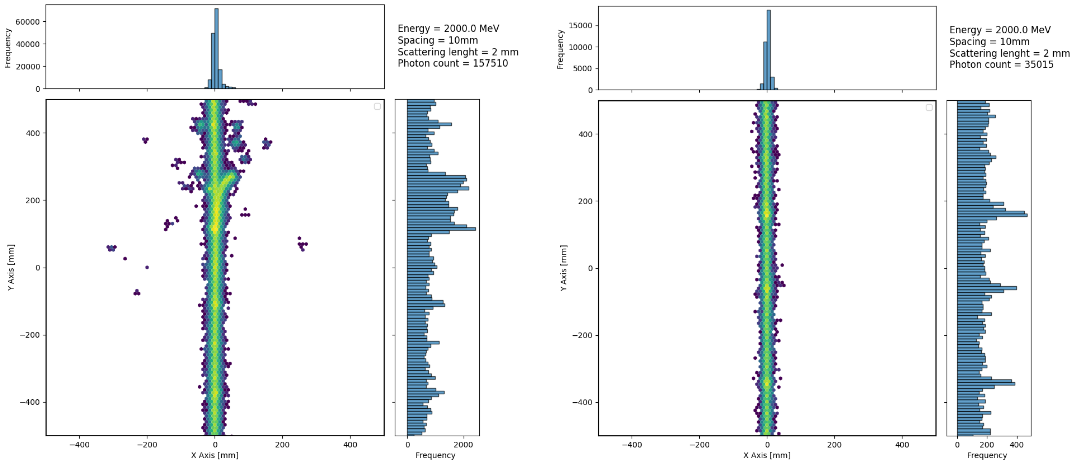

Figure 5.31.: Events caused by cosmic ray muons travelling horizontally through a $1\,\mathrm{m}^3$ detector.

Figures 5.31 and 5.30 show how a final DarkMESA opaque liquid scintillator detector of a cubic $1\,\mathrm{m}^3$ volume would respond to cosmic muons travelling vertically and horizontally through it. The light seen in both cases would far exceed the expected light of Dark Matter interaction.

5.4. Simulation summary

Simulating the detector yielded valuable insights into the expected capabilities of an opaque liquid scintillator detector. Of primary interest was the angular reconstruction of electron events and the energy resolution of the detector. The detector simulation also shows the additional advantage of discriminating mouns from cosmic rays events. In the following chapter, the simulated tests will be cross-checked using the detector prototype in tests at the MAMI accelerator. Since potential noise of electronics was not considered and the assumed fibre properties used in section 5.1.3 are quite optimistic, the results are most likely overly optimistic and a reduced performance of the prototype in the considered capabilities has to be expected.

6. Prototype detector measurements

6.1. Setup

The detector was set up in MAMI hall A, directly after the first racetrack microtron (RTM 1) this is shown in figures 6.1 and 6.2. This allowed the use of an electron energy of up to 14 MeV. The beam electron rate was set to roughly 1 kHz. Such a low beam rate was needed due to the maximum trigger rate of the used FERS electronics.

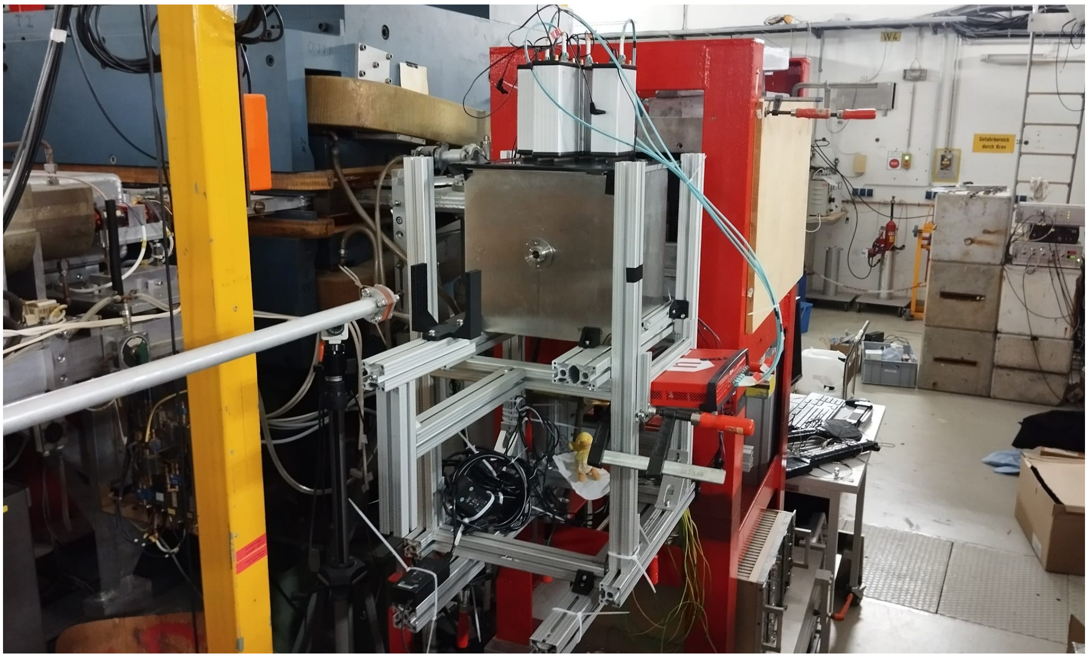

Figure 6.1.: The detector set up at the test site in MAMI hall A. The beamline can be seen on the left side.

For the experiments, the detector was triggered by a small detector, which consists of a thin sheet of plastic scintillator (2 mm thickness). To test the detector response at different energies, multiple attenuator plates could be inserted into a holder directly behind the flange of the beam pipe (see fig. 6.3). Each attenuator is made of aluminium sheets with 2 mm thickness. An electron passing through a plate would lose about 1 MeV of energy. A sketch of the setup is shown in figure 6.4.

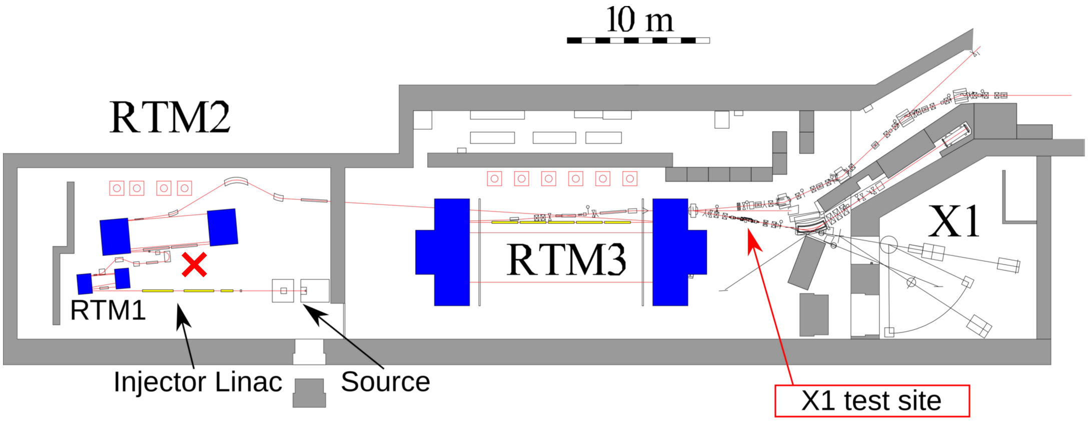

Figure 6.2.: Floor plan of the MAMI accelerator halls A (left side) and B (right side). The position of the test site is marked by a red cross. After passing the RTM 1, the beam energy is 14 MeV. [32]

The bremsstrahlungs-background induced by the attenuators was of little concern, as the detector response of photons can be easily distinguished, due to their characteristic event signature. Also, scattered electrons, that hit the detector at its front-facing wall and don't pass the beam window, can be discarded by event filtering (see sec. 6.3.1).

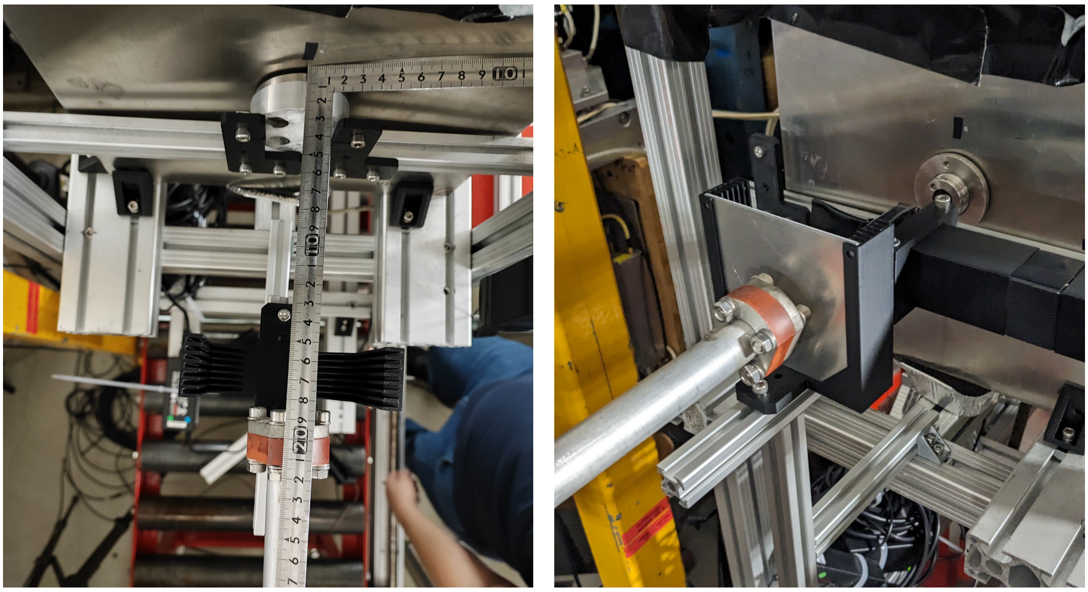

Figure 6.3.: Beamline setup during the experiments at MAMI. **Left:** Bare setup without an attenuator. In front of the beam window is a flange coated with a powder to visualize the beam position for alignment. **Right:** Setup with one attenuator present and the trigger detector in place.

Due to damage to one of the SiPMs on the back part of the grid, the high voltage of the SiPMs connected to board 3 could not be maintained and the grid section at the back (fig. 4.6, left) was unusable during the beam time.

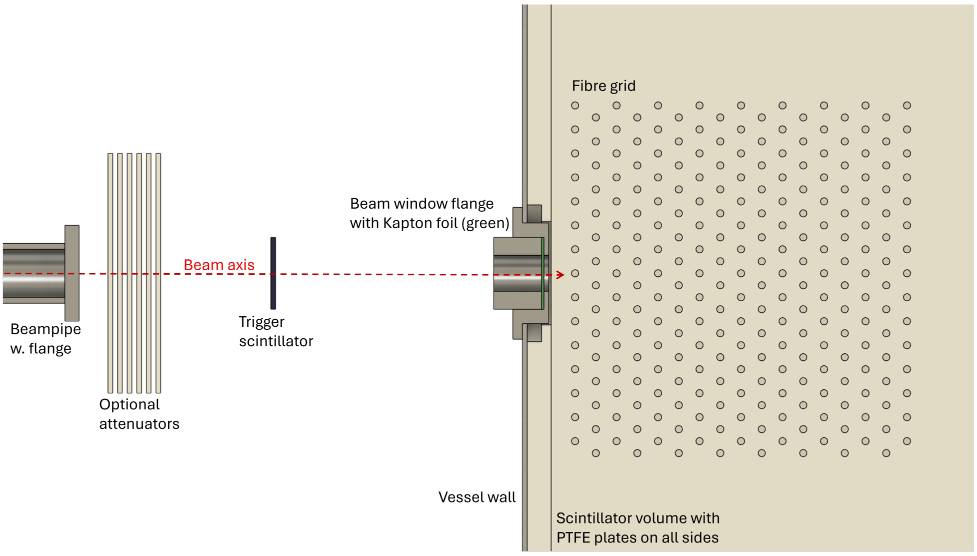

Figure 6.4.: Sketch of the beamline setup.

6.2. Cosmic ray background

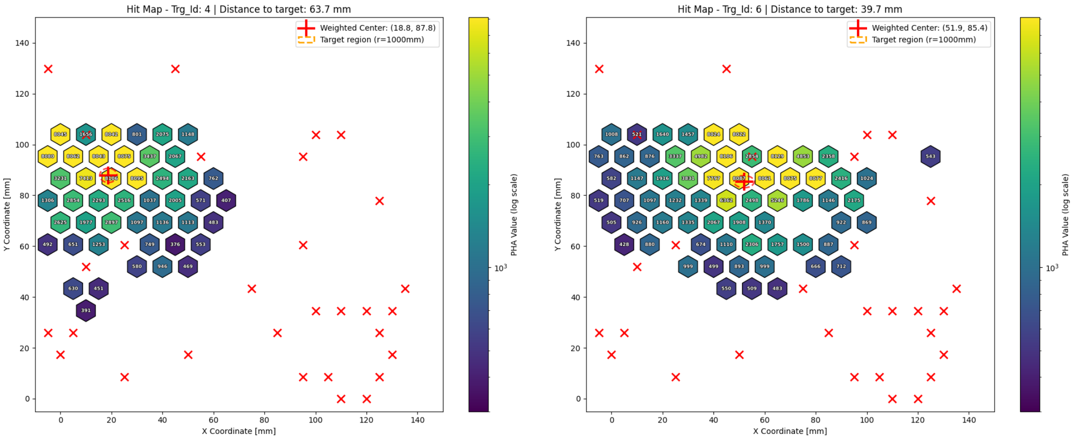

Figure 6.5.: Cosmic events.

Additionally to the electron beam tests, the detector response to cosmic ray muons was tested. For this purpose, two plastic scintillator trigger paddles (10 x 10 x 2 cm) were placed directly underneath the detector with a distance of about 30 cm between them. The detector was then triggered with both paddles in coincidence, so that roughly vertical cosmic rays were recorded, with the cosmic rate being roughly 0.071 Hz.
The cosmics rate was negligible in comparison to beam events, and therefore the paddles were not used as veto detectors while recording beam data.

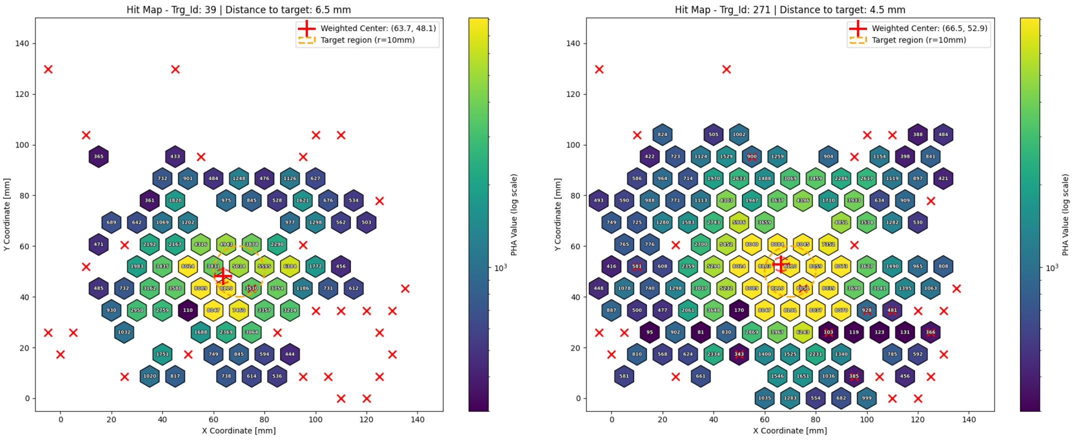

Figure 6.6.: Cosmic events constrained to the centre of the detector.

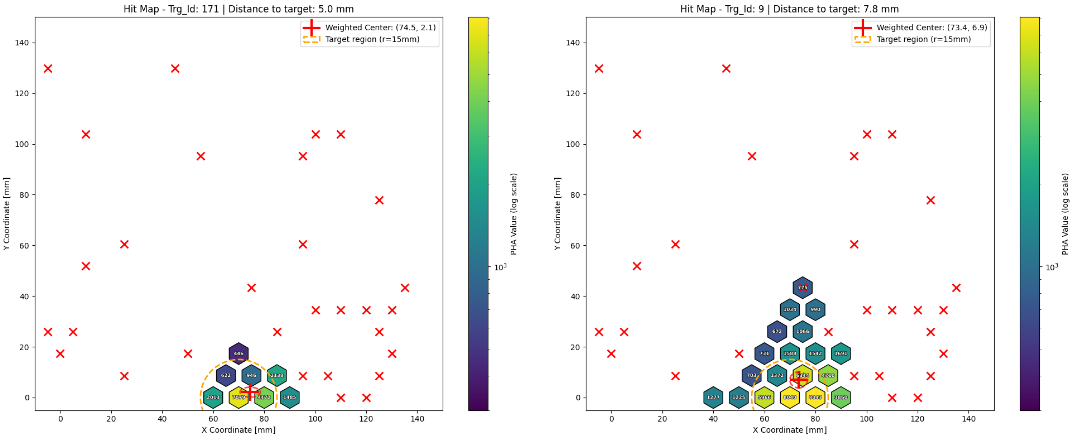

Figure 6.7.: Beam-like cosmic events like the ones simulated in fig. 5.29.

Some example events can be seen in figures 6.5, 6.6 and 6.7. A weighted average of all signals per event is used to determine the centre of the events, which is marked by a red cross in the events shown here. For mostly vertical events, this should be where the muon passed the detector.
Figure 6.8 shows the distribution of these points for all events. An increase in density can be seen close to the sides and back of the volume. This is caused by the scintillator volume at the sides and the back of the fibre grid. Cosmics that hit this part of the detector show only a small signal at the sides of the fibre grid. In contrast, no additional scintillator volume is present at the beam side of the detector, so no increase in centre density can be seen there.

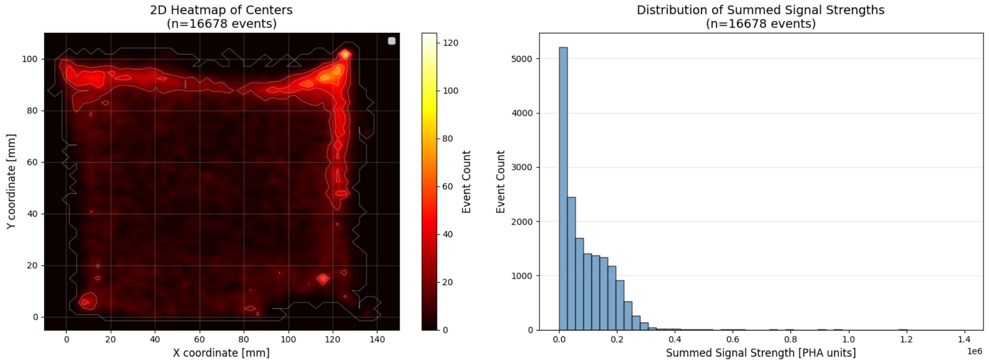

Figure 6.8.: Distribution of all cosmic ray centres and signal strength distribution.

Figure 6.9 shows only events where the determined centre is roughly in the middle of the detector grid. When looking at the signal strength distribution of these events and comparing them to the signal strengths of electron beam events (see fig. 6.27), it is clear that these events show energies well above the beam energies. This matches the results of the simulations seen in sec. 5.3.

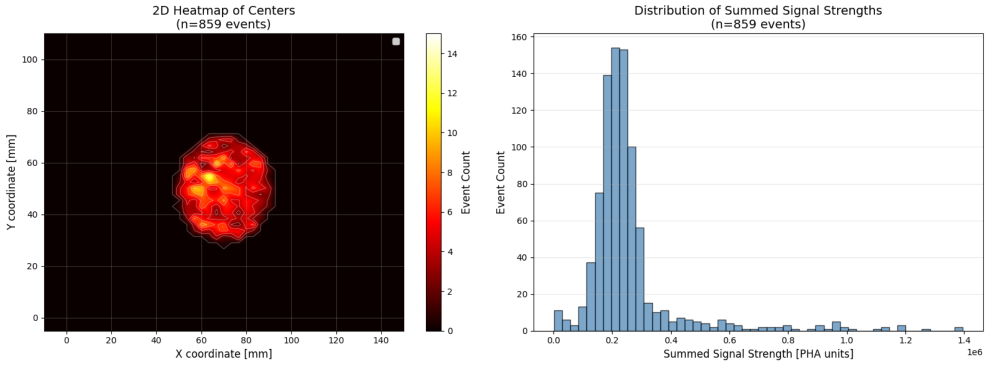

Figure 6.9.: Distribution of events in the centre of the detector grid.

Figure 6.7 shows events that had their centre near the beam window. These closely match with the beam-like muons simulated in sec. 5.3, and could be mistaken for electron tracks. The energies of these events can be in the order of those of beam events. However, the rate of these is in the order of mHz. The beam rate was set to roughly 1 kHz.

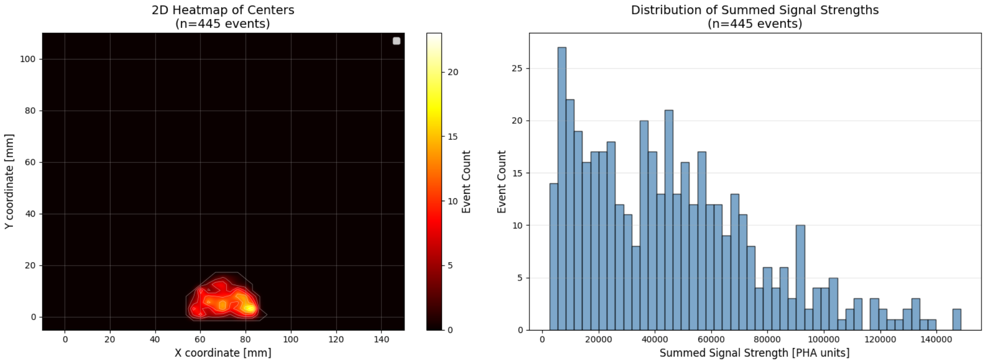

Figure 6.10.: Beam-like cosmic distributions.

6.3. Electron beam

The beamline setup for the experiments was already shown in figure 6.3. Due to the flange of the beam pipe, the attenuators and the trigger detector, many electrons did not reach the detector or hit it off-axis, not going through the beam window. Many of these electrons hit the trigger scintillator, but did not show a track in the detector. In order to analyse only the electrons reaching the beam window, an event selection cut has to be devised.

6.3.1. Event selection cuts

To determine the noise level of each SiPM, the average of non-event-signals has been considered. A dataset of the 6 attenuators is used. For each trigger ID a 5 cm, exclusion radius is drawn around each signal, where a clear signal is observed. Then the signal levels for all channel outside this radius are saved. The average signal strength of these lists for each channel, is then used as the noise level, and a threshold of 5 times the standard deviation is used. Since the signal strengths of beam events is relatively large, this aggressive threshold level does not reject a significant amount of signal events.

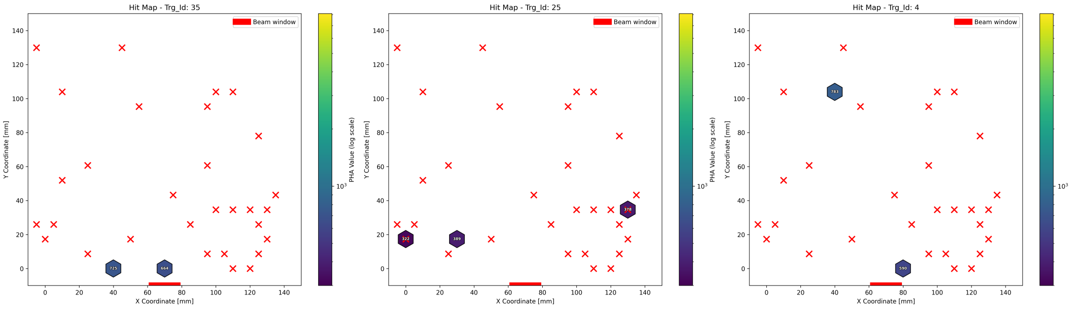

Figure 6.11.: Example events with no clusters, but several signals above the noise threshold. These are caused by the electron hitting the trigger detector, but missing the prototype detector.

The second cut discards events where no signal cluster containing at least 3 signals is present. Also, in order to discard events caused by photons interacting with the scintillator (see fig. 6.12), only events are kept where a signal in the SiPMs of the first row was present. Such photon events were discarded, because there is now way of determining the initial energy, as the detector was not calibrated for energy reconstruction (see sec. 5.2.2).

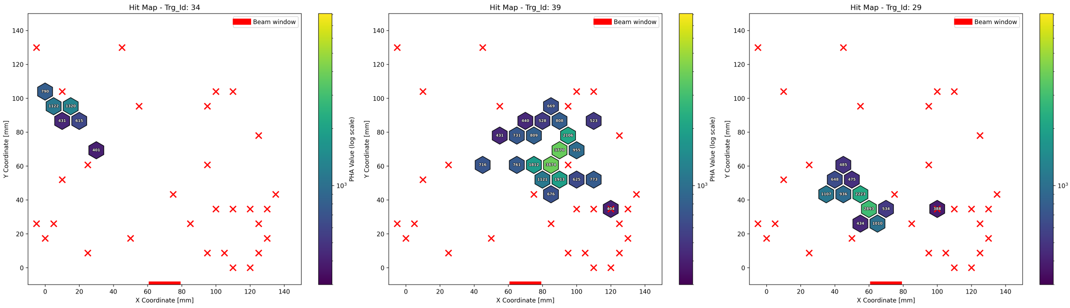

Figure 6.12.: Example events for clusters caused by gamma photons interaction with the scintillator. The electron hit the trigger detector, but misses the volume after emitting a gamma somewhere along the beamline. As mentioned in sec. 3.3.1, gamma photons do not cause tracks but Compton scatter off electrons in the scintillator, creating "blobs".

Many of the electron tracks observed after this track or photon cut are caused by electrons that did not pass through the beam window, instead passing though the 2 mm steel wall of the detector vessel and the 10 mm PTFE plate right behind it (see fig. 6.12). Therefore, the initial angle of these electrons cannot be determined, and the energies can vary drastically (see sec. 6.3.2).
To cut these events, the position of the strongest signal in the first fibre row was checked. An event passes the selection cut, if the strongest signal is right at the position of the beam window (Coordinate (0,70) mm) or immediately next to it and

the signal of the middle fibre is at least half as strong.
However, all cuts only work to filter by the x and y dimensions and there is no information regarding the z-position of any signal. This means that the final beam event selection cut also lets events pass in which an electron was scattered into or out of the detector plane and passes through the detector walls above or below the beam window.

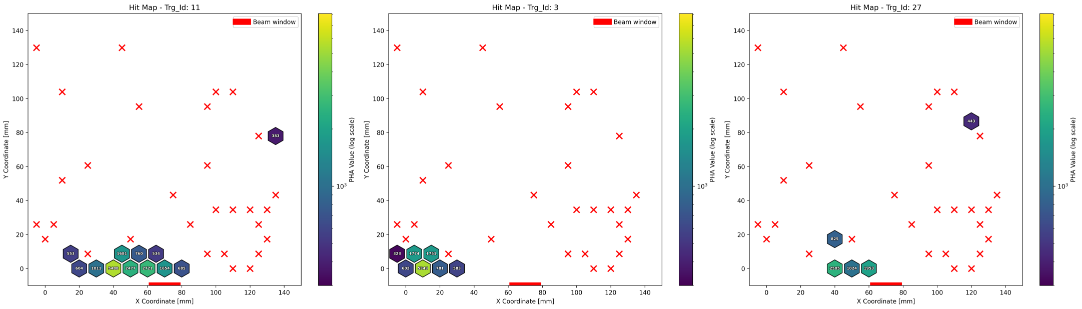

Figure 6.13.: Example events of electron tracks caused by electrons hitting the detector wall. The energy loss inside the detector wall and the PTFE plate causes these tracks to be significantly shorter and have a broader angular distribution due to scattering just before entering the scintillator.

Figure 6.14 shows events that passed these cuts. A significant portion of the events show an abrupt cut after the fifth row at the boundary between the different FERS boards (see fig. 4.6, left). A probable cause of this is a trigger delay between the boards. This drop can also be seen in figure 6.15.

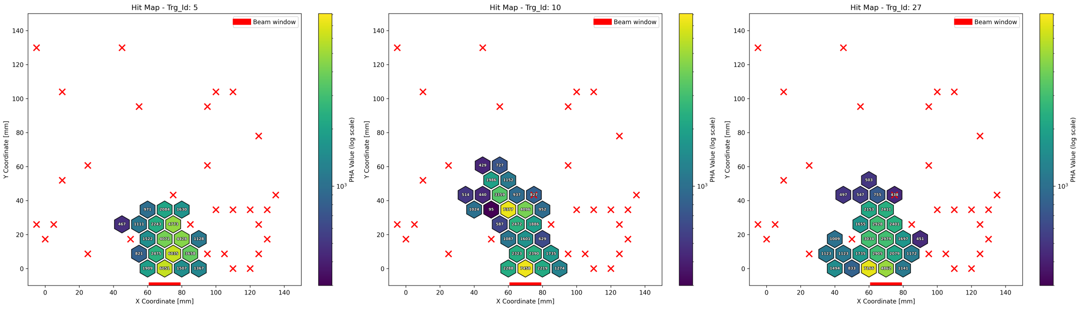

Figure 6.14.: Electron tracks that passed the beam selection cut. These are similar to the simulated tracks seen in figure 5.14, but are narrower and shorter.

The cut events resemble the simulated tracks in sec. 5.2.1, yet show a significantly narrower track. This could be due to the use of the much larger Bubo fibres in the experiment, whereas the simulation just used 3 mm OWL fibres. Also a scintillator with a greatly reduced scattering length in comparison to the simulation was used during the beam time. The simulation used a scattering length of 2 mm, but the scattering length in the experiment is less than 0.5 mm.

When comparing the expected simulated track reach (fig. 6.16) and the results from the prototype measurements (fig. 6.15), it can be seen that the distributions of the beam time tracks is far broader, while the simulation yields nearly Gaussian distributions. An explanation of the high number of short tracks at higher energies could be the filter inefficiency of the cut described in section 6.3.2 (tab. 6.1).

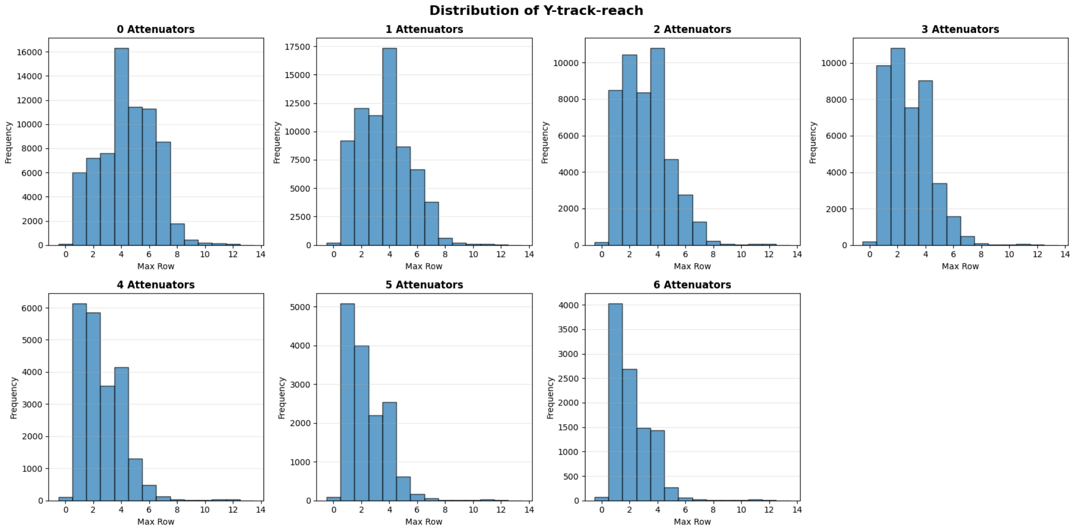

Figure 6.15.: Furthest track reach into the detector, i.e. track length, for all attenuator counts.

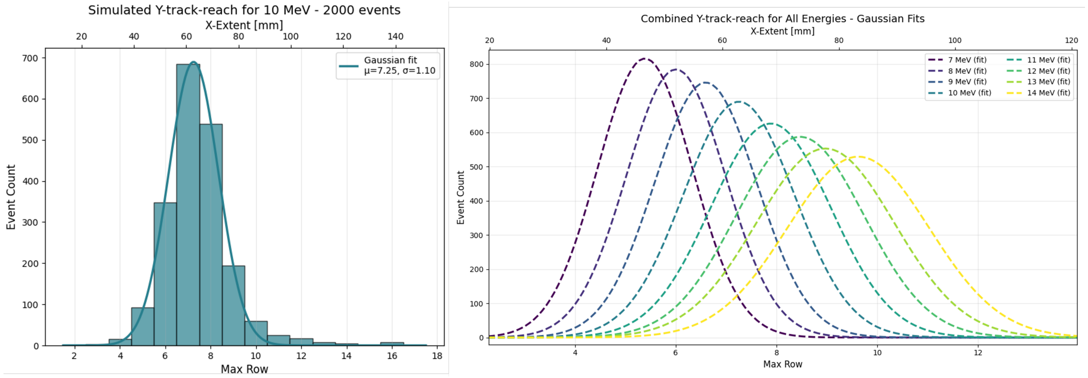

Figure 6.16.: Simulated track reach of energies of 7 to 14 MeV. **Left:** Distribution of electrons at 10 MeV and Gaussian fit. **Right:** Gaussian fits of all simulated electron energies. Other distributions can be found in the appendix A.26

.

6.3.2. Beamline simulation

In order to verify the validity of the applied cuts described in the previous section, a Geant4 simulation of the beamline has been developed. This simulation is shown in figure 6.17. The important components of the setup are the beam pipe flange, attenuators, trigger scintillator, beam window flange and the wall of the detector vessel with the PTFE plate. The dimensions of the setup were measured during the setup of the experiment, but some uncertainties in the relative positioning remain.
The simulation uses electrons with 14 MeV kinetic energy, originating right behind the beam pipe flange and records the following: whether the trigger detector was reached, the final position of particles hitting the detector inside and their angle, as well as the particle energies.

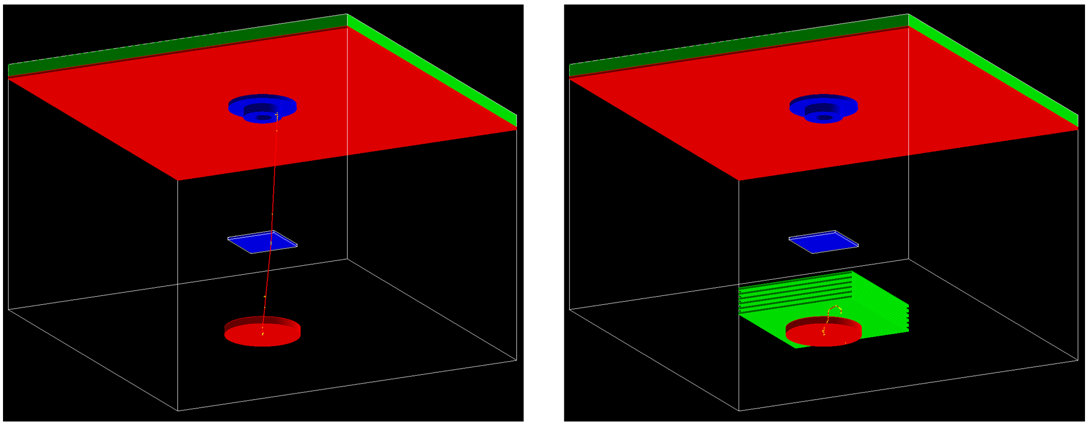

Figure 6.17.: Geant4 beamline simulation. The electron (red track) is generated in front of the beam pipe flange (red), then passes the attenuators (green) before reaching the trigger scintillator (blue) and then travels to the detector wall. There it can hit the wall (red) and potentially pass through it and the PTFE plate (green) or pass through the beam window flange (blue).

Additionally, a second setup was simulated (see fig. 6.20) with the addition of a 15 mm lead plate with a 10 mm diameter hole. This plate acts as shielding for scattered electrons, which would otherwise pass through the detector wall and therefore acts as a collimator. This was done in order to investigate its impact in potential future beam tests. Figures 6.18 and 6.19 show the electron distributions and energy spectra for the simulation with and without the collimator-shield and for 0 and 6 attenuators.

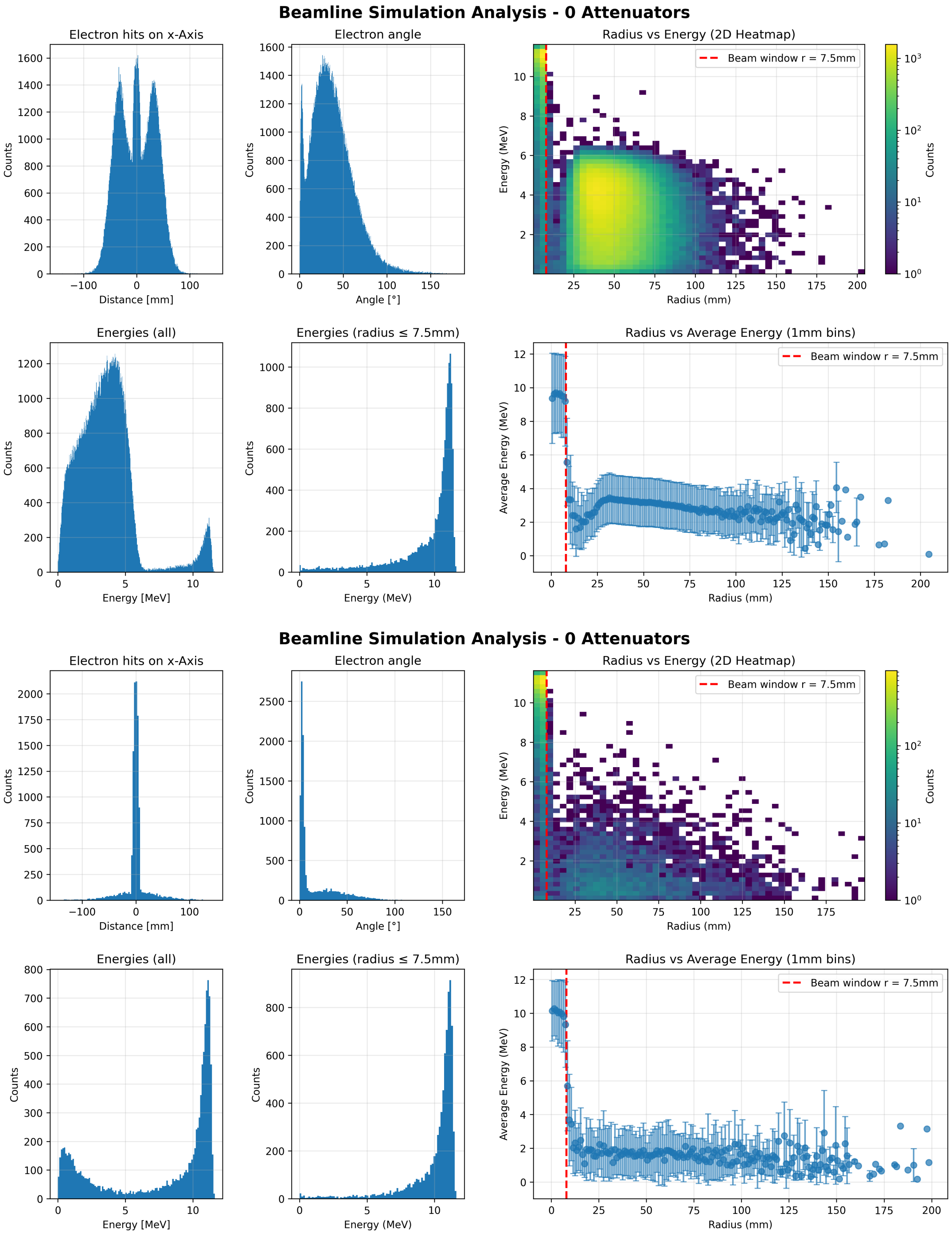

Figure 6.18.: Results of the beamline simulation without any attenuators. The top figure shows the simulation without the collimator-shield and the bottom with the shielding.

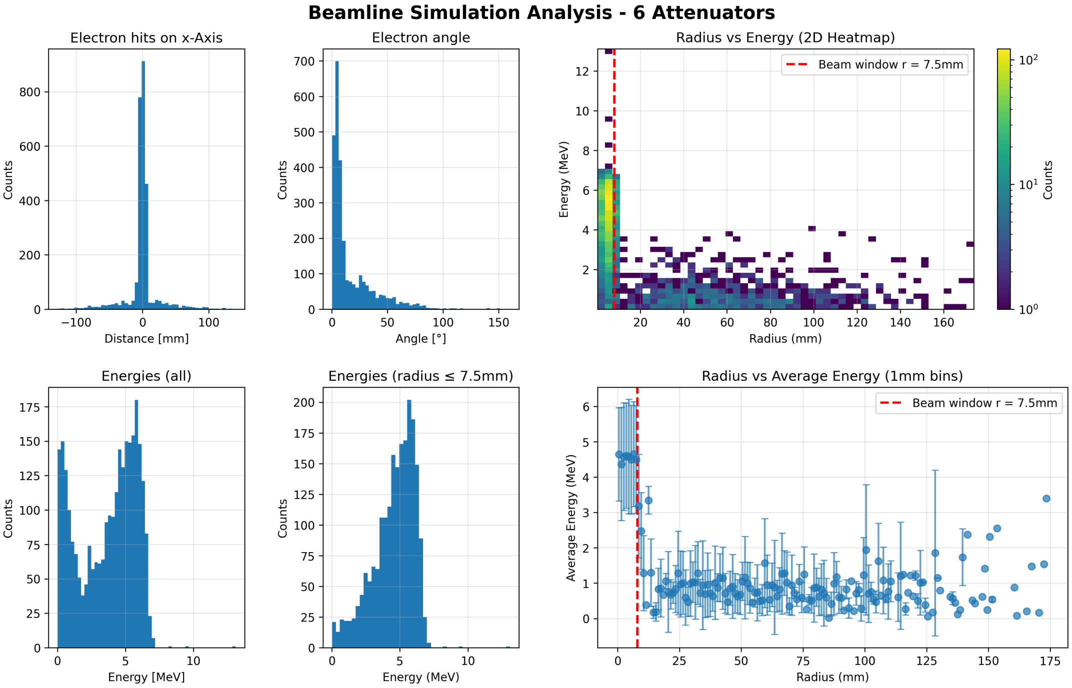

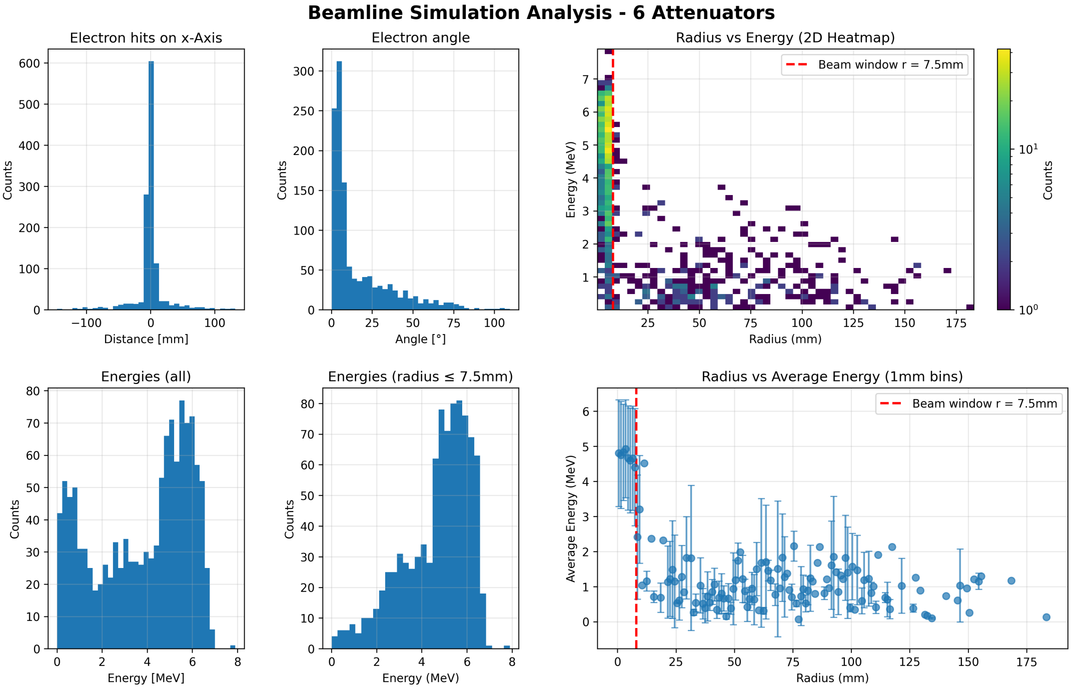

Figure 6.19.: Results of the beamline simulation using 6 attenuators. The top figure shows the simulation without the collimator-shield and the bottom with the shielding.

When comparing the effect of the collimator-shield with no attenuators (fig. 6.18), a strong difference can be observed. The radial distribution without the shielding shows three distinct peaks, which is caused by the geometry of the beam window flange (see fig. 4.3). The thick steel of the flange stops a significant portion of the incoming electrons, whereas the 2 mm steel and 10 mm PTFE of the vessel wall possess far less stopping power. Looking at the complete energy spectrum, one sees a large and broad peak with energies between 0 to 6 MeV. This is caused by electrons being scattered and passing the walls. By using the collimator-shield, all these electrons are stopped and only a clear peak remains. For the energy distribution, only a fractional part of the low energy electrons remain.

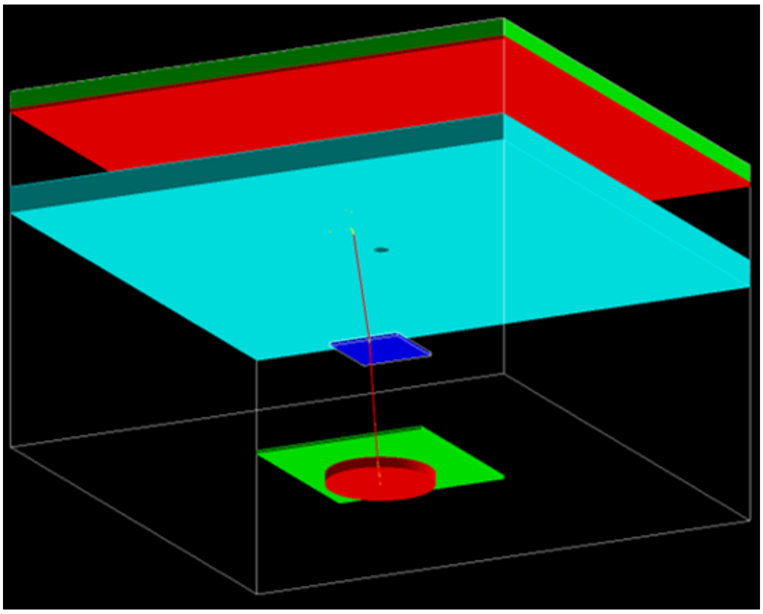

Figure 6.20.: Beamline simulation with the proposed addition of the collimator-shield (cyan).

Figure 6.19 shows a far smaller difference in the distribution in events with 6 attenuators present. This is simply due to the fact that electrons do not have enough energy to pass the vessel wall after the energy loss in the attenuators.

6.3.3. Rate comparison

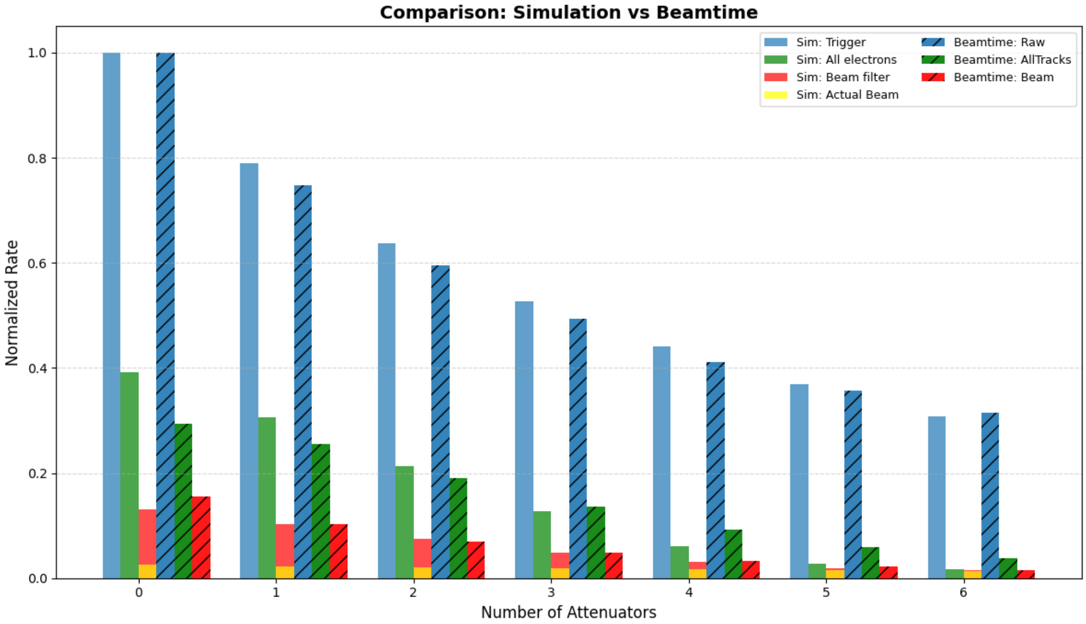

Figure 6.21.: Event rates after applying the selection cuts, comparing the beamline simulation to the experiments at MAMI. Yellow shows the simulated rate of electrons actually passing through the beam window and not above or below.

Att.	Beam rate after cuts (beam time)	Rate of simulated electrons passing the beam window	Cut accuracy [%]
0	0.1312	0.0259	19.74
1	0.1029	0.0223	21.67
2	0.0752	0.0205	27.26
3	0.0486	0.0183	37.65
4	0.0302	0.0170	56.29
5	0.0187	0.0146	78.07
6	0.0145	0.0128	88.28

Table 6.1.: Performance of simulated beam selection cuts (normalized rates). Cut efficiency is defined as the ratio of event rates after cuts between beam time data and simulated electrons passing through the beam window but not the wall detector.

Figure 6.21 shows a comparison between the normalized event rates after the the selection cuts for simulated and experimental data. To estimate the rate of tracks seen after applying the "AllTracks" cut (fig. 6.13), the rate of all electrons reaching the inside of the detector in the simulation was taken. The simulated beam track

rate was calculated by taking the rate of electrons reaching the inside detector with a horizontal distance from the middle of 20 mm. This also incorporates electrons reaching the detector inside above and below the beam window.
The rate of simulated electrons actually passing the beam window was also calculated. As mentioned already, this could not be determined for the experiment.
When comparing simulated and experimental data after applying the selection cuts, some differences can be found for the total and "AllTracks" rates. These are however reasonably small and lead to the conclusion that either the geometry of the simulation setup was somewhat flawed or some physical aspect, like the exact placements, have been incorrectly approximated in the simulation.
The real and simulated cut beam rates match very well. However, looking at the simulated actual beam rate, it becomes clear that for higher energies, a large percentage of these events are caused by electrons not passing the beam window, but rather the detector wall above and below. Table 6.1 shows the accuracy of the beam cut. For high energies (i.e. no attenuator), up to 80.26 % of all retained events by the cuts could be misidentified.

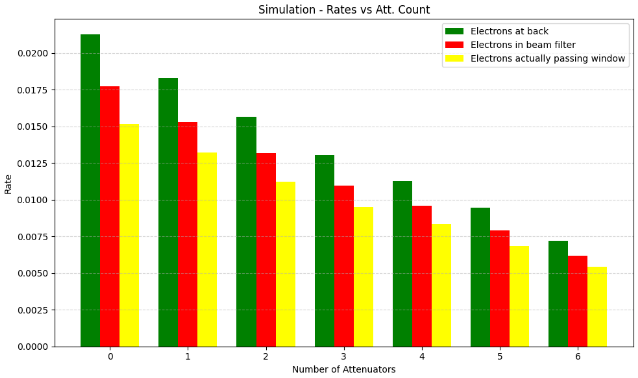

Figure 6.22.: Expected rates after the cuts and actual rate of electrons passing the beam window with the use of the proposed collimator-shield (15 mm lead with 10 mm hole)

This performance could be massively increased by using the collimator shield proposed in the previous section. Table 6.2 shows the simulated efficiencies using a 15 mm lead collimator-shield. This could potentially be further improved by using thicker lead or, even an active veto system.

Att.	Beam rate after cuts (simulation w. shielding)	Rate of simulated electrons passing the beam window	Cut accuracy [%]
0	0.0177	0.0151	85.31
1	0.0153	0.0132	86.27
2	0.0132	0.0112	84.85
3	0.011	0.0095	86.36
4	0.0096	0.0083	86.46
5	0.0079	0.0068	86.08
6	0.0062	0.0054	87.10

Table 6.2.: Simulated beam selection cut performance the with proposed collimator-shield as seen in figure 6.22. When comparing to fig. 6.1, a significantly higher accuracy can be found.

6.3.4. Angular reconstruction

To reconstruct the initial angle of the electrons, a weighted linear fit was performed, similar to the method described in sec. 5.2.1. For most events at higher electron energies, the fits look similar to the examples in figure 6.23. At these energies, the detector is capable to reconstruct the initial angles, even with the simple linear fit approach.

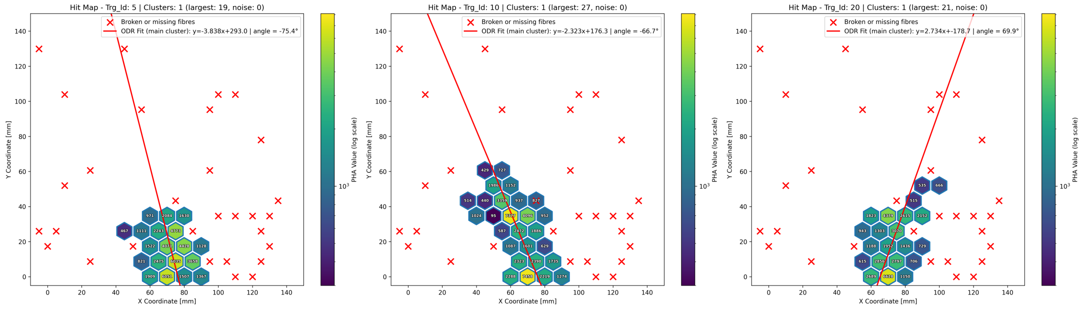

Figure 6.23.: Examples of good angular fits at high electron energies with no attenuators.

However, similar to the simulated beam time setup (sec. 5.2.1, fig. 5.15), the problem can arise when the track is shortened by bremsstrahlung photon emission and vertical scattering and the linear approach fails. This can be observed in figure 6.24. The fits seen in figure 6.25 show what predominately happens at high attenuator counts and therefore low electron energies. Due to the extremely short tracks, the angle can not be reconstructed.

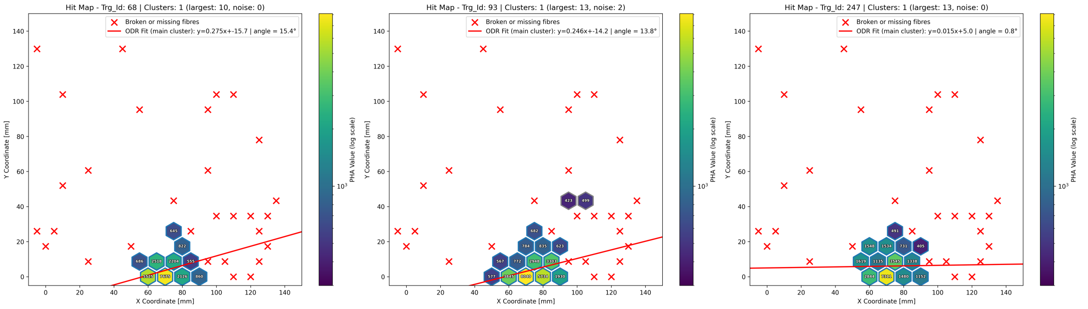

Figure 6.24.: Examples of failing angular fits at high electron energies due to short tracks caused by energy loss or vertical scattering.

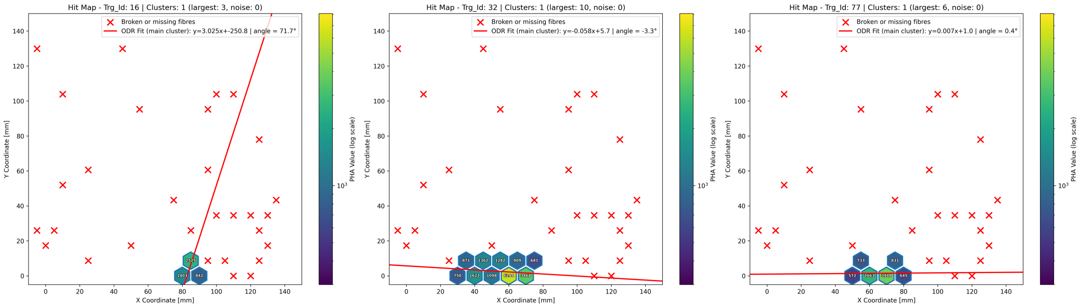

Figure 6.25.: Angular fits for low energies. The angles can not be reconstructed reliably.

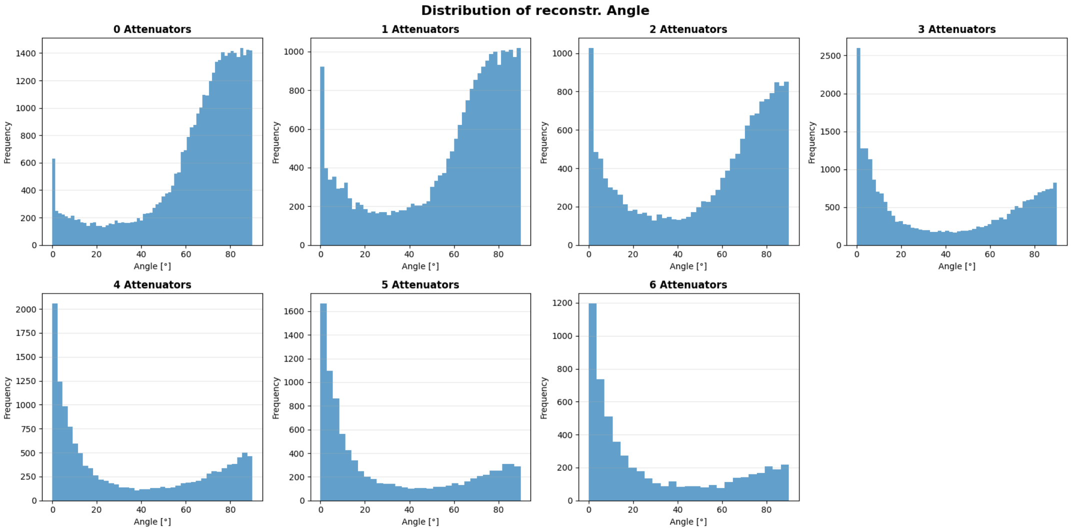

Figure 6.26.: Angular distribution of different attenuator counts. The angle is given in degrees in relation to the x-axis, defining the initial angle as 90°.

The distribution of the fitted electron angles can be found in figure 6.26. At high energies, the angular reconstruction works well, however at lower energies, the tracks becomes too short. For 6 attenuators (energy of about 5 MeV), only a small peak at 90° can be seen.

6.3.5. Energy deposition

To analyse the energy deposition of each event, the signal strength of all channels was summed. Due to tight time constraints, it was not possible to determine the conversion of signal strength to photo electron count for the SiPMs. The resulting distributions can be seen in figure 6.27.

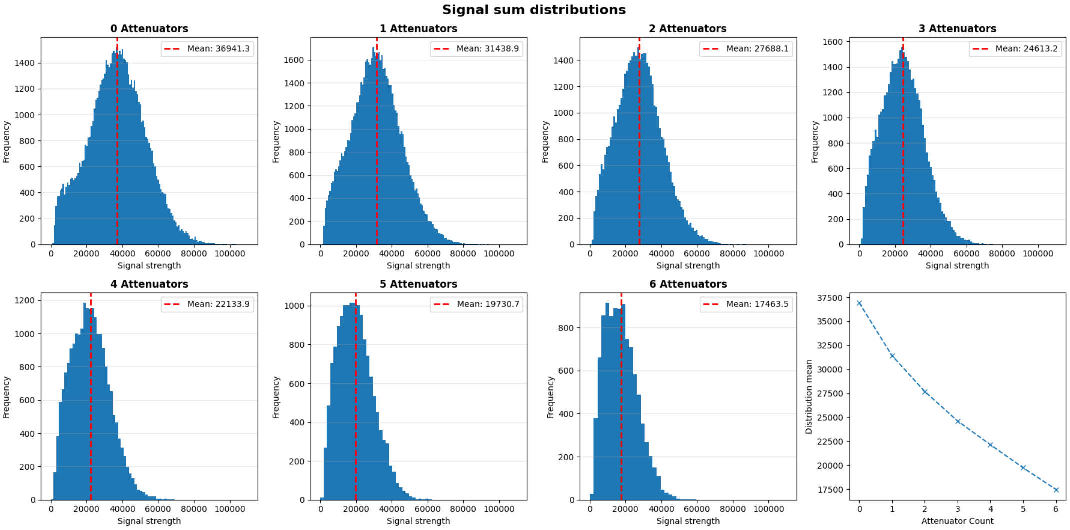

Figure 6.27.: Energy deposition of all attenuator counts as well as the relation between distribution mean and attenuator count.

For higher electron energies, a bump on the left side of the distribution can be seen. This is most likely caused by electrons passing the detector walls above or below the beam window. At low energies, the simulation of the beamline shows that this should not appear, since lower energy electrons will not be able to pass the steel detector wall and PTFE plate.

The relation between the mean energy deposition and attenuator count appears to be almost linear, as expected.

7. Summary and conclusion

The goal of this thesis was to investigate the potential use of opaque liquid scintillators in the DarkMESA experiment. This detector technology utilises confined scattered due to the addition of wax in the scintillator medium to confine scintillation light close to its point of origin. In combination with the use of optimised wavelength shifting fibres, this allows the retention of topological information inside the detector.

In this thesis, a prototype detector was constructed to track electrons produced by the MAMI accelerator. This was done to simulate events caused by the potential scattering of Dark Matter particles off electrons inside the detector. Using an opaque scintillator, it may be possible to reconstruct the scattering angle and discriminate such events from background sources, like radioactivity and cosmic rays.

The potential performance of this detector was assessed using a Geant4 simulation. These simulation studies showed promising first results regarding the angular reconstruction capability and energy resolution of the prototype detector. The detector's response to cosmic ray muons was also simulated, which highlighted the technology's capability to discriminate signals caused by such events.
Several shortcomings of the current design were identified during construction of the prototype. Nevertheless, these studies helped to establish a construction procedure that will be invaluable for a future improved detector design.
The response of the prototype detector to cosmic ray muons closely matched the simulation results. The electron beam measurements demonstrated that the detector is capable of recording spatially resolved light patterns consistent with expectations from simulation. Further analysis of the data gathered during the beam time revealed an inferior performance compared to the simulation.
However, this is to be expected from this proof-of-concept prototype. The simulation results should be regarded as representing a best-case scenario, since the effects of electronic readout noise were not included and the assumed performance of the wavelength-shifting was assumed to be close to perfect. The Bubo fibres used in the prototype were not included in the simulation and should be implemented in a future version in order to better understand their impact on detector performance.

The development of a second-stage detector is already being discussed and is expected to further enhance performance by addressing the design limitations highlighted in this thesis.

Bibliography

[1] M. Böhles, S. Böser, M. Eisenhuth, et al.
Combining hybrid and opaque scintillator techniques in the search for double beta plus decays - a concept study for the nudoubt experiment.
Eur. Phys. J. C, 85(121), 2025.
`doi:10.1140/epjc/s10052-025-13847-1`.

[2] F. Zwicky.
Die Rotverschiebung von extragalaktischen Nebeln.
Helv. Physica Acta., 6:110, 1933.

[3] V.C. Rubin *et al.*
Extended rotation curves of high-luminosity spiral galaxies.
Astrophys. Journal, 225:107, 1978.

[4] Hermann Kolanoski.
Einführung in die Astroteilchenphysik, 2009.
URL: `https://www-zeuthen.desy.de/~kolanosk/astro0910/skripte/astro.pdf`.

[5] Douglas *et al.* Clowe.
A direct empirical proof of the existence of dark matter.
Astrophys. J. Lett., 648:L109–L113, 2006.
`arXiv:astro-ph/0608407`, `doi:10.1086/508162`.

[6] Mordehai Milgrom.
MOND laws of galactic dynamics.
Mon. Not. Roy. Astron. Soc., 437(3):2531–2541, 2014.
`arXiv:1212.2568`, `doi:10.1093/mnras/stt2066`.

[7] M. *et al.* Tanabashi.
Review of particle physics.
Phys. Rev. D, 98:030001, Aug 2018.
URL: `https://link.aps.org/doi/10.1103/PhysRevD.98.030001`, `doi:10.1103/PhysRevD.98.030001`.

[8] European Space Agency (ESA).
Cosmic microwave background seen by planck, 2019.
Last visited on 09.02.2026.
URL: `https://sci.esa.int/s/WLGmGdw`.

[9] Luca Doria.
Search for New Physics with Intense Pion and Electron Beams.
Habilitation Thesis, Johannes Gutenberg-Universitat Mainz, 2018.

[10] Institut für Theoretische Physik und Astrophysik, Julius-Maximilians-Universität Würzburg.
Mev dark matter freeze-out, 2025.
Bachelor and Master thesis topics description.
URL: `https://www.physik.uni-wuerzburg.de/en/astro/studium-der-astronomie/bachelor-und-masterarbeitsthemen/mev-dark-matter-freeze-out/`.

[11] R. D. Peccei.
The Strong CP problem and axions.
Lect. Notes Phys., 741:3–17, 2008.
`arXiv:hep-ph/0607268`, `doi:10.1007/978-3-540-73518-2_1`.

[12] Denig, Achim.
Review of dark photon searches.
EPJ Web Conf., 130:01005, 2016.
`doi:10.1051/epjconf/201613001005`.

[13] Wikimedia Commons.
Doppelbeta-massenparabel.png, July 2005.
Last visited on 09.02.2026.
URL: `https://commons.wikimedia.org/wiki/File:Doppelbeta-massenparabel.png`.

[14] Frank T. Avignone, Steven R. Elliott, and Jonathan Engel.
Double beta decay, majorana neutrinos, and neutrino mass.
Rev. Mod. Phys., 80:481–516, Apr 2008.
URL: `https://link.aps.org/doi/10.1103/RevModPhys.80.481`, `doi:10.1103/RevModPhys.80.481`.

[15] Ettore Majorana.
Teoria simmetrica dell'elettrone e del positrone.
Nuovo Cim., 14:171–184, 1937.
`doi:10.1007/BF02961314`.

[16] Matteo Agostini, Giovanni Benato, Jason A. Detwiler, Javier Menéndez, and Francesco Vissani.
Toward the discovery of matter creation with neutrinoless double-beta decay.
Rev. Mod. Phys., 95:025002, Apr 2023.
`arXiv:2202.01787`, `doi:10.1103/RevModPhys.95.025002`.

[17] Sebastian Stengel.
Design and development of the MAGIX Trigger veto system.
PhD thesis, Mainz, 2024.
`doi:10.25358/openscience-12071`.

[18] F. Hug *et al.*
MESA - an ERL Project for Particle Physics Experiments.

In *Proc. of Linear Accelerator Conference (LINAC'16), East Lansing, MI, USA, 25-30 September 2016*, number 28 in Linear Accelerator Conference, pages 313–315, Geneva, Switzerland, May 2017. JACoW.
https://doi.org/10.18429/JACoW-LINAC2016-MOP106012.
URL: `http://jacow.org/linac2016/papers/mop106012.pdf`, `doi:10.18429/JACoW-LINAC2016-MOP106012`.

[19] Patrick Achenbach and Mirco Christmann.
Application of accelerator beam dumps for dark matter searches.
Nuclear Science and Engineering, 198(1):1–6, 2024.
`arXiv:https://doi.org/10.1080/00295639.2022.2151301`, `doi:10.1080/00295639.2022.2151301`.

[20] Luca Doria *et al.*
Dark Matter at the Intensity Frontier: the new MESA electron accelerator facility.
Proceedings of Science (PoS), ALPS2019 Conference, 2019.
`arXiv:1908.07921`.

[21] Hermann Kolanoski and Norbert Wermes.
Teilchendetektoren: Grundlagen und Anwendungen.
Springer Spektrum, Berlin, Heidelberg, 1 edition, 2016.
`doi:10.1007/978-3-662-45350-6`.

[22] Y. Zhang, Z.Y. Yu, X.Y. Li, Z.Y. Deng, and L.J. Wen.
A complete optical model for liquid-scintillator detectors.
Nuclear Instruments and Methods in Physics Research Section A: Accelerators, Spectrometers, Detectors and Associated Equipment, 967:163860, July 2020.
URL: `http://dx.doi.org/10.1016/j.nima.2020.163860`, `doi:10.1016/j.nima.2020.163860`.

[23] LiquidO Consortium.
Neutrino physics with an opaque detector.
Commun. Phys., 4:263, 2021.
`doi:10.1038/s42005-021-00763-5`.

[24] Benjamin Bastian-Querner, Till Dieminger, Timo Karg, Reyn Kramer, Kai Krings, Lora Martin, Matthias Plum, and Christopher Wiebusch.
The wavelength-shifting optical module, 2021.
`doi:10.48550/arXiv.2112.12258`.

[25] Bastian Keßler.
Optimized wavelength-shifting fibers (owls) for a high photon capture-rate.
Poster presented at EPS-HEP 2025, Hamburg, Germany, July 2025.
URL: `https://indico.in2p3.fr/event/33627/contributions/155325/`.

[26] Sebastian Böser.
Photon emission in owl fibres.
Unpublished, used with permission.

[27] Miriam Weigand.
Construction of a test setup and characterization of wavelength shifting fibres and opaque scintillator properties for NuDoubt^{++}.
Master's thesis, Johannes Gutenberg University Mainz, 2026.

[28] J. Allison et al.
Recent developments in geant4.
Nuclear Instruments and Methods in Physics Research Section A, 835:186–225, 2016.
`doi:10.1016/j.nima.2016.06.125`.

[29] Kitzia M. Hernandez Curiel.
Event reconstruction for an opaque liquid scintillator detector.
Master's thesis, Johannes Gutenberg University Mainz, 2025.

[30] John Erthal Gaiser.
Charmonium Spectroscopy From Radiative Decays of the J/ψ and ψ'.
Ph.d. thesis, SLAC, 8 1982.

[31] Lawrence Livermore National Laboratory.
Physics simulation packages.
Last visited 09.02.2026.
URL: `https://nuclear.llnl.gov/simulation/`.

[32] S. *et al.* Riordan.
Study of light backgrounds from relativistic electrons in air light-guides.
Nucl. Instrum. Methods Phys. Res. A, 895:1–8, 2018.
`arXiv:1710.07100`, `doi:10.1016/j.nima.2018.04.029`.

[33] Anycubic.
Abs-like resin 2.0.
Technical specifications and datasheet.
URL: `https://de.anycubic.com/collections/jubilaumsverkauf/products/abs-like-resin-2`.

[34] CAEN SpA.
FERS-5200 Front-End Readout System.
CAEN SpA, Viareggio, Italy.
Product brochure and technical specifications.
URL: `https://www.caen.it/subfamilies/fers-5200/`.

[35] onsemi.
J-Series Silicon Photomultipliers (SiPM): High PDE and Timing Resolution Sensors.
onsemi, 2021.
Datasheet, document number: MicroJ-Series-D.
URL: `https://www.onsemi.com/products/sensors/photodetectors-sipm-spad/silicon-photomultipliers-sipm/j-series`.

A. Appendix

A.1. Prototype construction

A.1.1. Prototype technical drawings

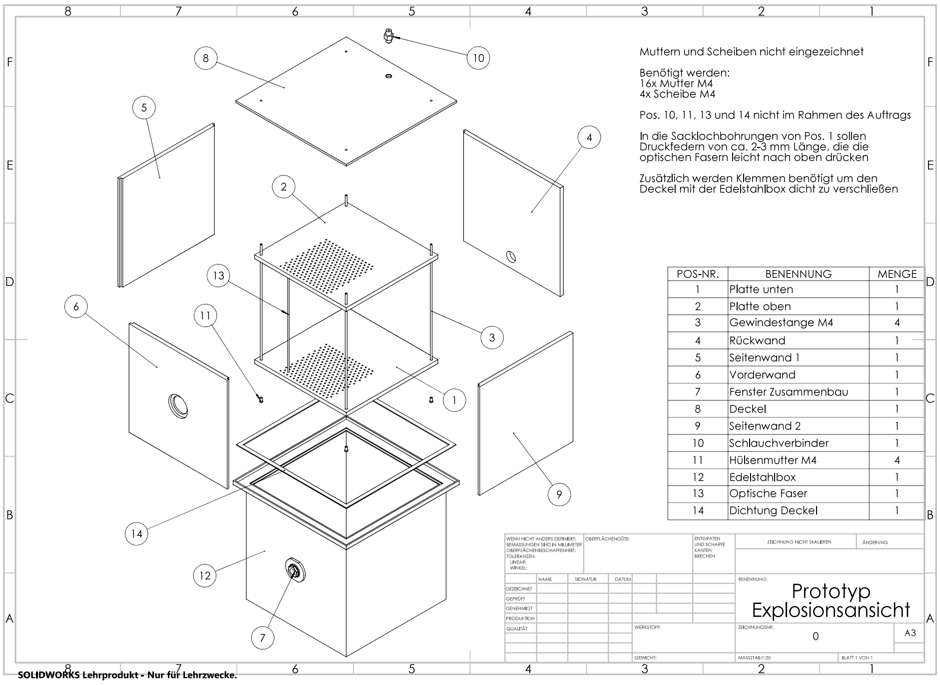

Muttern und Scheiben nicht eingezeichnet

Benötigt werden:
16x Mutter M4
4x Scheibe M4

Pos. 10, 11, 13 und 14 nicht im Rahmen des Auftrags

In die Sacklochbohrungen von Pos. 1 sollen Druckfedern von ca. 2-3 mm Länge, die die optischen Fasern leicht nach oben drücken

Zusätzlich werden Klemmen benötigt um den Deckel mit der Edelstahlbox dicht zu verschließen

POS-NR.	BENENNUNG	MENGE
1	Platte unten	1
2	Platte oben	1
3	Gewindestange M4	4
4	Rückwand	1
5	Seitenwand 1	1
6	Vorderwand	1
7	Fenster Zusammenbau	1
8	Deckel	1
9	Seitenwand 2	1
10	Schlauchverbinder	1
11	Hülsenmutter M4	4
12	Edelstahlbox	1
13	Optische Faser	1
14	Dichtung Deckel	1

WENN NICHT ANDERS DEFINIERT:
BEMASSUNGEN SIND IN MILLIMETER
OBERFLÄCHENBESCHAFFENHEIT:
TOLERANZEN:
LINEAR:
WINKEL:

OBERFLÄCHENGÜTE:

ENTGRATEN UND SCHARFE KANTEN BRECHEN

ZEICHNUNG NICHT SKALIEREN

ÄNDERUNG

	NAME	SIGNATUR	DATUM
GEZEICHNET			
GEPRÜFT			
GENEHMIGT			
PRODUKTION			
QUALITÄT			

BENENNUNG: Prototyp Explosionsansicht

WERKSTOFF:

ZEICHNUNGSNR. 0

A3

GEWICHT:

MASSSTAB:1:20

BLATT 1 VON 1

Figure A.1.: Page 1 of detector drawing by Fabian Piermaier

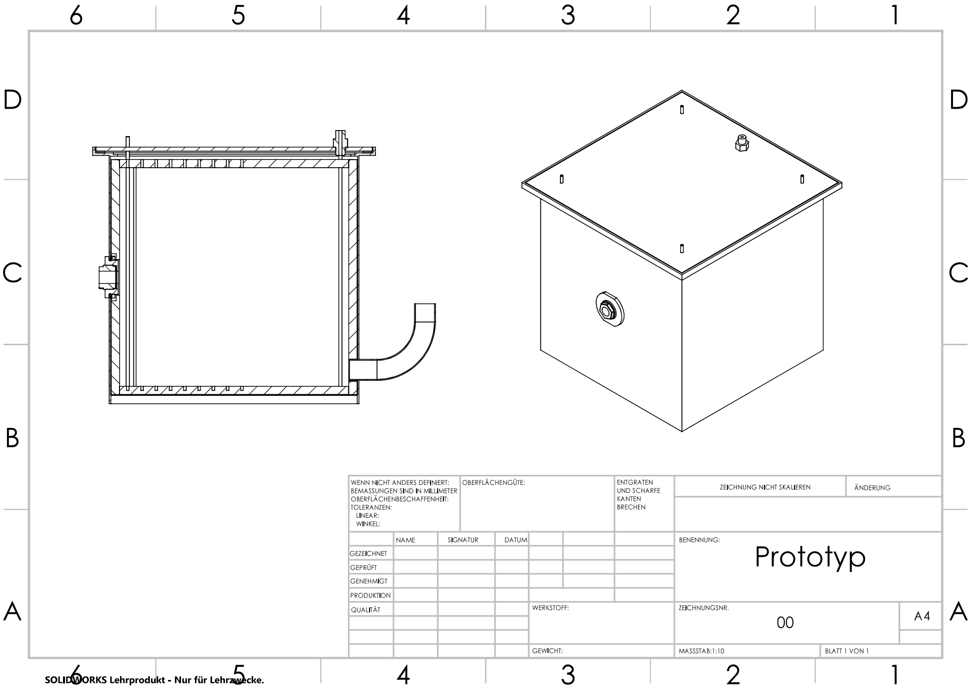

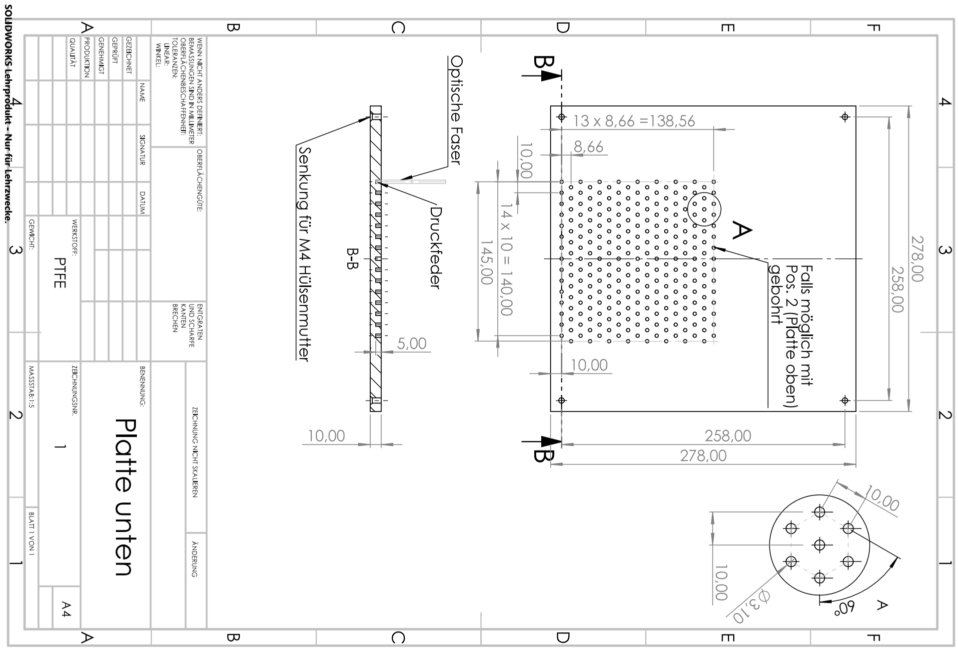

Figure A.2.: Page 2 and 3 of detector drawing by Fabian Piermaier

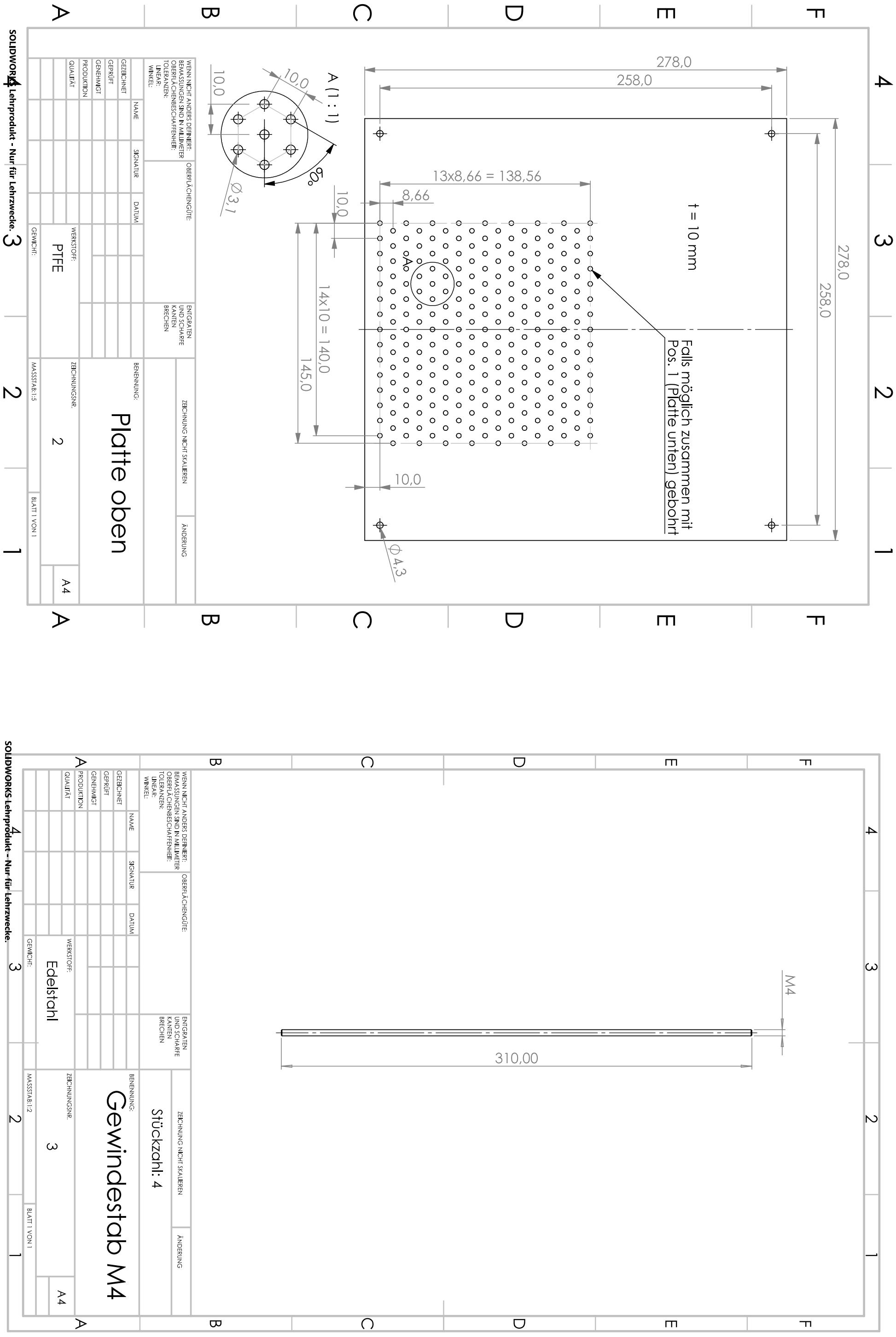

Figure A.3.: Page 4 and 5 of detector drawing by Fabian Piermaier

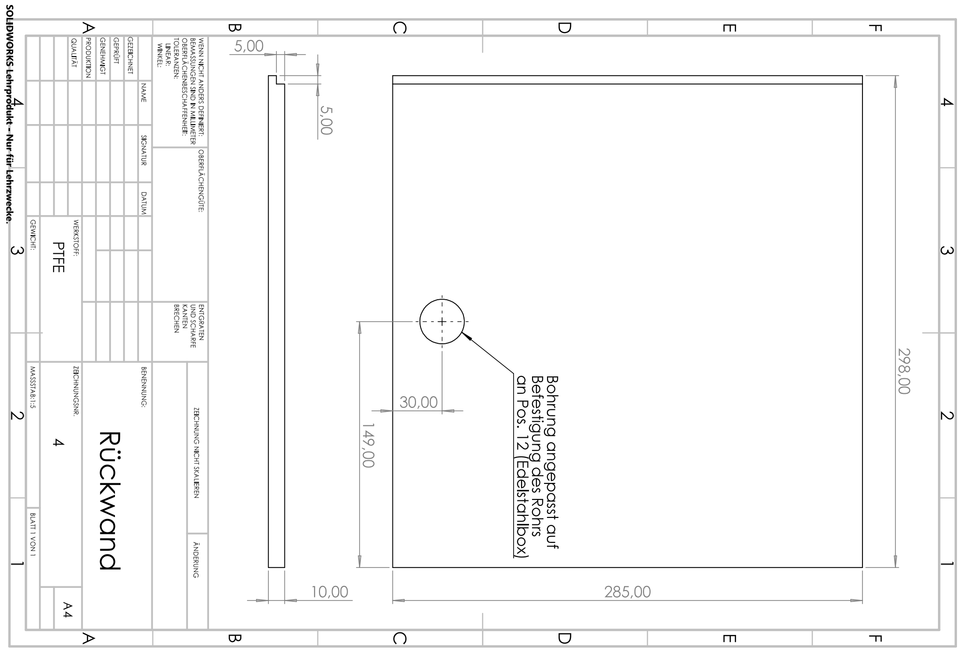

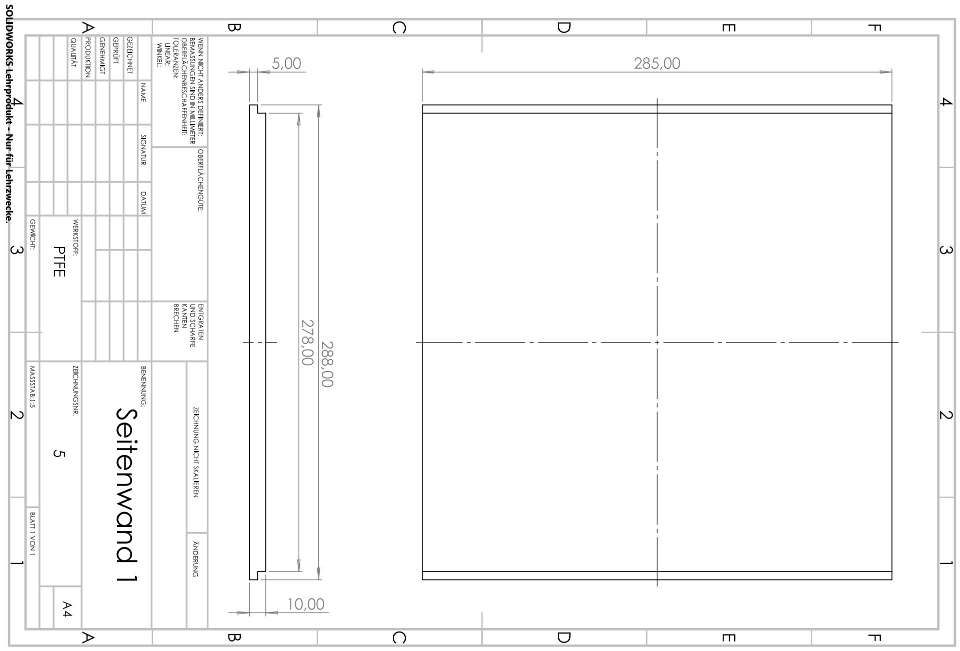

Figure A.4.: Page 6 and 7 of detector drawing by Fabian Piermaier

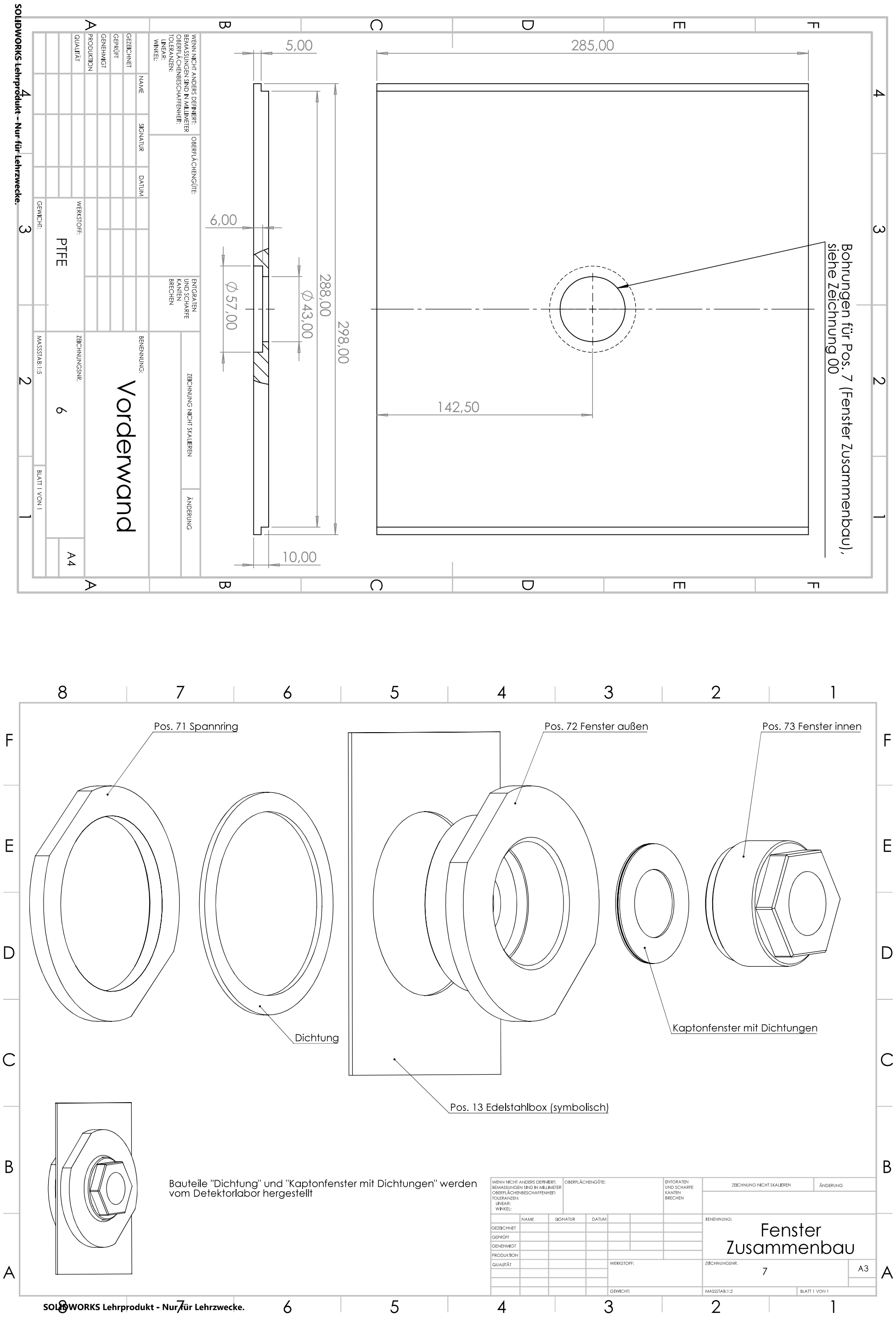

Figure A.5.: Page 8 and 9 of detector drawing by Fabian Piermaier

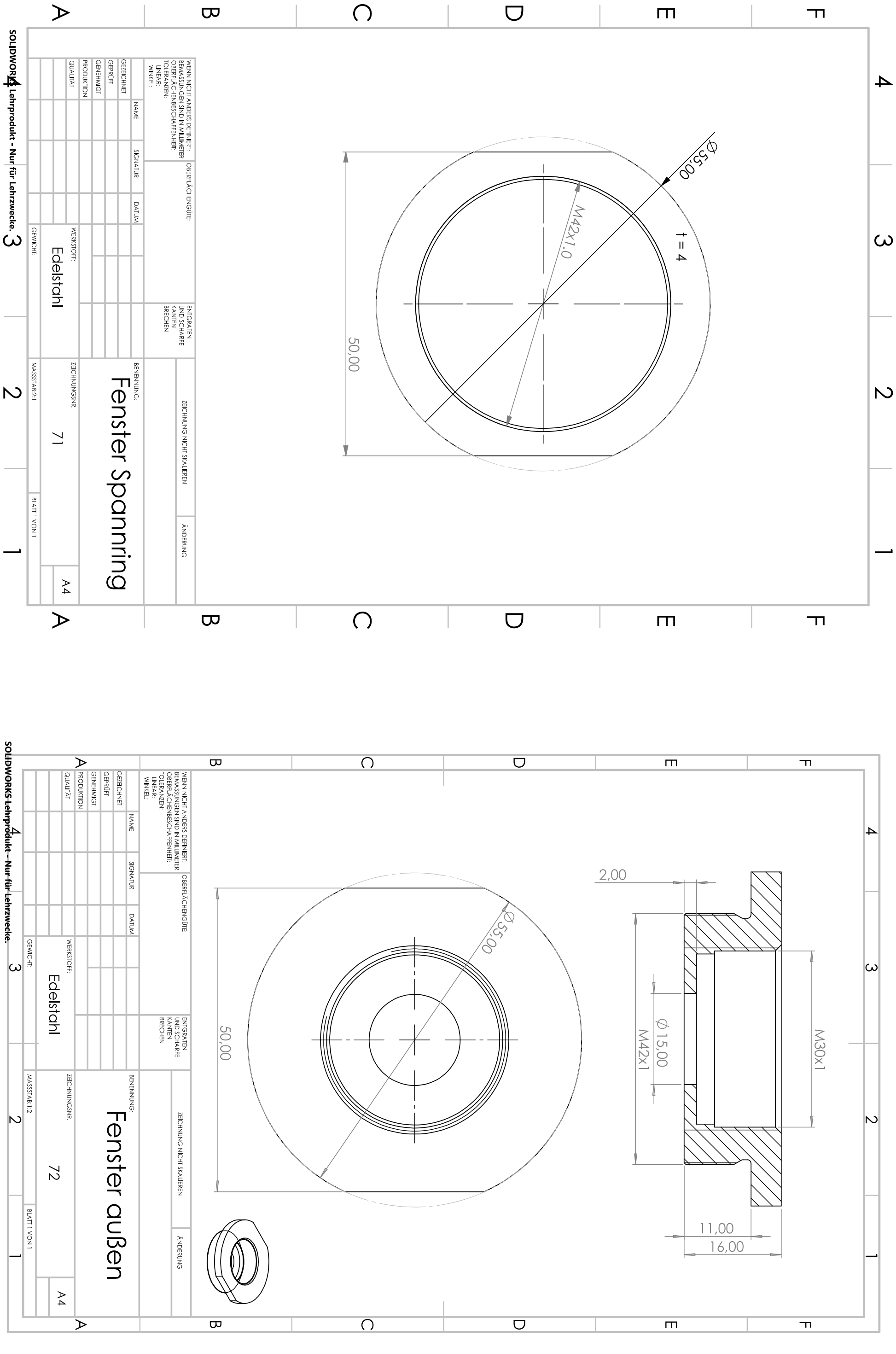

Figure A.6.: Page 10 and 11 of detector drawing by Fabian Piermaier

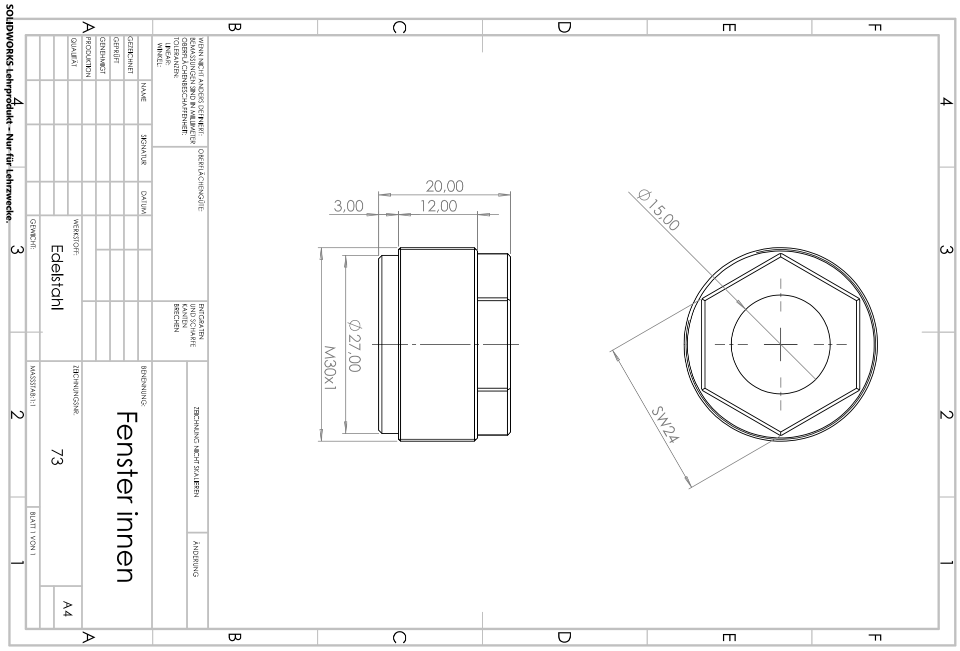

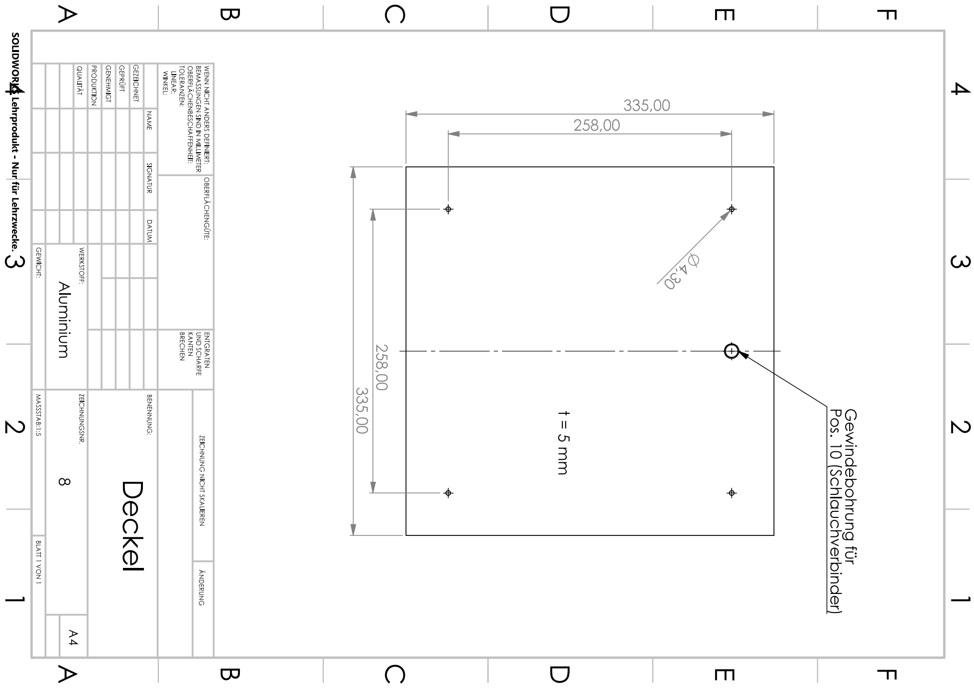

Figure A.7.: Page 12 and 13 of detector drawing by Fabian Piermaier

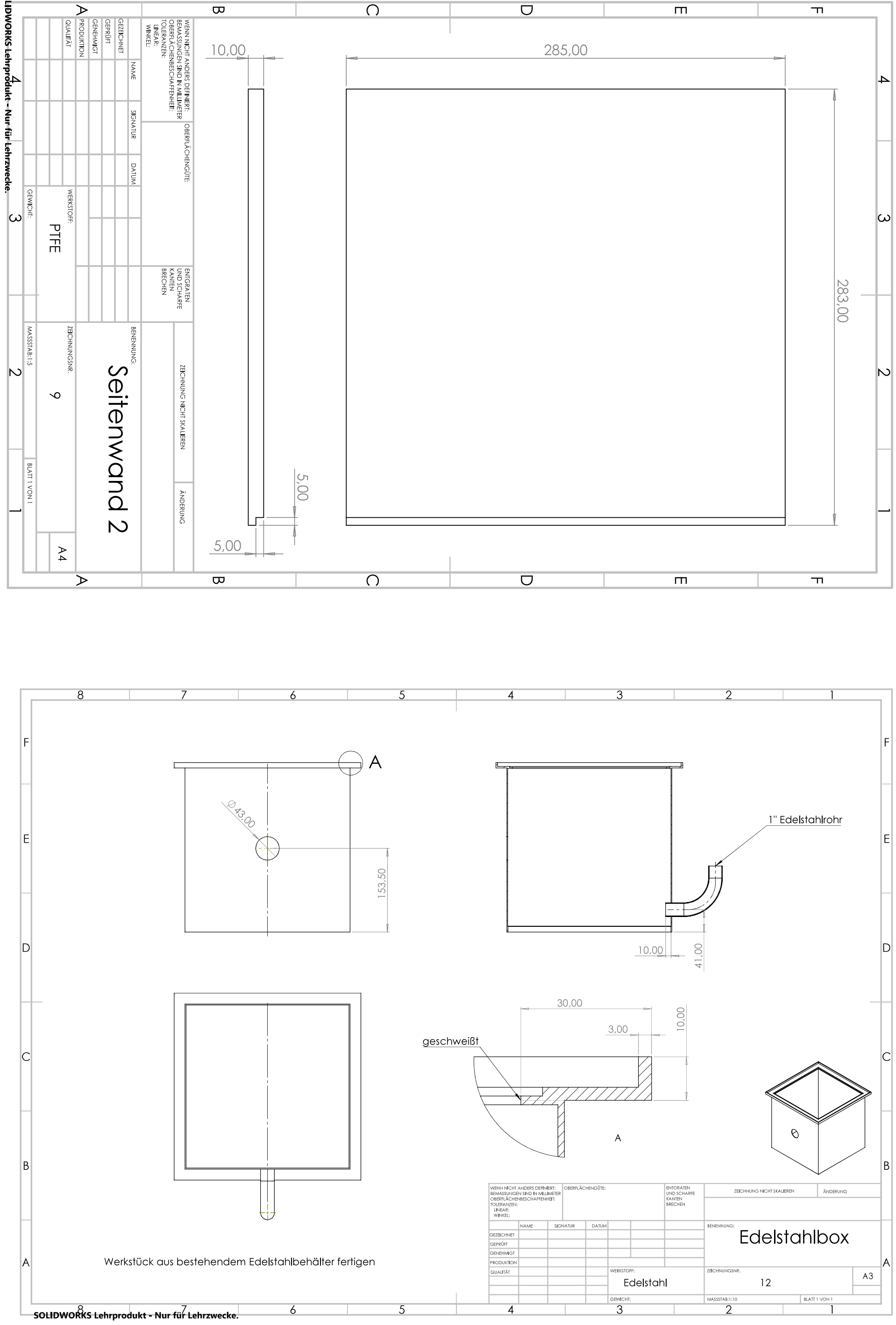

Figure A.8.: Page 14 and 15 of detector drawing by Fabian Piermaier

A.1.2. 3D printing resin

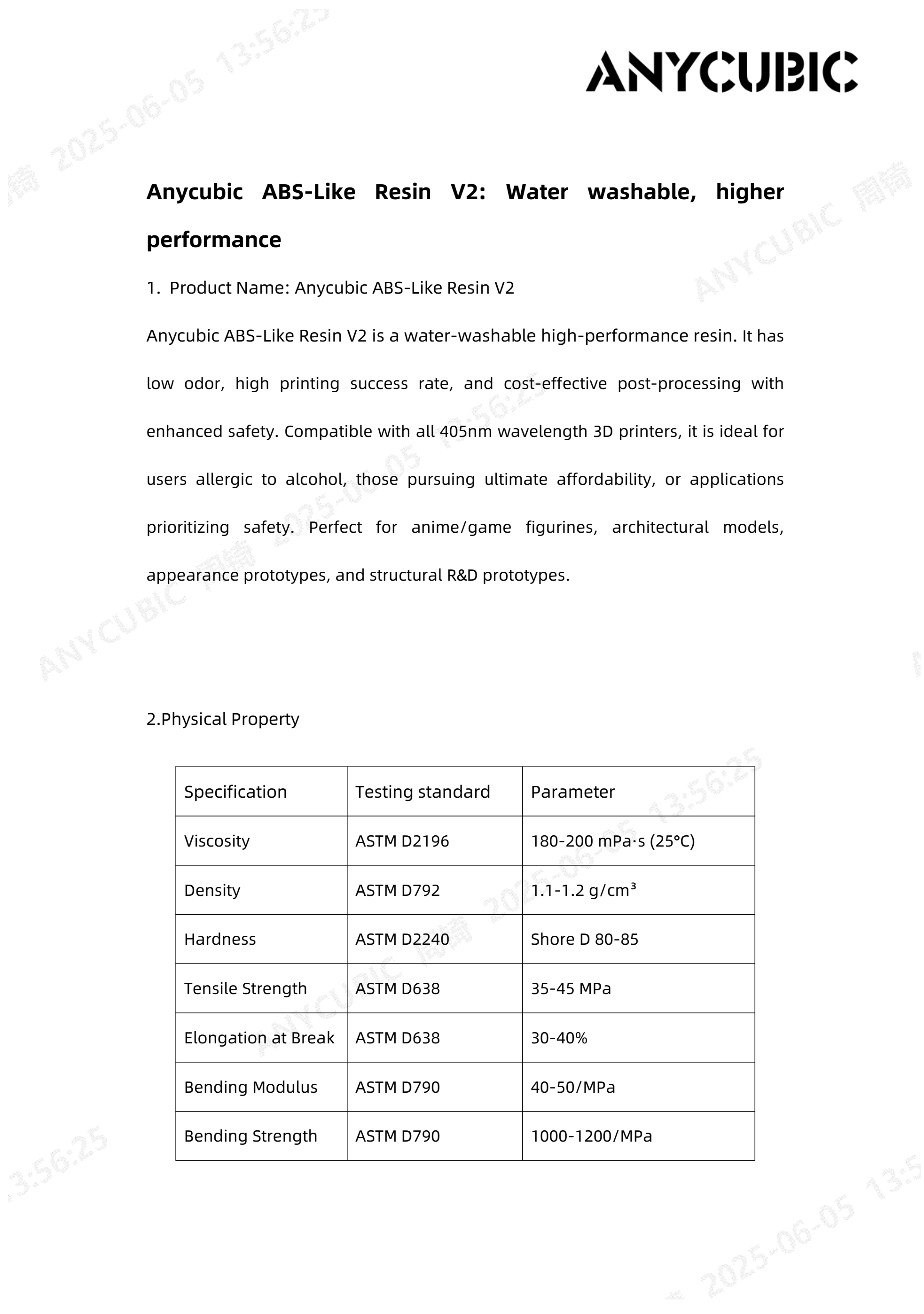

ANYCUBIC

Anycubic ABS-Like Resin V2: Water washable, higher performance

1. Product Name: Anycubic ABS-Like Resin V2

Anycubic ABS-Like Resin V2 is a water-washable high-performance resin. It has low odor, high printing success rate, and cost-effective post-processing with enhanced safety. Compatible with all 405nm wavelength 3D printers, it is ideal for users allergic to alcohol, those pursuing ultimate affordability, or applications prioritizing safety. Perfect for anime/game figurines, architectural models, appearance prototypes, and structural R&D prototypes.

2.Physical Property

Specification	Testing standard	Parameter
Viscosity	ASTM D2196	180-200 mPa·s (25°C)
Density	ASTM D792	1.1-1.2 g/cm³
Hardness	ASTM D2240	Shore D 80-85
Tensile Strength	ASTM D638	35-45 MPa
Elongation at Break	ASTM D638	30-40%
Bending Modulus	ASTM D790	40-50/MPa
Bending Strength	ASTM D790	1000-1200/MPa

Figure A.9.: Data sheet of the used Anycubic resin [33]

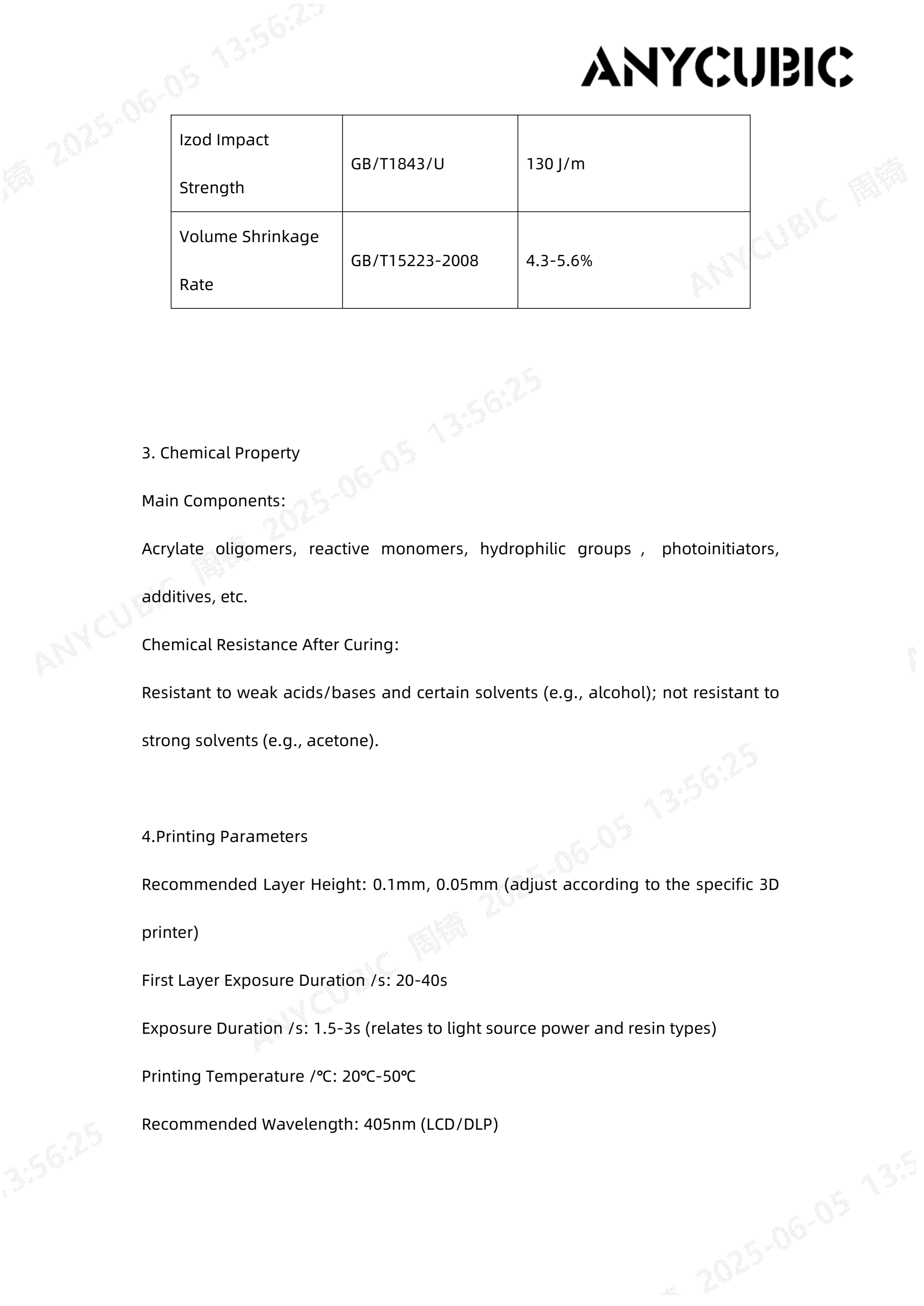

ANYCUBIC

Izod Impact Strength	GB/T1843/U	130 J/m
Volume Shrinkage Rate	GB/T15223-2008	4.3-5.6%

3. Chemical Property

Main Components:

Acrylate oligomers, reactive monomers, hydrophilic groups , photoinitiators, additives, etc.

Chemical Resistance After Curing:

Resistant to weak acids/bases and certain solvents (e.g., alcohol); not resistant to strong solvents (e.g., acetone).

4.Printing Parameters

Recommended Layer Height: 0.1mm, 0.05mm (adjust according to the specific 3D printer)

First Layer Exposure Duration /s: 20-40s

Exposure Duration /s: 1.5-3s (relates to light source power and resin types)

Printing Temperature /℃: 20℃-50℃

Recommended Wavelength: 405nm (LCD/DLP)

Figure A.10.: Data sheet of the used Anycubic resin [33]

ANYCUBIC

5.Post Processing

Washing Method: Wash with water, Ethanol, or Isopropyl Alcohol(IPA)

Wash Duration: ≥3 min (in wash & cure) / water wash ≥5 min

UV Curing Method: 3 minutes (in wash & cure)

Resin Disposal: Treated as plastic waste after curing

1.Do not discharge wastewater into drains to prevent groundwater contamination.

2.Allow the cleaned wastewater to settle in the sink for a period of time, then place it under sunlight to fully solidify the resin in the sink. Dispose of it as solid plastic waste to avoid environmental pollution.

6.Storage Condition

Temperature: 20-50°C (avoid extreme high/low temperatures)

Light Protection: Store in its factory container

Shelf Life: 18 months

7.Supplier Information

Manufacturer/Brand: ANYCUBIC

3.Technical Support: https://www.anycubic.com/

Figure A.11.: Data sheet of the used Anycubic resin [33]

ANYCUBIC

User Instructions

* Before use: Shake the resin thoroughly, clean the resin vat and build plate, ensure the vat's bottom remains highly transparent, and inspect the release film for any signs of damage.

* During use: Open the cap, remove the sealing film, pour the resin into the vat and ensure it does not exceed the max fill line.

* After use: Use proper tools for post-processing, including scrapers, flush cutters, tweezers, gloves, and IPA (≥95% concentration)

* Post-processing:

A: Remove the prints from the build plate using a scraper.

B: Wash prints, remove the support, and cure the prints.

C: Polish, paint, etc.

* Wastewater Disposal：

1. Do not discharge wastewater into drains to prevent groundwater contamination.

2. Allow the cleaned wastewater to settle in the sink for a period of time, then place it under sunlight to fully solidify the resin in the sink. Dispose of it as solid plastic waste to avoid environmental pollution.

Attention

1. Store in room temperatures and avoid direct sunlight.

Figure A.12.: Data sheet of the used Anycubic resin [33]

ANYCUBIC

2. We recommend a printing temperature above 20 ° C. Lower temperatures may negatively impact print success rates. Be cautious, as excessive temperature can lead to increased resin color settlement.

3. If sediment settles at the bottom of the resin vat, gently stir it with a plastic spatula or pour the resin back into its bottle and shake thoroughly to remix.

4. Uncured resin is highly light-sensitive and will cure in direct sunlight. For best results, print in a dark, well-ventilated area or keep the cover closed during printing.

5. Models made with water-washable resin are prone to absorbing moisture from the air, which may degrade performance or cause cracking. Please dry the models thoroughly (inside and out) and cure them promptly after printing.

6.Do not leave the uncured prints in the cleaning agent for a prolonged period, which may compromise the resin’s performance.

PS: The material performance may vary depending on the printer, method of curing, and testing instruments. Please refer to this product's safety information and certification reports (e.g., MSDS, REACH, RoHS, EAN, TDS). Should you encounter any issues, do not hesitate to contact us.

Figure A.13.: Data sheet of the used Anycubic resin [33]

A.2. Electronics

A.2.1. PCB layouts

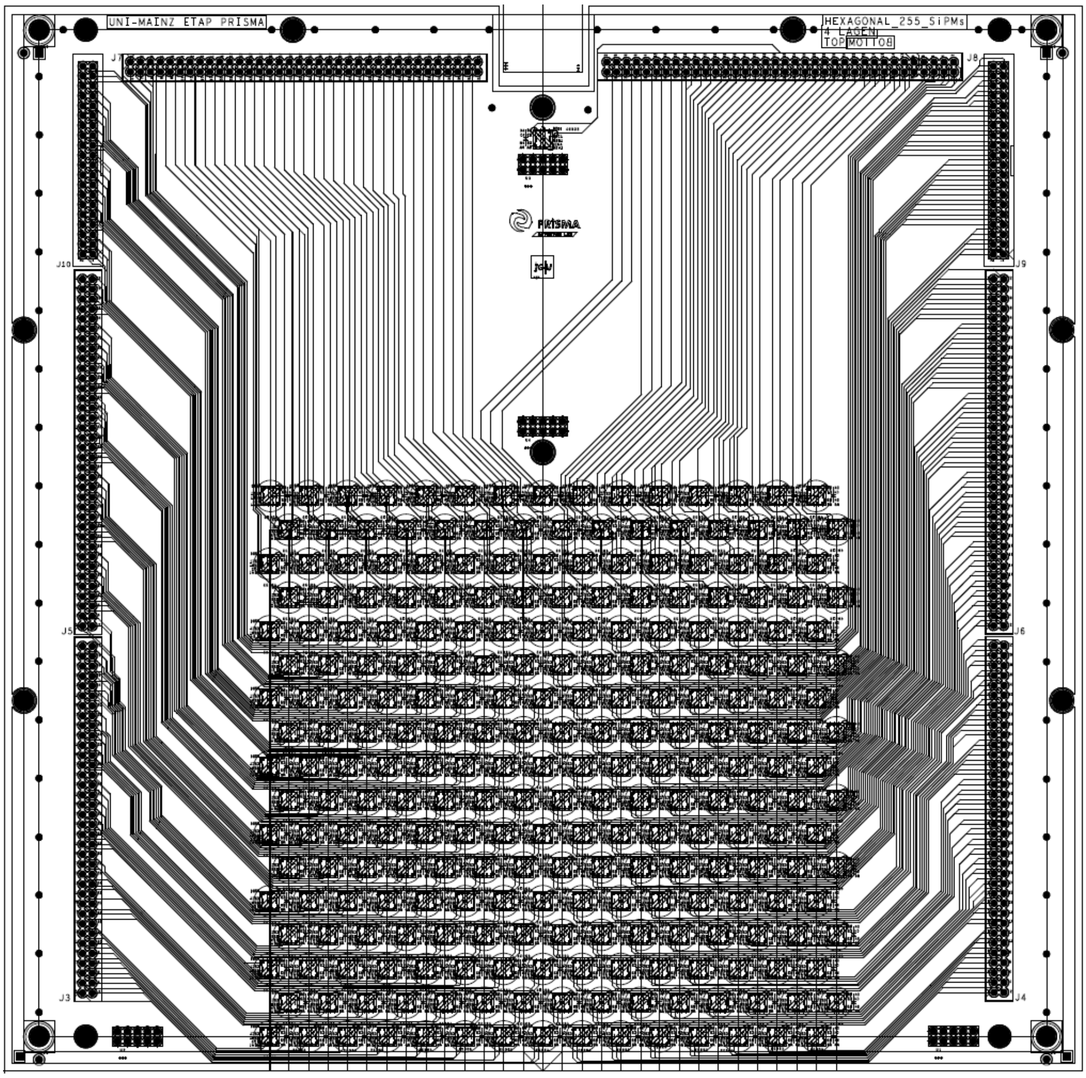

Figure A.14.: Connection scheme of the main PCB

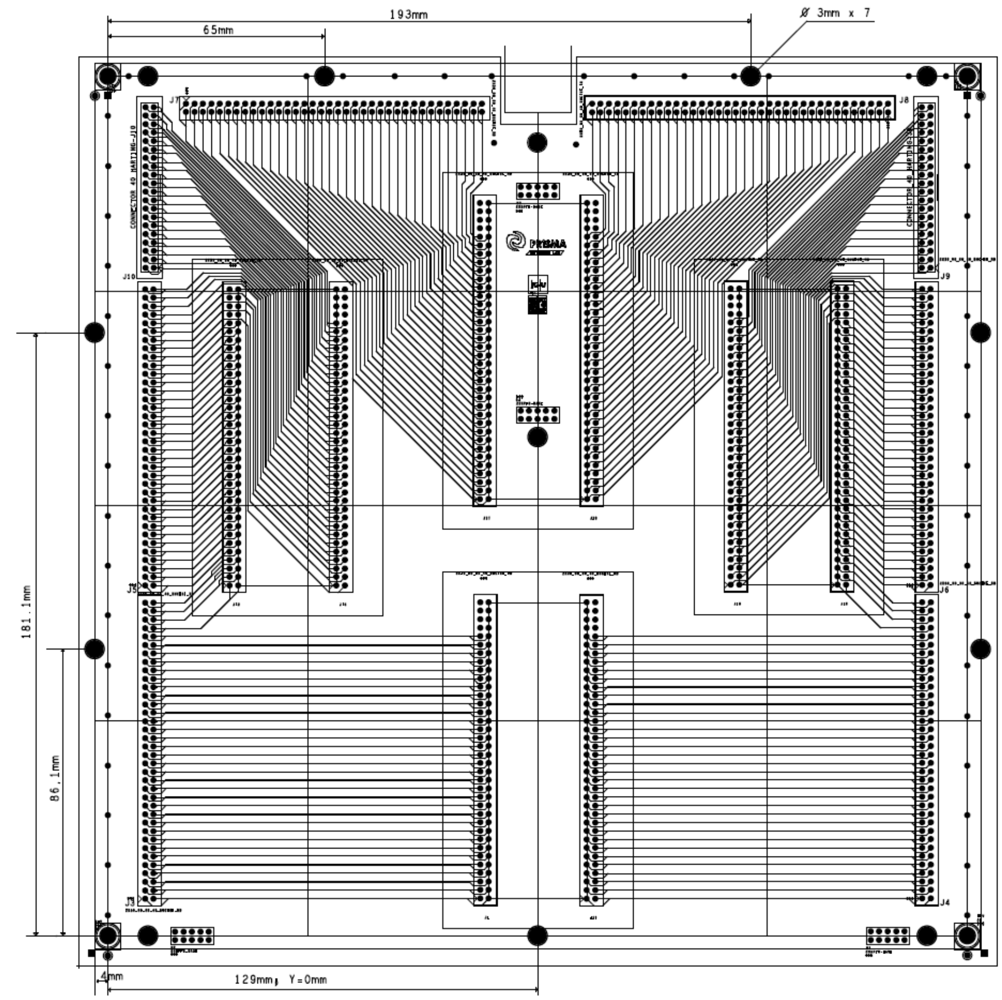

Figure A.15.: Connection scheme of the secondary signal routing PCB

A.2.2. CAEN FERS 5200

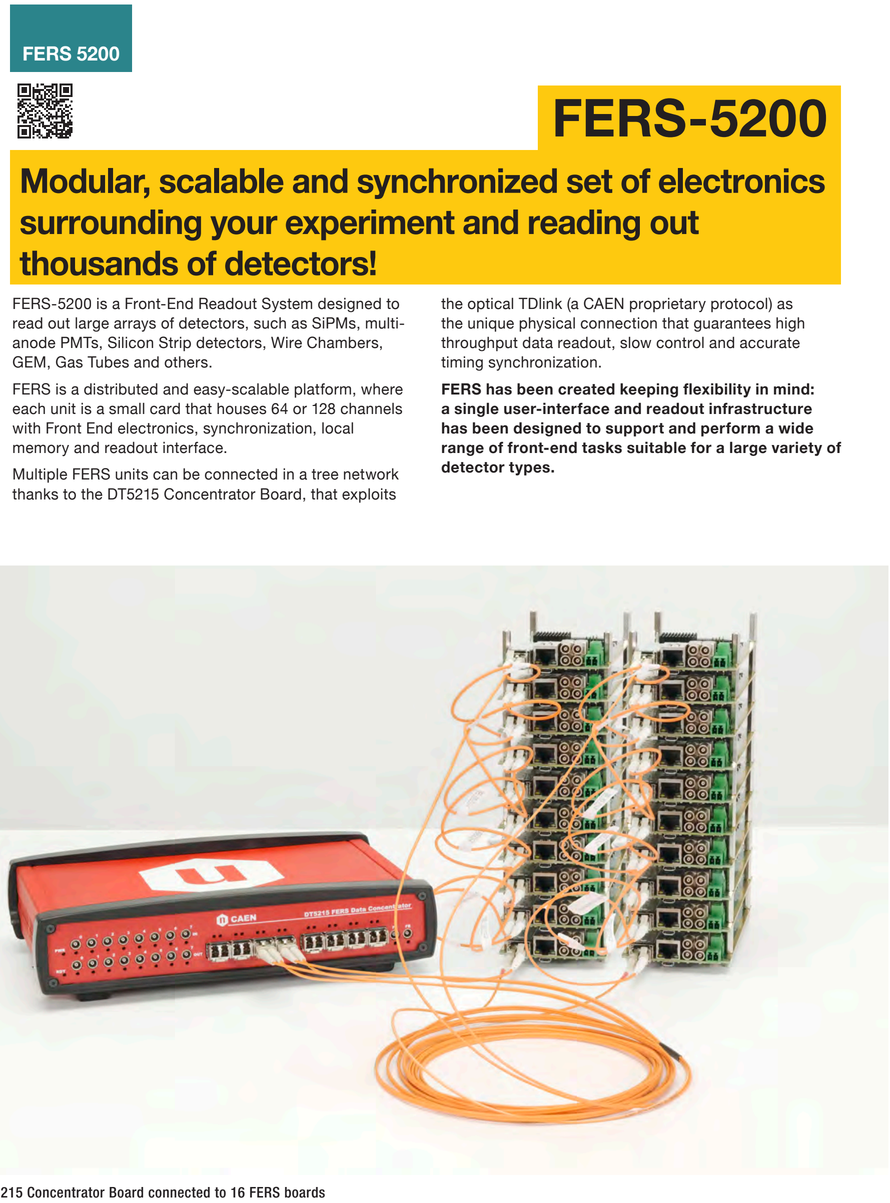

FERS 5200

FERS-5200

Modular, scalable and synchronized set of electronics surrounding your experiment and reading out thousands of detectors!

FERS-5200 is a Front-End Readout System designed to read out large arrays of detectors, such as SiPMs, multi-anode PMTs, Silicon Strip detectors, Wire Chambers, GEM, Gas Tubes and others.

FERS is a distributed and easy-scalable platform, where each unit is a small card that houses 64 or 128 channels with Front End electronics, synchronization, local memory and readout interface.

Multiple FERS units can be connected in a tree network thanks to the DT5215 Concentrator Board, that exploits the optical TDlink (a CAEN proprietary protocol) as the unique physical connection that guarantees high throughput data readout, slow control and accurate timing synchronization.

FERS has been created keeping flexibility in mind: a single user-interface and readout infrastructure has been designed to support and perform a wide range of front-end tasks suitable for a large variety of detector types.

DT5215 Concentrator Board connected to 16 FERS boards

Figure A.16.: Brochure of the CAEN FERS 5200 [34]

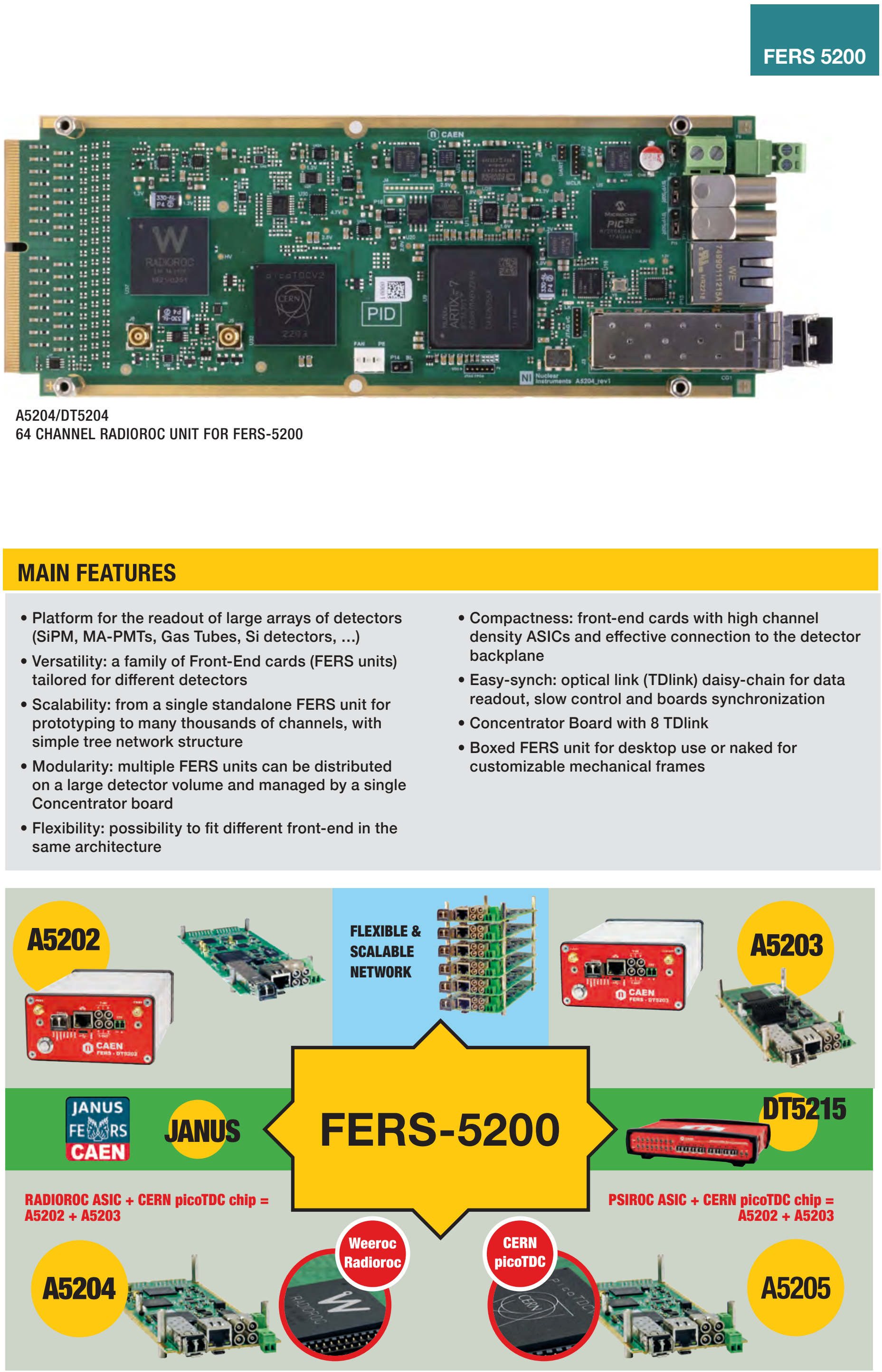

FERS 5200

A5204/DT5204
64 CHANNEL RADIOROC UNIT FOR FERS-5200

MAIN FEATURES

- Platform for the readout of large arrays of detectors (SiPM, MA-PMTs, Gas Tubes, Si detectors, ...)
- Versatility: a family of Front-End cards (FERS units) tailored for different detectors
- Scalability: from a single standalone FERS unit for prototyping to many thousands of channels, with simple tree network structure
- Modularity: multiple FERS units can be distributed on a large detector volume and managed by a single Concentrator board
- Flexibility: possibility to fit different front-end in the same architecture
- Compactness: front-end cards with high channel density ASICs and effective connection to the detector backplane
- Easy-synch: optical link (TDlink) daisy-chain for data readout, slow control and boards synchronization
- Concentrator Board with 8 TDlink
- Boxed FERS unit for desktop use or naked for customizable mechanical frames

A5202

FLEXIBLE & SCALABLE NETWORK

A5203

JANUS

FERS-5200

DT5215

RADIOROC ASIC + CERN picoTDC chip = A5202 + A5203

PSIROC ASIC + CERN picoTDC chip = A5202 + A5203

Weeroc Radioroc

CERN picoTDC

A5204

A5205

Figure A.17.: Brochure of the CAEN FERS 5200 [34]

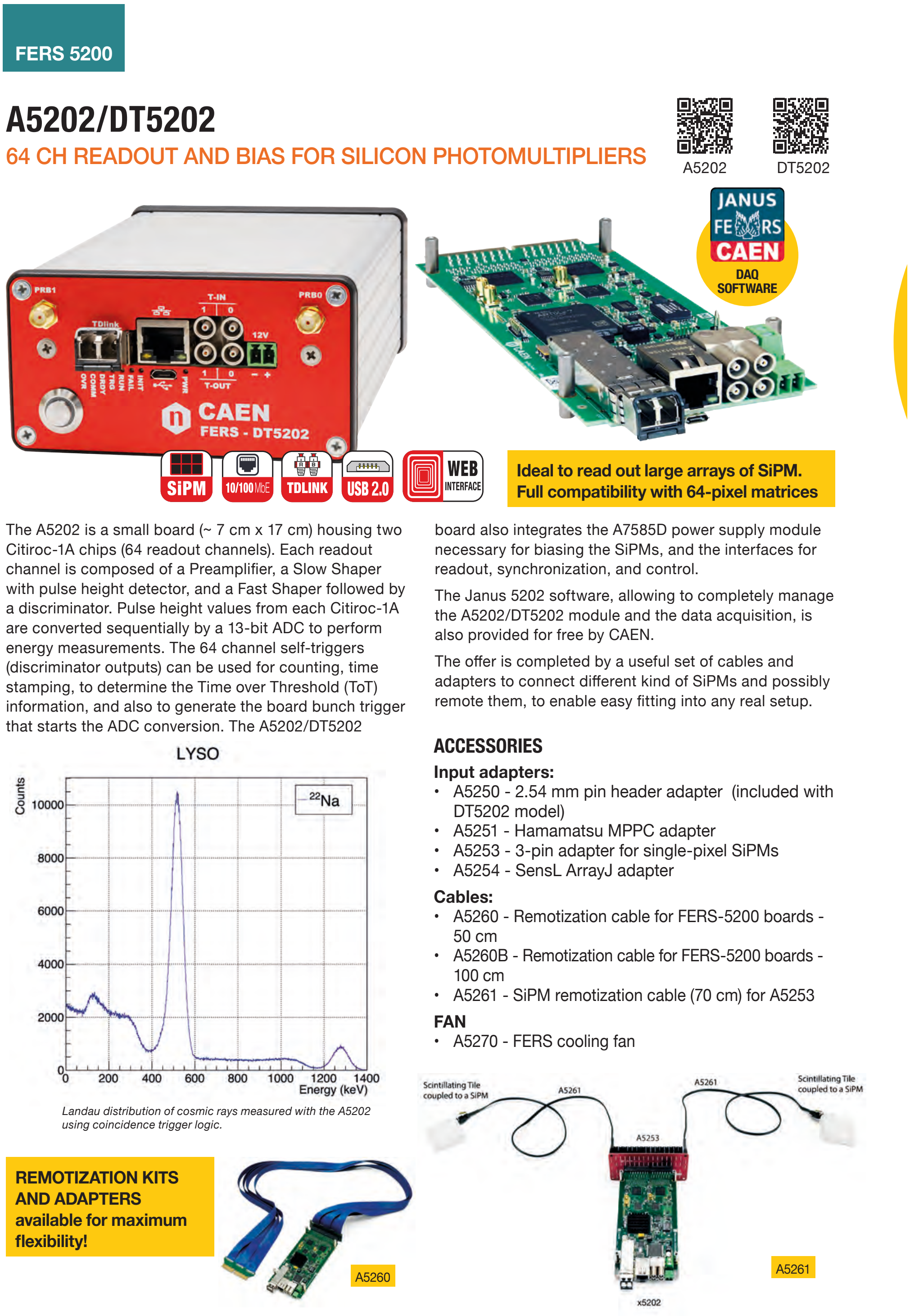

FERS 5200

A5202/DT5202

64 CH READOUT AND BIAS FOR SILICON PHOTOMULTIPLIERS

A5202 DT5202

JANUS FERS CAEN DAQ SOFTWARE

SiPM 10/100 MbE TDLINK USB 2.0 WEB INTERFACE

Ideal to read out large arrays of SiPM.
Full compatibility with 64-pixel matrices

The A5202 is a small board (~ 7 cm x 17 cm) housing two Citiroc-1A chips (64 readout channels). Each readout channel is composed of a Preamplifier, a Slow Shaper with pulse height detector, and a Fast Shaper followed by a discriminator. Pulse height values from each Citiroc-1A are converted sequentially by a 13-bit ADC to perform energy measurements. The 64 channel self-triggers (discriminator outputs) can be used for counting, time stamping, to determine the Time over Threshold (ToT) information, and also to generate the board bunch trigger that starts the ADC conversion. The A5202/DT5202 board also integrates the A7585D power supply module necessary for biasing the SiPMs, and the interfaces for readout, synchronization, and control.

The Janus 5202 software, allowing to completely manage the A5202/DT5202 module and the data acquisition, is also provided for free by CAEN.

The offer is completed by a useful set of cables and adapters to connect different kind of SiPMs and possibly remote them, to enable easy fitting into any real setup.

Landau distribution of cosmic rays measured with the A5202 using coincidence trigger logic.

ACCESSORIES

Input adapters:

- A5250 - 2.54 mm pin header adapter (included with DT5202 model)
- A5251 - Hamamatsu MPPC adapter
- A5253 - 3-pin adapter for single-pixel SiPMs
- A5254 - SensL ArrayJ adapter

Cables:

- A5260 - Remotization cable for FERS-5200 boards - 50 cm
- A5260B - Remotization cable for FERS-5200 boards - 100 cm
- A5261 - SiPM remotization cable (70 cm) for A5253

FAN

- A5270 - FERS cooling fan

REMOTIZATION KITS AND ADAPTERS available for maximum flexibility!

Figure A.18.: Brochure of the CAEN FERS 5200 [34]

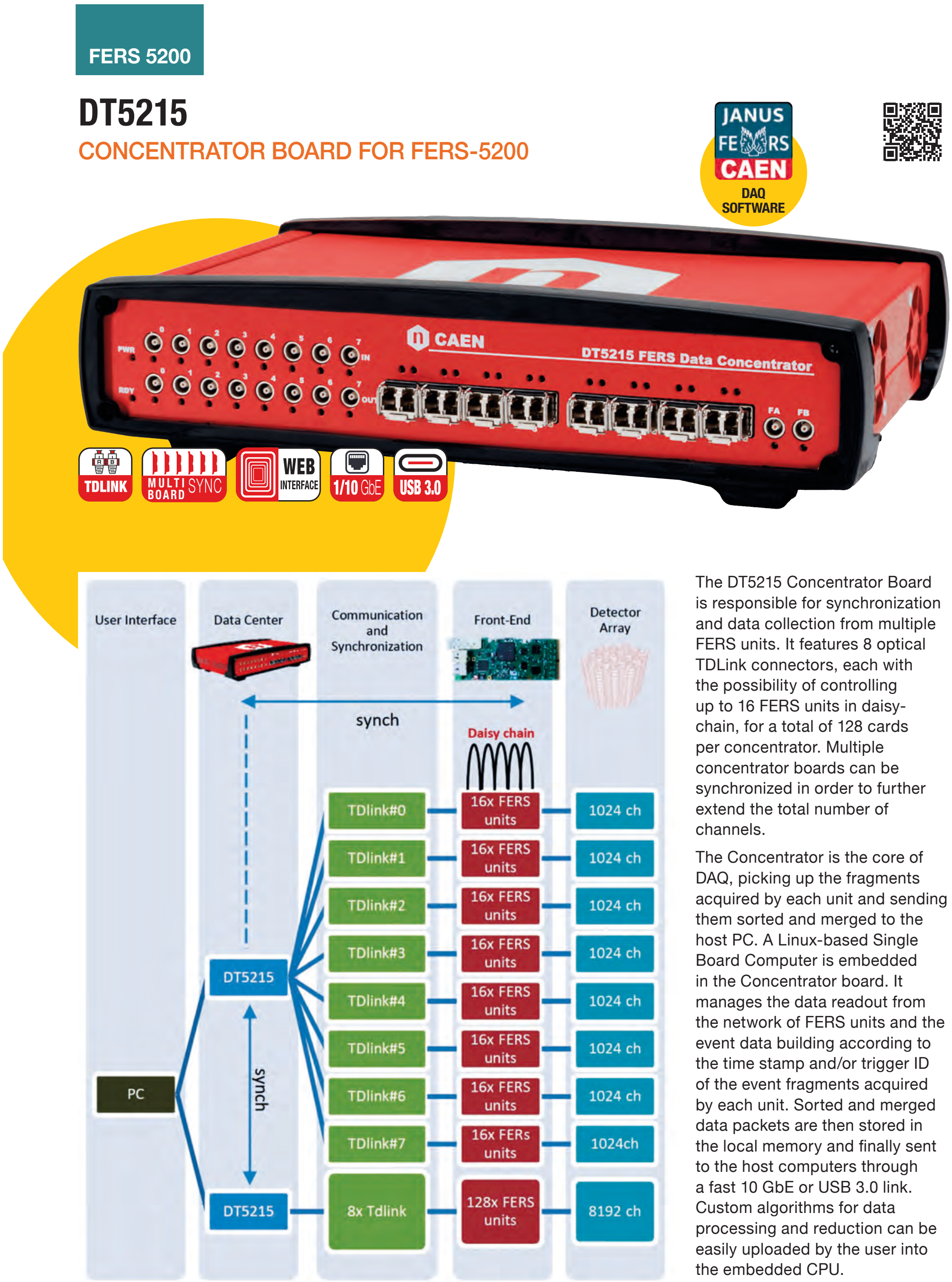

DT5215

CONCENTRATOR BOARD FOR FERS-5200

The DT5215 Concentrator Board is responsible for synchronization and data collection from multiple FERS units. It features 8 optical TDLink connectors, each with the possibility of controlling up to 16 FERS units in daisy-chain, for a total of 128 cards per concentrator. Multiple concentrator boards can be synchronized in order to further extend the total number of channels.

The Concentrator is the core of DAQ, picking up the fragments acquired by each unit and sending them sorted and merged to the host PC. A Linux-based Single Board Computer is embedded in the Concentrator board. It manages the data readout from the network of FERS units and the event data building according to the time stamp and/or trigger ID of the event fragments acquired by each unit. Sorted and merged data packets are then stored in the local memory and finally sent to the host computers through a fast 10 GbE or USB 3.0 link. Custom algorithms for data processing and reduction can be easily uploaded by the user into the embedded CPU.

Figure A.19.: Brochure of the CAEN FERS 5200 [34]

FERS 5200

JANUS

FERS-5200 DAQ SOFTWARE

A single DAQ software to control the FERS-5200 board family. Available in Console and GUI Mode, it allows the user to customize the DAQ, and offers an easy way to approach multi-boards and high-channel density FERS-5200 systems.

Janus is an open source software for the control and readout of FERS-5200 boards. Available in two versions (Ver. 5202, Ver. 5203), it can be used as a platform for the development of custom DAQ, tailored to the specific application. Indeed, the user can change the data treatment, the acquired statistics and the output file format.

Janus can manage up to 16 FERS units connected via Ethernet or USB directly as well as the readout of the DT5215 Concentrator Board, so that a single user interface is available for the whole system.

Janus is composed of two parts, one written in C, which is the real heart of the application, one written in Python which manages the user interface. The plots are executed through Gnuplot. All the configuration parameters are written in a textual configuration file.

It is possible to launch and use Janus in 2 different modes:

- **Console Mode.** In this case, the Python part of the software is not used. The user can edit the configuration file with any text editor and save the proper values for the desired parameters. Then, the user can launch a purely textual console window. The application writes a series of messages (which are also saved in a log file) and, during the run, prints statistics on the screen. The only graphical part is the plot, which is managed by Gnuplot.
- **GUI Mode**: In this case, the user only have to run the Python program which calls the C program and connects to it via a socket to send commands and receive messages which are then displayed in the Python GUI.

Features

- Model-dependent GUI for a quick and easy start
- Open-Source for user customization
- Management of the acquisition parameters of all connected boards
- Multi parametric Jobs and Runs with time or counts preset
- Data saving of lists in .bin, .txt format
- Statistics and Plots visualization

Figure A.20.: Brochure of the CAEN FERS 5200 [34]

A.2.3. SiPM data sheets

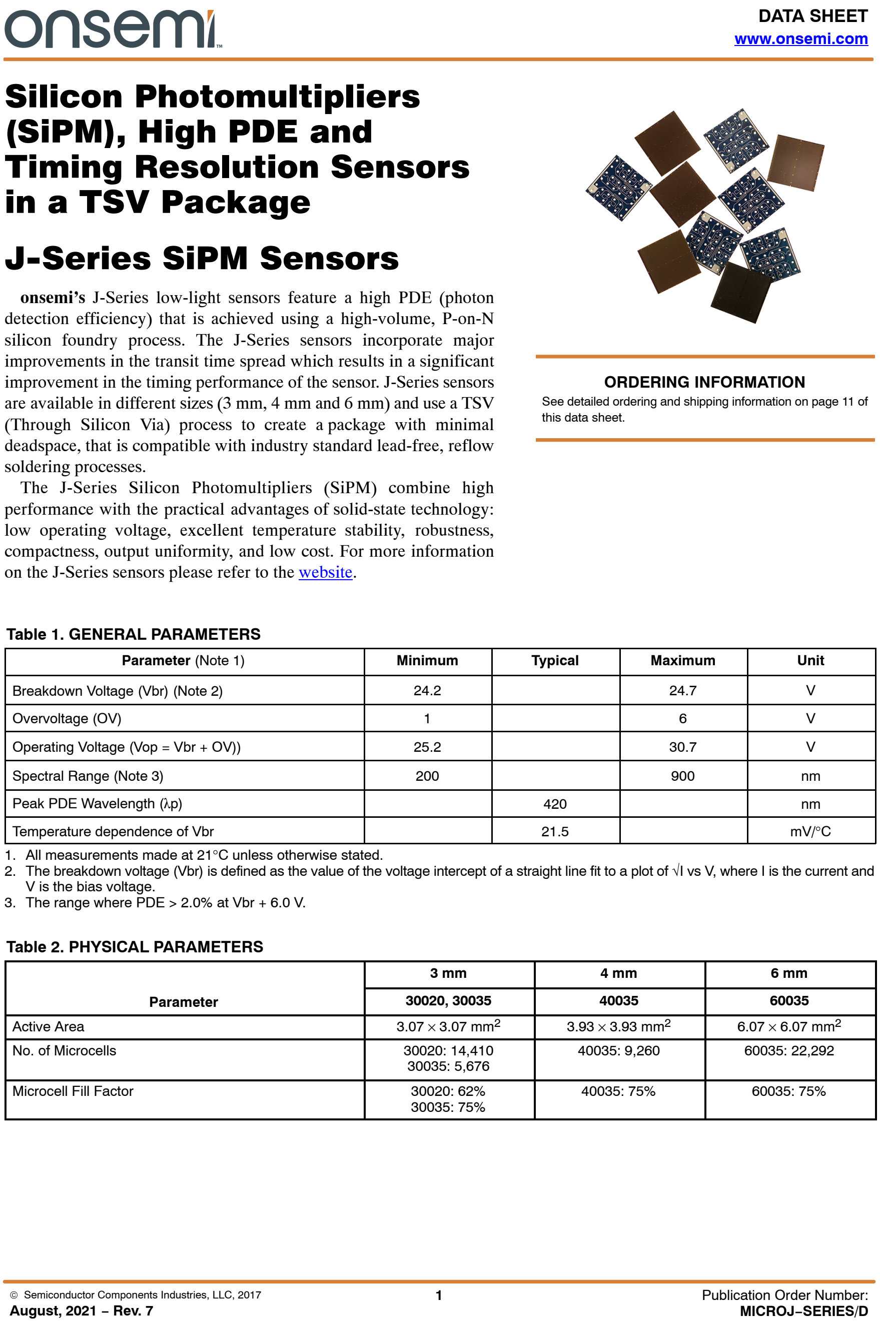

DATA SHEET
www.onsemi.com

Silicon Photomultipliers (SiPM), High PDE and Timing Resolution Sensors in a TSV Package

J-Series SiPM Sensors

onsemi’s J-Series low-light sensors feature a high PDE (photon detection efficiency) that is achieved using a high-volume, P-on-N silicon foundry process. The J-Series sensors incorporate major improvements in the transit time spread which results in a significant improvement in the timing performance of the sensor. J-Series sensors are available in different sizes (3 mm, 4 mm and 6 mm) and use a TSV (Through Silicon Via) process to create a package with minimal deadspace, that is compatible with industry standard lead-free, reflow soldering processes.

The J-Series Silicon Photomultipliers (SiPM) combine high performance with the practical advantages of solid-state technology: low operating voltage, excellent temperature stability, robustness, compactness, output uniformity, and low cost. For more information on the J-Series sensors please refer to the website.

ORDERING INFORMATION
See detailed ordering and shipping information on page 11 of this data sheet.

Table 1. GENERAL PARAMETERS

Parameter (Note 1)	**Minimum**	**Typical**	**Maximum**	**Unit**
Breakdown Voltage (Vbr) (Note 2)	24.2		24.7	V
Overvoltage (OV)	1		6	V
Operating Voltage (Vop = Vbr + OV))	25.2		30.7	V
Spectral Range (Note 3)	200		900	nm
Peak PDE Wavelength (λp)		420		nm
Temperature dependence of Vbr		21.5		mV/°C

1. All measurements made at 21°C unless otherwise stated.
2. The breakdown voltage (Vbr) is defined as the value of the voltage intercept of a straight line fit to a plot of √I vs V, where I is the current and V is the bias voltage.
3. The range where PDE > 2.0% at Vbr + 6.0 V.

Table 2. PHYSICAL PARAMETERS

	3 mm	**4 mm**	**6 mm**
Parameter	**30020, 30035**	**40035**	**60035**
Active Area	3.07×3.07 mm^2	3.93×3.93 mm^2	6.07×6.07 mm^2
No. of Microcells	30020: 14,410 30035: 5,676	40035: 9,260	60035: 22,292
Microcell Fill Factor	30020: 62% 30035: 75%	40035: 75%	60035: 75%

© Semiconductor Components Industries, LLC, 2017
August, 2021 − Rev. 7
1
Publication Order Number:
MICROJ−SERIES/D

Figure A.21.: SiPM data sheet [35]

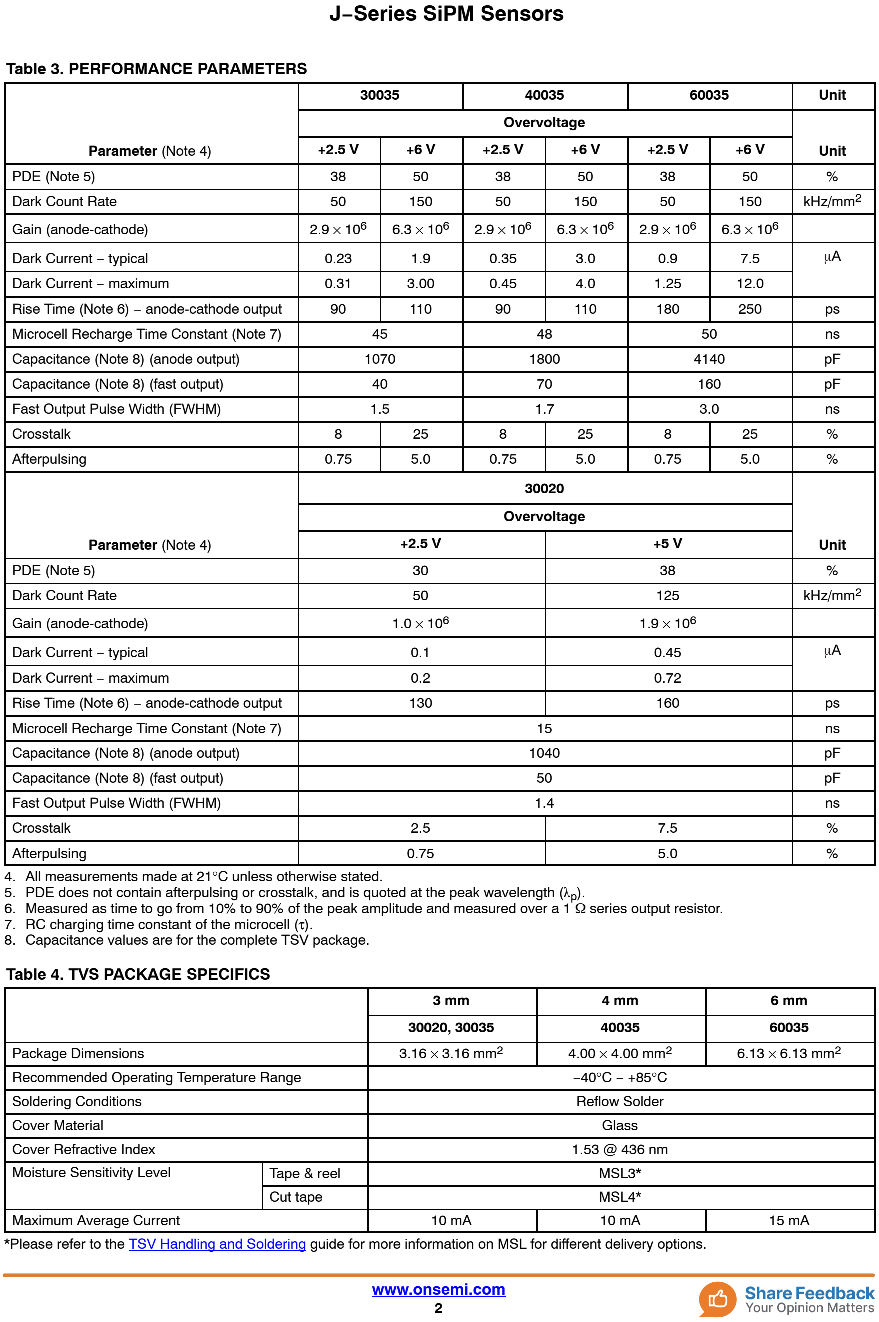

J–Series SiPM Sensors

Table 3. PERFORMANCE PARAMETERS

	30035		**40035**		**60035**		**Unit**
	Overvoltage						
Parameter (Note 4)	**+2.5 V**	**+6 V**	**+2.5 V**	**+6 V**	**+2.5 V**	**+6 V**	**Unit**
PDE (Note 5)	38	50	38	50	38	50	%
Dark Count Rate	50	150	50	150	50	150	kHz/mm^2
Gain (anode-cathode)	2.9×10^6	6.3×10^6	2.9×10^6	6.3×10^6	2.9×10^6	6.3×10^6	
Dark Current – typical	0.23	1.9	0.35	3.0	0.9	7.5	μA
Dark Current – maximum	0.31	3.00	0.45	4.0	1.25	12.0	
Rise Time (Note 6) – anode-cathode output	90	110	90	110	180	250	ps
Microcell Recharge Time Constant (Note 7)	45		48		50		ns
Capacitance (Note 8) (anode output)	1070		1800		4140		pF
Capacitance (Note 8) (fast output)	40		70		160		pF
Fast Output Pulse Width (FWHM)	1.5		1.7		3.0		ns
Crosstalk	8	25	8	25	8	25	%
Afterpulsing	0.75	5.0	0.75	5.0	0.75	5.0	%

	30020		
	Overvoltage		
Parameter (Note 4)	**+2.5 V**	**+5 V**	**Unit**
PDE (Note 5)	30	38	%
Dark Count Rate	50	125	kHz/mm^2
Gain (anode-cathode)	1.0×10^6	1.9×10^6	
Dark Current – typical	0.1	0.45	μA
Dark Current – maximum	0.2	0.72	
Rise Time (Note 6) – anode-cathode output	130	160	ps
Microcell Recharge Time Constant (Note 7)	15		ns
Capacitance (Note 8) (anode output)	1040		pF
Capacitance (Note 8) (fast output)	50		pF
Fast Output Pulse Width (FWHM)	1.4		ns
Crosstalk	2.5	7.5	%
Afterpulsing	0.75	5.0	%

4. All measurements made at 21°C unless otherwise stated.
5. PDE does not contain afterpulsing or crosstalk, and is quoted at the peak wavelength (λ_p).
6. Measured as time to go from 10% to 90% of the peak amplitude and measured over a 1 Ω series output resistor.
7. RC charging time constant of the microcell (τ).
8. Capacitance values are for the complete TSV package.

Table 4. TVS PACKAGE SPECIFICS

		3 mm	**4 mm**	**6 mm**
		30020, 30035	**40035**	**60035**
Package Dimensions		3.16×3.16 mm^2	4.00×4.00 mm^2	6.13×6.13 mm^2
Recommended Operating Temperature Range		–40°C – +85°C		
Soldering Conditions		Reflow Solder		
Cover Material		Glass		
Cover Refractive Index		1.53 @ 436 nm		
Moisture Sensitivity Level	Tape & reel	MSL3*		
	Cut tape	MSL4*		
Maximum Average Current		10 mA	10 mA	15 mA

*Please refer to the TSV Handling and Soldering guide for more information on MSL for different delivery options.

www.onsemi.com
2

Share Feedback
Your Opinion Matters

Figure A.22.: SiPM data sheet [35]

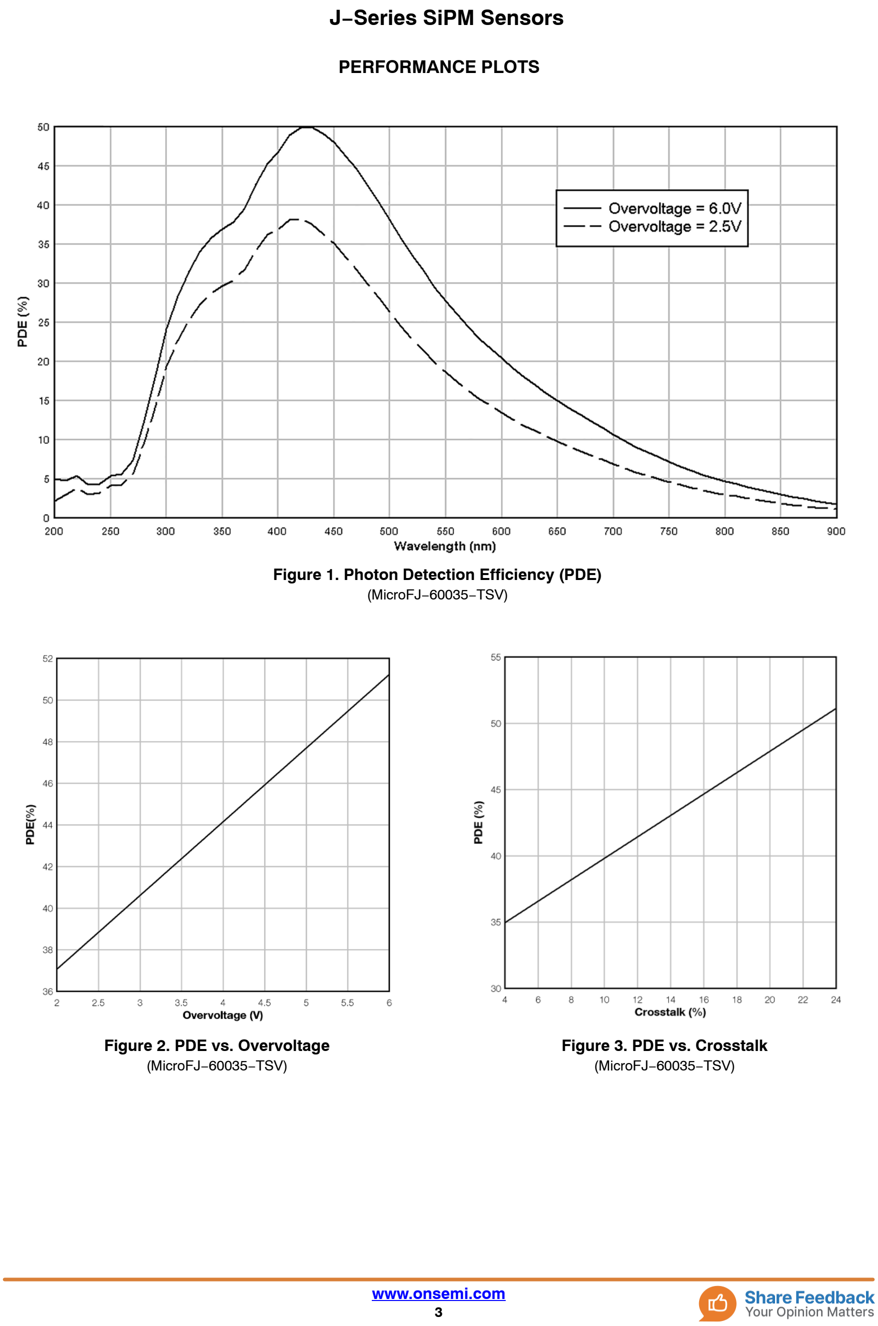

J–Series SiPM Sensors

PERFORMANCE PLOTS

Figure 1. Photon Detection Efficiency (PDE)
(MicroFJ–60035–TSV)

Figure 2. PDE vs. Overvoltage
(MicroFJ–60035–TSV)

Figure 3. PDE vs. Crosstalk
(MicroFJ–60035–TSV)

www.onsemi.com
3

Share Feedback
Your Opinion Matters

Figure A.23.: SiPM data sheet [35]

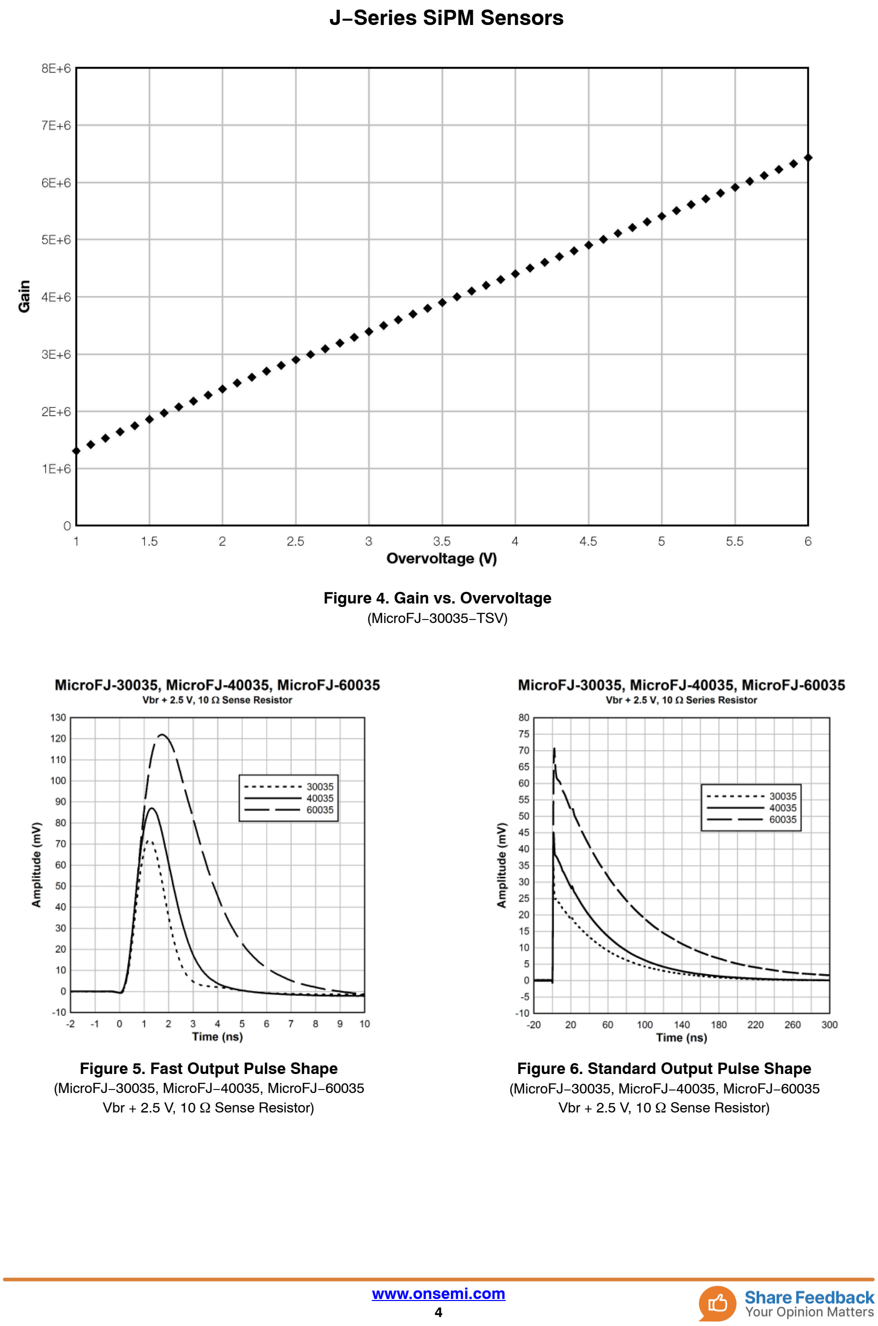

J–Series SiPM Sensors

Figure 4. Gain vs. Overvoltage
(MicroFJ−30035−TSV)

Figure 5. Fast Output Pulse Shape
(MicroFJ−30035, MicroFJ−40035, MicroFJ−60035
Vbr + 2.5 V, 10 Ω Sense Resistor)

Figure 6. Standard Output Pulse Shape
(MicroFJ−30035, MicroFJ−40035, MicroFJ−60035
Vbr + 2.5 V, 10 Ω Sense Resistor)

www.onsemi.com
4

Figure A.24.: SiPM data sheet [35]

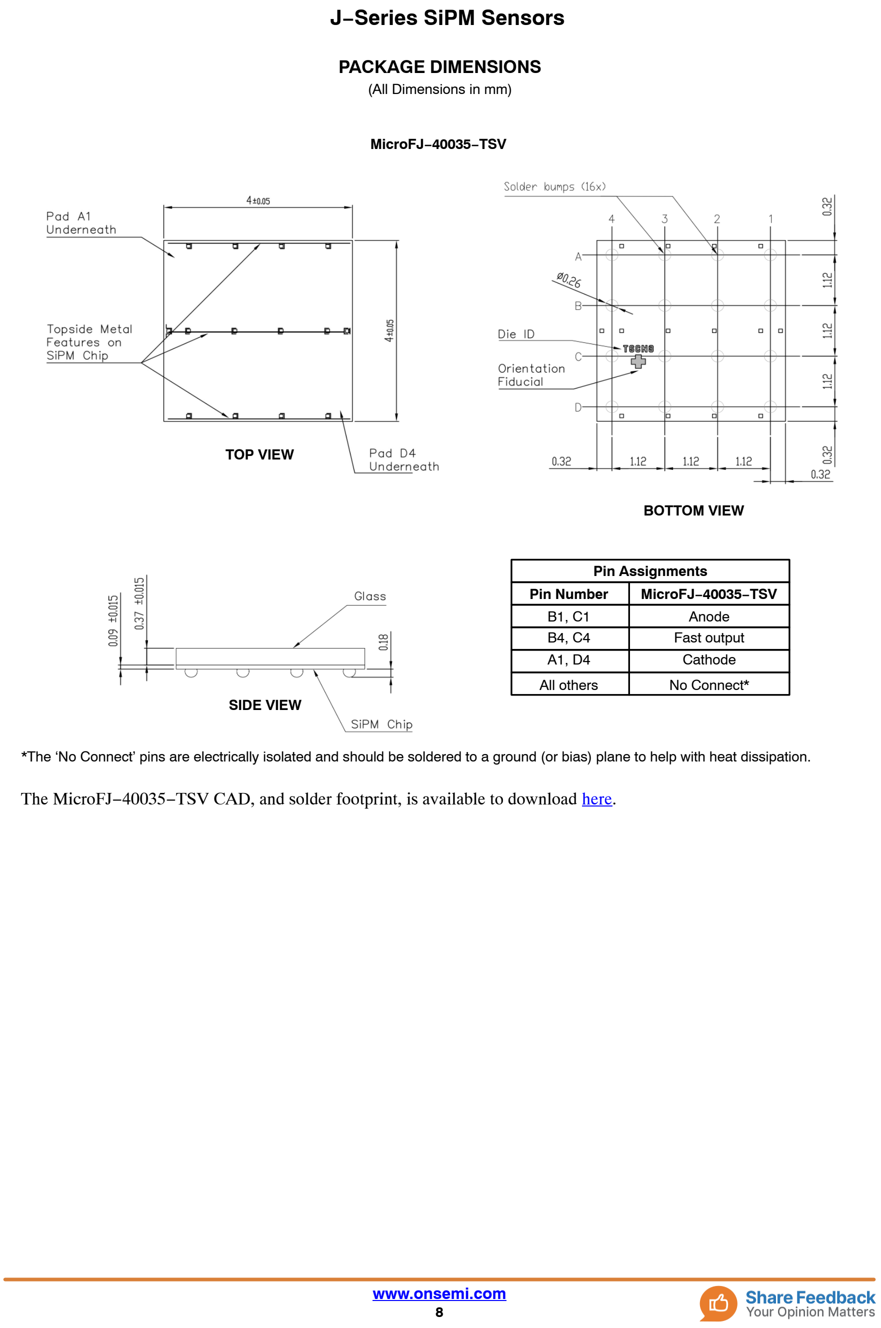

J–Series SiPM Sensors

PACKAGE DIMENSIONS

(All Dimensions in mm)

MicroFJ–40035–TSV

Pin Assignments	
Pin Number	**MicroFJ–40035–TSV**
B1, C1	Anode
B4, C4	Fast output
A1, D4	Cathode
All others	No Connect*

*The ‘No Connect’ pins are electrically isolated and should be soldered to a ground (or bias) plane to help with heat dissipation.

The MicroFJ–40035–TSV CAD, and solder footprint, is available to download here.

www.onsemi.com
8

Share Feedback
Your Opinion Matters

Figure A.25.: SiPM data sheet [35]

A.3. Additional simulation data

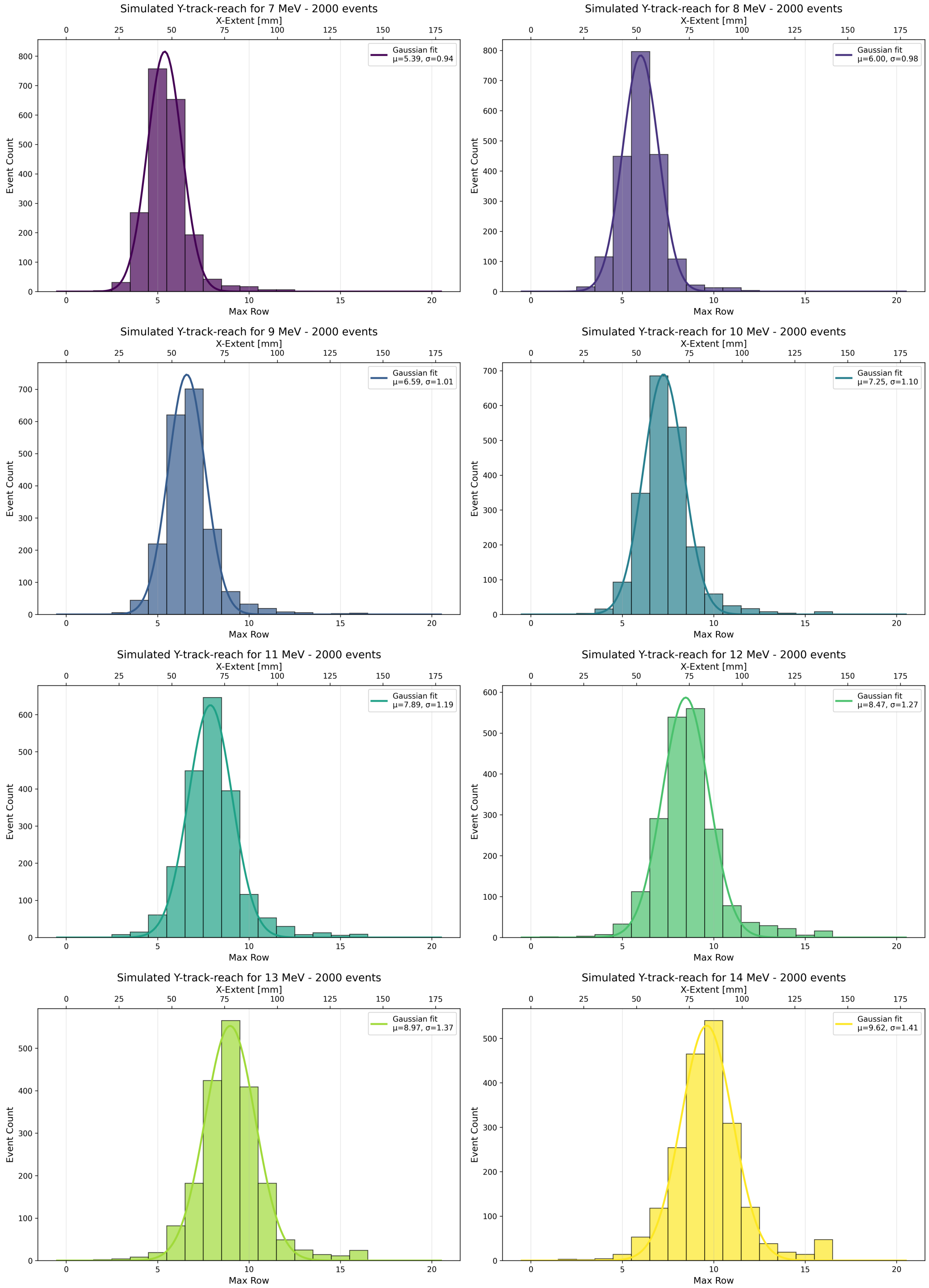

Figure A.26.: Distribution for electrons for all simulated energies with Gaussian fits

A.4. Beamline simulation

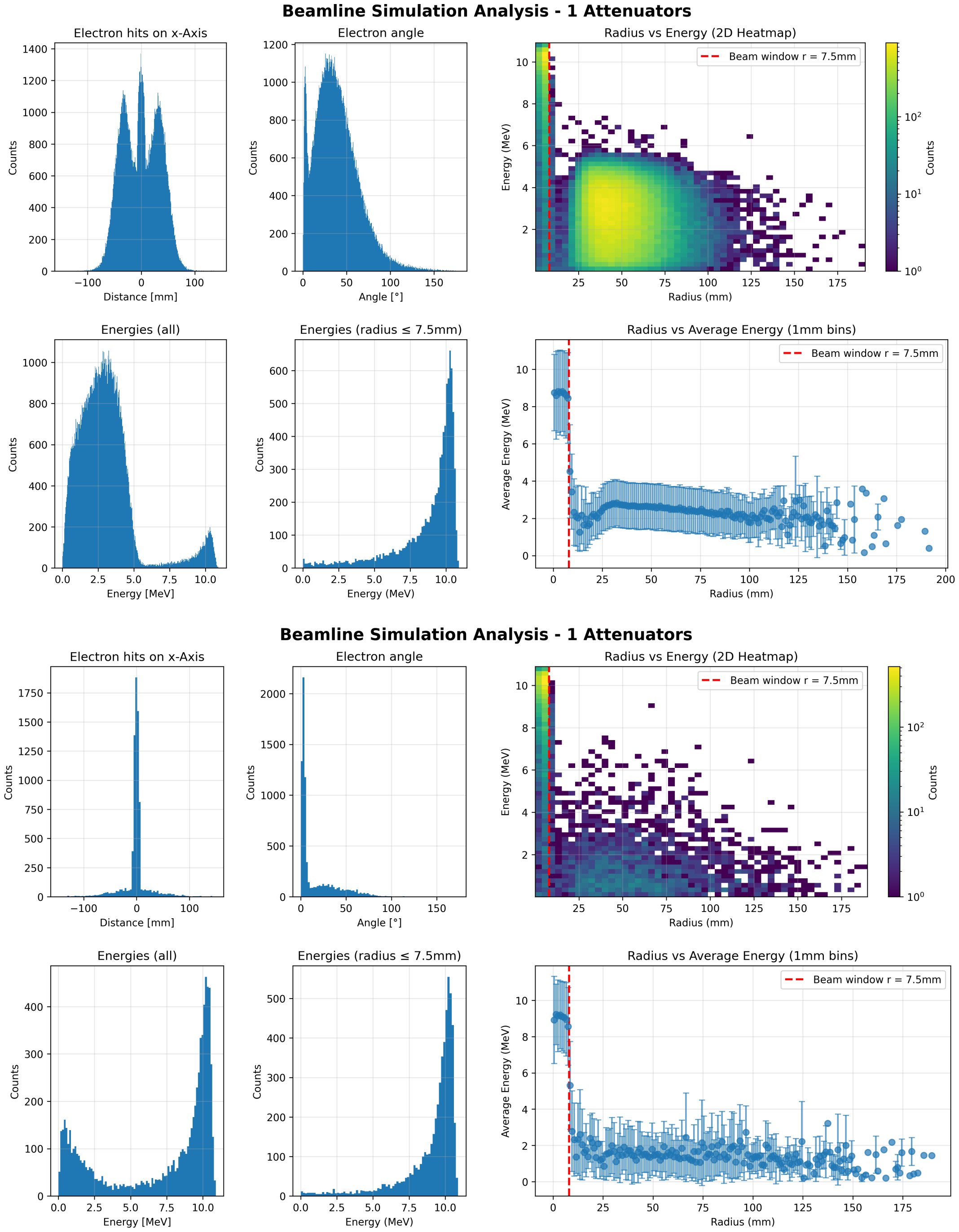

Figure A.27.: Results of the beam line simulation with 1 attenuators. Top without the collimator-shield and the bottom with the shielding.

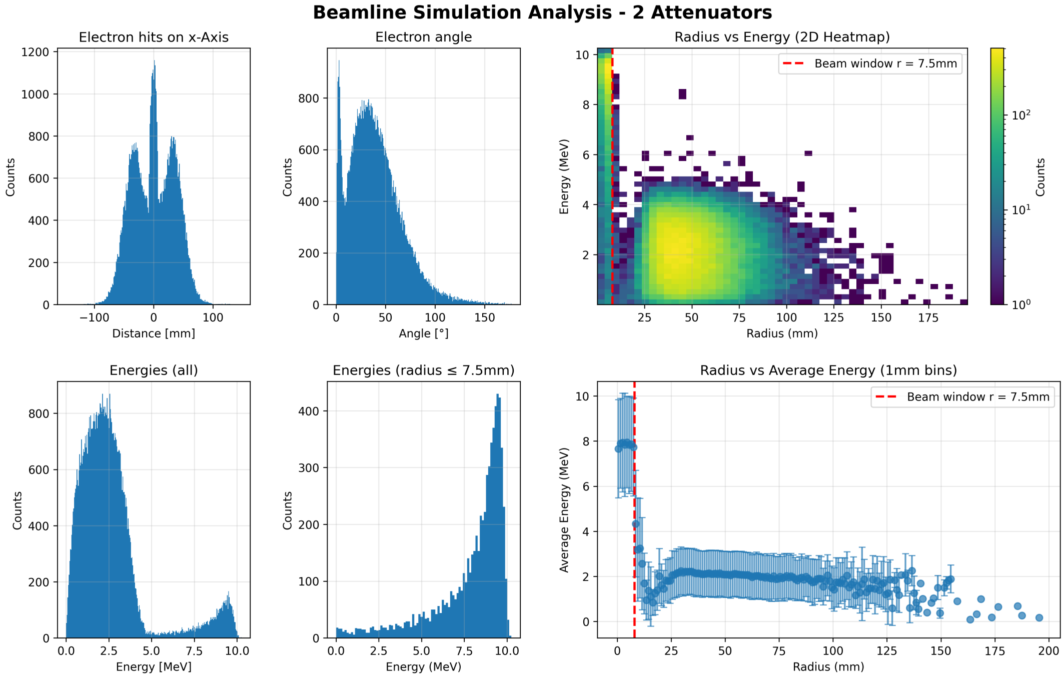

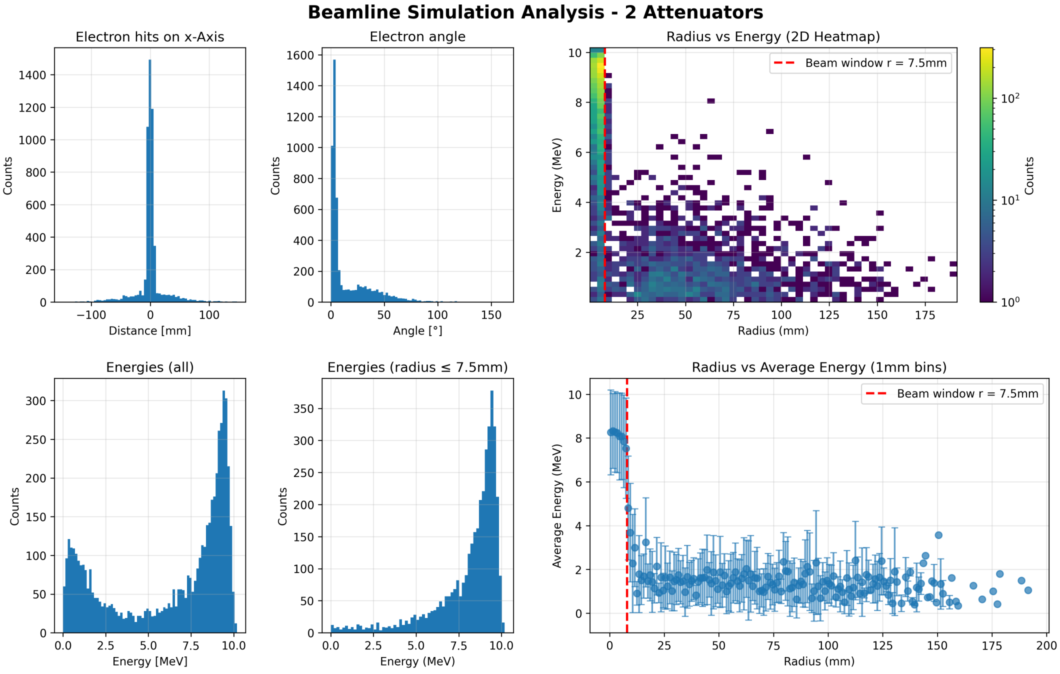

Figure A.28.: Results of the beam line simulation with 2 attenuators. Top without the collimator-shield and the bottom with the shielding.

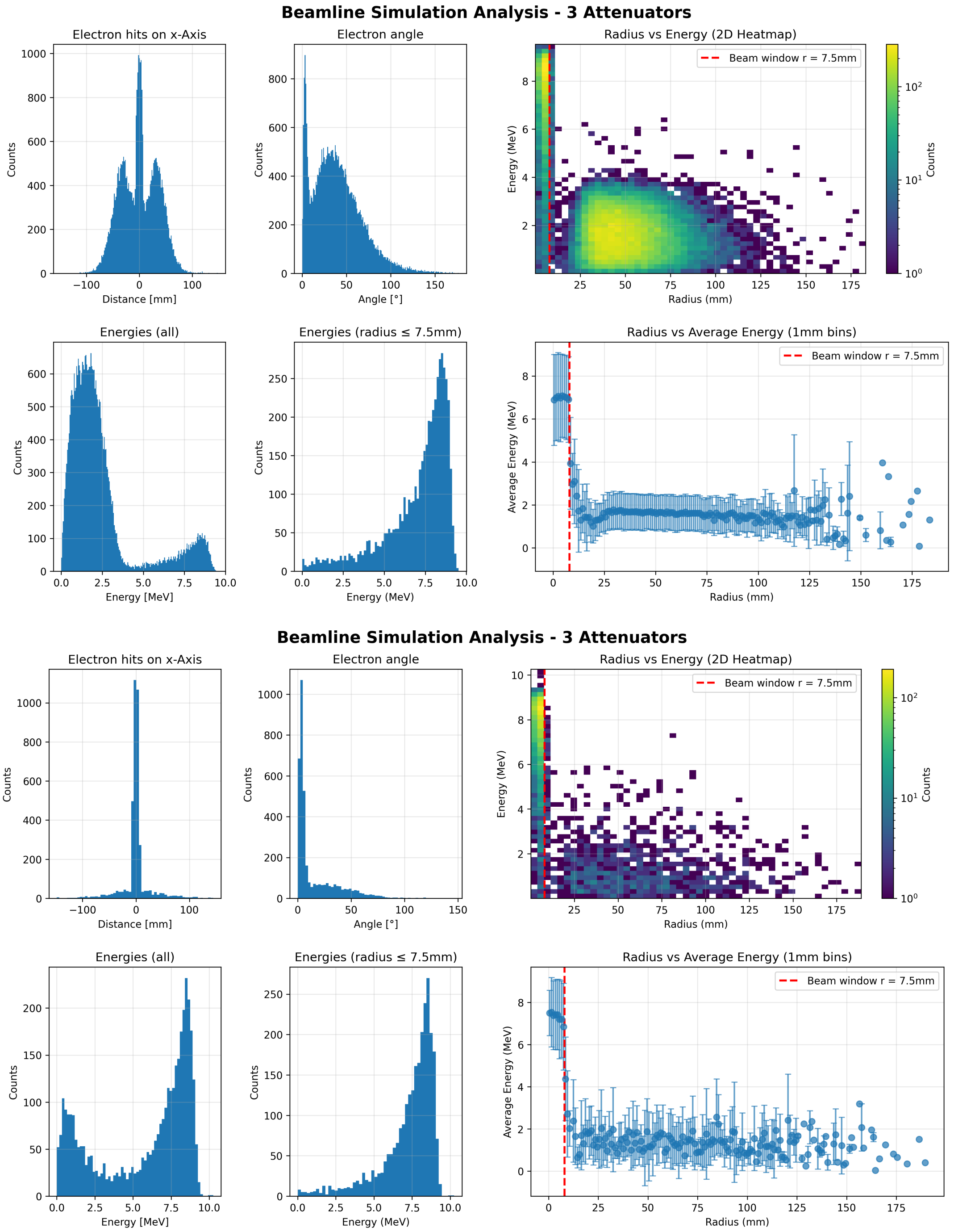

Figure A.29.: Results of the beam line simulation with 3 attenuators. Top without the collimator-shield and the bottom with the shielding.

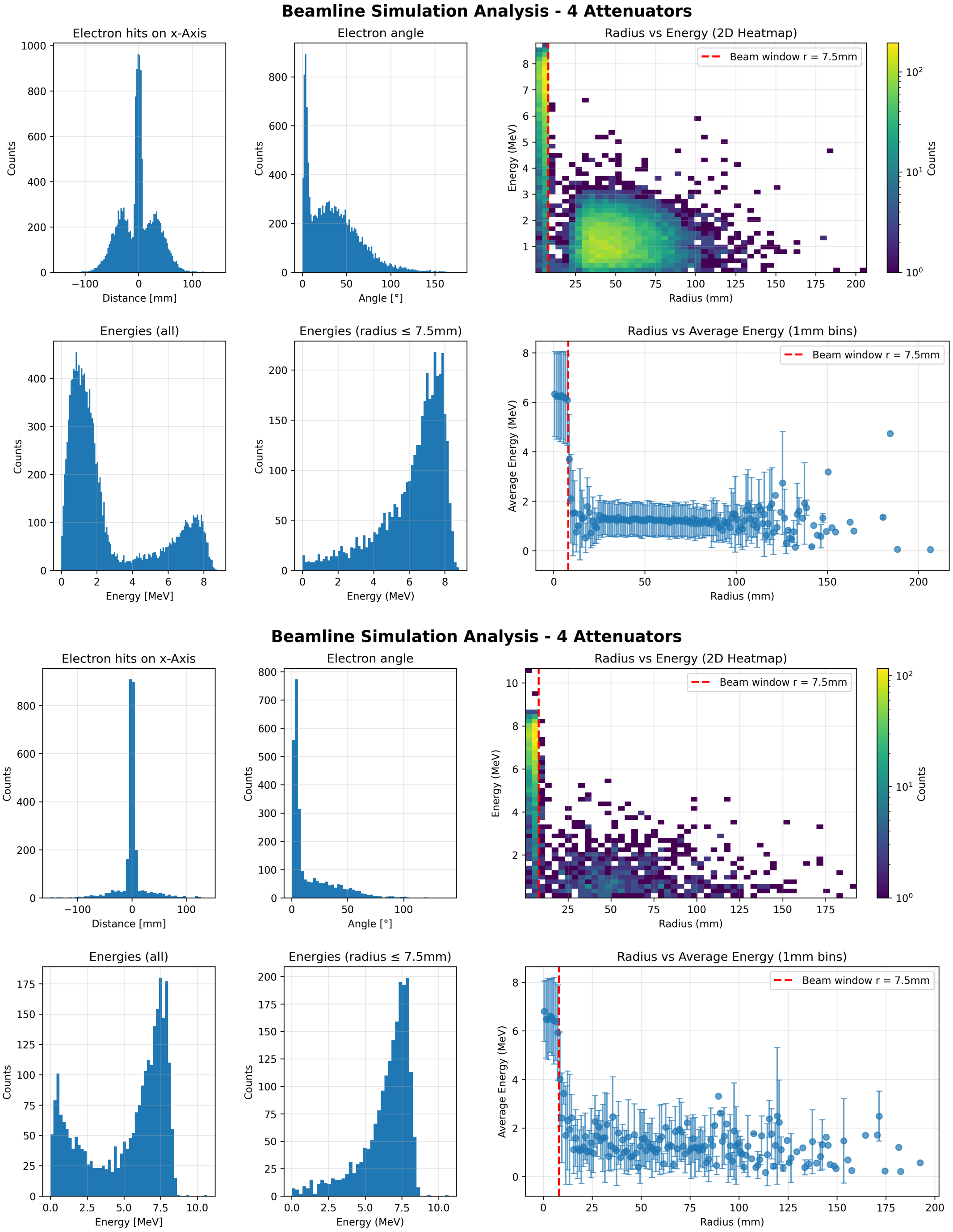

Figure A.30.: Results of the beam line simulation with 4 attenuators. Top without the collimator-shield and the bottom with the shielding.

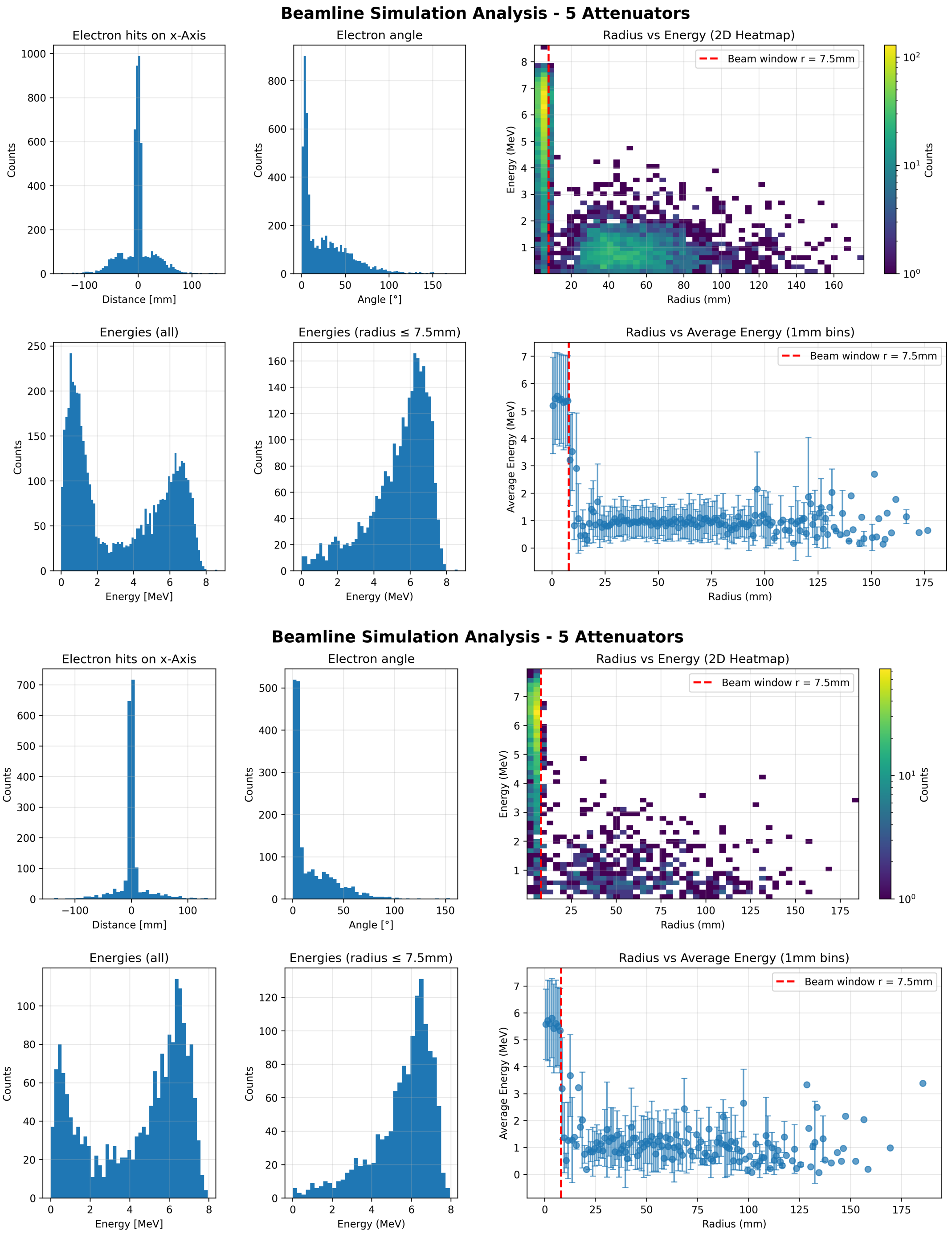

Figure A.31.: Results of the beam line simulation with 5 attenuators. Top without the collimator-shield and the bottom with the shielding.

A.5. Used AI tools

The following AI tools were used during this thesis:

AI tool	Used for	Reason
Claude by Anthropic	Coding assistance for Python	To provide Python code snippets in order to increase coding efficiency, speed quality
	Coding assistance for C^{++}	To enable the use of C^{++} without knowledge prior to the start of this thesis
	Formulation assistance for LaTeX	To improve efficiency while writing and provide syntax examples
ChatGPT by OpenAi	Coding assistance for Python	To provide Python code in order to increase coding efficiency, speed and quality
	Formulation improvements	To improve the quality and readability of the written text
	Spell checking	To efficiently detect typing errors for a better text quality
	General research assistance	To effectively cross checking of simple calculation, provide cross references, check feasibility of design ideas

Table A.1.: Used AI tools throughout the entire thesis

B. Acknowledgments

At this point, I would like to thank both my supervisors, PD Dr. Luca Doria and Dr. Stefan Schoppmann, for giving me the opportunity to write my Master's thesis within the DarkMESA group and the NuDoubt^{++} collaboration. Their advice throughout this thesis was invaluable, and I could always count on their support.

I would also like to thank the members of both groups for their support during the entire course of my thesis, for their help during my beam time at MAMI, and especially Mirco Christmann, Saskia Plura, Christian Stoß, and Michail Kontogoulas for proofreading and their extensive advice on writing this thesis.

The design and construction of the prototype detector, as well as the production of all 255 Bubo fibres, would not have been possible without the help of Steffen Schönfelder and Fabian Piermaier, both of whom dedicated considerable time to ensuring the detector was finished just in time for the tests at MAMI.

I am grateful to Reinhold Degele, who designed both PCBs used in the detector on short notice, as well as to Sebastian Ritter for his advice on operating the FERS system. The production of this electronics would not have been possible without the expertise and work of Igor Beltschikow and the electronics workshop of the Institute of Nuclear Physics.

I would like to thank my close friend Daniel Schmid, whom I could always rely on for advice and support during this thesis and who even accompanied me on the day-long road trip to collect the PCBs near Munich.

Last but certainly not least, I thank my partner and my family, without whose support this thesis - and indeed my entire degree - would not have been possible.